



**Universitat
Autònoma
de Barcelona**

Statistical Models of the Architecture and Function of the Left Ventricle

A dissertation submitted by **Jaume Garcia i
Barnés** at Universitat Autònoma de Barcelona
to fulfil the degree of **Doctor en Informàtica**.

Bellaterra, September 2009

Director: **Dra. Debora Gil i Resina**
Universitat Autònoma de Barcelona
Dep. Ciències de la Computació & Computer Vision Center
Co-director:



This document was typeset by the author using L^AT_EX 2_ε.

The research described in this book was carried out at the Computer Vision Center, Universitat Autònoma de Barcelona.

Copyright © 2009 by Jaume Garcia i Barnés. All rights reserved. No part of this publication may be reproduced or transmitted in any form or by any means, electronic or mechanical, including photocopy, recording, or any information storage and retrieval system, without permission in writing from the author.

ISBN 978-84-937261-5-7

Printed by Ediciones Gráficas Rey, S.L.

A la Helens i als pares.

Agraïments

Primerament voldria donar les gràcies a Martin Kamen y Sam Ruben, descobridors del Carboni-14, mitjançant el qual he pogut datar la meva estada al CVC i l'inici del projecte TIVALTA. Durant aquest període, que abarca des de finals del cretaci superior fins a l'actualitat, he tingut l'oportunitat de conèixer un munt de persones meravelloses i fantàstiques. Però, donat que aquest tipus de gent segur que amaga alguna cosa, prefereixo dirigir els meus agraïments a tota la resta.

Dins el CVC hi ha una persona que mereix tota la meva gratitud: la Debora, qui en el seu moment va creure en mi i en el potencial de les meves idees. Sense el seu ajut, aquesta tesi mai hagués arribat on ha arribat. Però no només per això, també li agraeixo la pila d'històries surrealistes que ha aportat, dins el *Proyecto Sonrisas*, a l'hora de dinar. També vull agrair les petites aportacions de moltes altres persones dins el CVC: a l'Àgata, pel vent generat amb el seu parpalleig ultra-ràpid que ha fet més suportables els estius. L'aire acondicionat mai ha funcionat al CVC. A l'Agnés, per resoldre *El Problema de la Visó per Computador* i esperar-me per presentar la tesi. Gràcies Borri. A l'Àlicia per les seves estadístiques inútils, però sempre entretingudes. A l'Anton, per tenir un timbre de veu i un somriure tan sensual; a l'Aura, per fer-me veure que el cervell de les dones funciona amb geometria Riemmaniana mentre que, afortunadament, el dels homes funciona amb geometria Euclidiana. A la Carme, pels concerts a què hem anat. Ah! I també a aquella noia rossa que anava sempre amb ella... Com es deia?... És igual. A en Ciscu, per haver marxat lluny (no cal que tornis¹). A en David Alcalde, per fer-me veure que afirmar una cosa i tot el contrari al cap d'un segon, no està renyit amb la coherència del discurs. Ah! I per les interminables converses de música. ...Tot i que segueixo pensant que Dream Theater és un trunyu. A en David Rotger, la persona més enterada de les últimes tecnologies. A l'Enric, per les seves filosofades magistrals i per fer-me veure que el meu pentinat, en el fons, no és el més ridícul. A l'Eva Costa, per fer-me entendre que en el món de la visió per computador, tot el que requereixi més de 2 thresholds, no funciona. A l'Ernst. Mai ningú no oblidarà la seva ja mítica frase: "Computer Vision is not my dream job". Proposo crear un grup de fans al Facebook! A l'Ernest, amb qui la docència de tots aquest anys ha estat una bassa d'oli. A la Laura, amb qui sempre tot continua Igual. A la Marín per salvar-me la vida davant l'atac d'uns skins rabiosos. A en Miquel. Gràcies a ell m'he passat a MAC i ara molo més. A la Piulachs, una lionesa que em va ajudar a trobar pis en un moment de màxim estrès. A en Ricard, que m'ha fet veure que és possible rentar roba sense utilitzar sabó; a en Robert, la

¹Ni per Nadal.

persona més meticulosa que conec. A en Santi, tot un exemple de que treballar amb imatges de merda (literalment), pot arribar a ser glamurós. També en Poal, la Raquel, en Sergio o en Xevi amb qui, en un moment o altre ens hem fet unes 'risas'. Ja fora del CVC, però vinculats al meu treball, voldria donar les gràcies a en Francesc i a en Manel, per les seves llargues xerrades sobre la banda miocàrdica. Gràcies a ells m'he adherit al club de fans d'en Torrent-Guasp. I ja posats, també al Paco, per haver trencat esquemes en anatomia cardiològica. A la gent del BSC, la Ruth i en Mariano. A en Patrick, per haver-me acollit al Creatis (a Lyon).

Tot i que no tenen res a veure amb la tesi també voldria donar les gràcies a la gent de Sant Feliu de Guíxols, de mates i de Castellar, ja que d'una manera o altre m'han doant suport. A SFG, en Marc i en Raül (malgrat pensin que la meva feina consisteix en retallar caretes amb un punxó), la Marta Manson (que fa els millors llibrets de l'univers), la Gemma, en Jordi (per ensenyar-me que el més important de ser professor, és sortir al patatabrava) i la Marta, i en Sergi i l'Anna (the real Fu). A mates, en Cirer i na Clara, la Teresa i l'Albert, la Sara, la Remeiu i tota la resta de la 'Colla Maca', que no són pocs. A Castellar, en Yanyís, en Pere, en Yevi i la Lelis i l'Erola. A en Jordi i l'Isabel els agraeixo la oportunitat que m'han donat de pernoctar a mig kilòmetre d'una central nuclear i a 20 kilòmetres d'una planta de tractament de residus nuclears a Normandia. Now I glow in the night!

Per acabar, voldria agrair el suport que m'ha donat la meva família al llarg de tots aquests anys. Especialment als pares, que es pot dir que són els màxims fans del meu treball (sempre amb el permís dels Beatles) i l'avi a qui, de ben segur, li hagués agradat moltíssim assistir a la defensa de la tesi.

De tots és sabut que el el plat fort d'un concert es deixa pel final. Doncs bé, si això fons un concert, el cap de cartell seria la Helens. Ella no només m'ha donat suport explícit i impagable, sinó que a més ha aguantat (de bon grat, sens dubte) moltes 'frikades' durant tot el temps que he estat escrivint la tesi. És per aquest motiu que el meu màxim agraïment va dirigit a ella. Tinc moltes ganes de fer aquestes llargues vacances amb tu!

Tal dia farà un any.

Abstract

Cardiovascular Diseases, specially those affecting the Left Ventricle (LV), are the leading cause of death in developed countries with approximately a 30% of all global deaths. In order to address this public health concern, physicians focus on diagnosis and therapy planning. On one hand, early and accurate detection of Regional Wall Motion Abnormalities (RWMA) significantly contributes to a quick diagnosis and prevents the patient to reach more severe stages. On the other hand, a thoroughly knowledge of the normal gross anatomy of the LV, as well as, the distribution of its muscular fibers is crucial for designing specific interventions and therapies (such as pacemaker implanction). Statistical models obtained from the analysis of different imaging modalities allow the computation of the normal ranges of variation within a given population. Normality models are a valuable tool for the definition of objective criterions quantifying the degree of (anomalous) deviation of the LV function and anatomy for a given subject. The creation of statistical models involve addressing three main issues: extraction of data from images, definition of a common domain for comparison of data across patients and designing appropriate statistical analysis schemes.

In this PhD thesis we present generic image processing tools for the creation of statistical models of the LV anatomy and function. On one hand, we use differential geometry concepts to define a computational framework (the Normalized Parametric Domain, NPD) suitable for the comparison and fusion of several clinical scores obtained over the LV. On the other hand, we present a variational approach (the Harmonic Phase Flow, HPF) for the estimation of myocardial motion that provides dense and continuous vector fields without overestimating motion at injured areas. These tools are used for the creation of statistical models. Regarding anatomy, we obtain an atlas jointly modelling, both, LV gross anatomy and fiber architecture. Regarding function, we compute normality patterns of scores characterizing the (global and local) LV function and explore, for the first time, the configuration of local scores better suited for RWMA detection.

Resum

Les Malalties Cardiovasculars (MCV), especialment aquelles que afecten el Ventricle Esquerre (VE), són la principal causa de mortalitat als països desenvolupats, causant un 30% del total de les morts. Per tal d'afrontar aquest problema, els metges tracten dos punts principals, la diagnosi i la planificació de teràpies. Per una banda una detecció acurada i precoç de les Anomalies Regionals del Moviment del Teixit (ARMT) contribueix, de forma significativa, a disminuir el risc que el pacient empitjori el seu estat. Per altra banda, el coneixement exhaustiu de l'anatomia externa del VE, així com la distribució de les fibres musculars dins el miocardi és crucial per tal de dissenyar intervencions i teràpies apropiades (com ara la implantació de marcapassos). Els models estadístics obtinguts a partir de l'anàlisi de diferents modalitats d'imatge mèdica permeten calcular els rangs de normalitat dins una població donada. Aquests patrons de normalitat són una eina molt valuosa per tal de poder definir criteris objectius que permetin quantificar el grau de desviació de la funció i la anatomia del VE per a un subjecte donat. La creació de models estadístics requereix tractar tres punts principals: la extracció de dades a partir de les imatges, la definició d'un domini de comparació de les dades obtingudes en els diferents pacients i, finalment, el disseny d'esquemes apropiats per l'anàlisi estadística.

En aquesta tesi es presenta tot un seguit d'eines genèriques per a la creació de models estadístics tant de l'anatomia com de la funció del VE. Per una banda s'usen conceptes de geometria diferencial per tal de definir un marc computacional (el Normalized Parametric Domain, NPD) adequat per a la comparació i fusió de varis valors clínics estimats sobre el VE. Per altra banda es presenta una aproximació variacional (l'Harmonic Phase Flow, HPF) per a l'estimació del moviment miocàrdic. El resultat és un camp vectorial dens i continu que no sobreestima el moviment en les zones afectades. Aquestes eines s'utilitzen per a la creació de models estadístics. Quant a l'anatomia, construïm un atlas que modela conjuntament l'anatomia externa i l'arquitectura de les fibres. Pel que fa a la funció, calculem els patrons de normalitat de diversos valors que caracteritzen la funció (global i local) del VE. Amés, explorem per primera vegada quina és la configuració de valors locals més apropiada per a la detecció d'ARMT.

Contents

Agraiments	i
Abstract	iii
Resum	v
1 Introduction	1
1.1 Goals of the Thesis	6
1.2 Magnetic Resonance Imaging	7
1.3 An Overview of the State of the Art	9
1.3.1 Anatomy Modelling	10
1.3.2 Function Modeling	13
1.4 Main Contributions of the Thesis	18
1.5 Structure of the Thesis	19
2 Anatomy and Function of the Heart	21
2.1 Gross Anatomy of the Heart	21
2.1.1 Coronary Vessels	21
2.1.2 Chambers	22
2.1.3 Valves	23
2.2 Fiber Architecture of the Heart	24
2.2.1 Techniques for Measuring Cardiac Architecture	25
2.3 Conceptual Models of Cardiac Architecture	27
2.3.1 Distinct Muscle Bundles and Three-Layered Ventricle Models	28
2.3.2 Helical Myocardial Ventricular Band Model	29
2.3.3 Simple and Complex Laminar Structure Models	31
2.3.4 Nested Doughnut and Pretzel Geodesics Models	31
2.4 Gross Function of the Heart	32
3 Harmonic Phase Flow	35
3.1 Harmonic Images	35
3.2 Tracking Issues	36
3.3 Harmonic Phase Flow	38
3.3.1 Retrieving Angle Images	38
3.3.2 Variational Approach to LV Motion	41

3.3.3	Numerical Issues	44
3.4	Experiments	47
3.4.1	Synthetic Data	47
3.4.2	Real Data	50
3.5	Discussion	53
4	Normalized Parametric Domain	57
4.1	Background on Manifolds	57
4.1.1	Mapping Data to the Parametric Domain	61
4.2	Normalized Parametric Domain Framework	62
4.2.1	NPD Framework Properties	63
4.3	Definition of the NPD for the Left Ventricle	64
4.3.1	NPD in (2D) SA TMR Sequences	65
4.3.2	NPD in (3D) DTI Volumes	70
5	Anatomy Modelling	77
5.1	Gross Anatomy Modelling	77
5.1.1	Control Point-Based LV Atlas	77
5.2	Fiber Modelling	80
5.2.1	Principal Eigenvector Statistics	80
5.3	Visualization of Fibers Architecture	83
5.4	Experiments	86
5.4.1	Anatomic Atlas	87
5.4.2	Evidences Supporting the HMVB	91
5.5	Discussion	92
6	Function Modelling	95
6.1	Function Descriptors	95
6.1.1	Global Descriptors	95
6.1.2	Local Descriptors	97
6.1.3	Multivariate Regional Function Descriptors	98
6.2	Time and Space Normalization	99
6.3	LV Functional Assessment	100
6.3.1	Normality Patterns	100
6.3.2	Regional Function Assessment	100
6.3.3	Parametric Images	101
6.4	Experiments	102
6.4.1	Normality Patterns	102
6.4.2	Optimal Configuration for RWMA Assessment	104
6.5	Discussion	108
6.5.1	Normality Patterns	108
6.5.2	RWMA Assessment	109
7	Conclusions and Future Lines of Research	127
	Bibliography	135

List of Tables

3.1	Parameter ranges of the Gabor filter banks for each type of sequence .	41
3.2	Motion parameters of the 3D phantom for each frame of the systolic cycle.	48
6.1	Visualization of Regional Function Assessment.	101
6.2	Mean values and their standard deviation for basal (B), mid (M) and apical (A) levels. Torsion (T) is also showed. Values are given for 6 stages of the systolic cycle.	103
6.3	Parameter configurations used in our experiments	104
6.4	Statistics summary.	108
6.5	RWMA validation for \mathcal{C}_6	110
6.6	RWMA validation for ICA-method and WT reported in [185]	110

List of Figures

1.1	CVD risk factors due to a non-healthy lifestyle. From left to right: smoking, bad food habits, alcohol, physical inactivity and obesity.	2
1.2	Different imaging modalities for the visualization of specific anatomical, functional and physiological aspects of the heart.	3
1.3	Main steps in the creation of statistical models of anatomy and function of the heart.	5
1.4	Slices of DTI volumes for 2 complementary planes: red (top row) and blue (bottom row). Geometrical volume in A and B. x , y and z components of DTI principal eigenvector in C, D; E, F and G, H respectively.	8
1.5	Standard acquisition slices. On the left image, we show slices perpendicular to the long axis of the heart (called short axis, SA) at the 3 levels (base, mid and apex) covering the whole LV. On the right image, we show the most common slices parallel to the long axis (called long axis, LA), These are the so called 2- and 4-chambers.	9
1.6	TMR sequences. The first 3 rows belong to the SA view and stand for basal, mid and apical tomographic slices respectively. The 2 bottom rows belong to the LA view and stand for 2- and 4-Chambers respectively.	10
1.7	Different cardiac coordinate systems. Cartesian coordinates in a) and d) for 3D and 2D respectively. More adapted coordinates are cylindrical b) and prolate spheroidal c) for 3D; and polar e) for 2D.	17
2.1	Location of the four valves of the heart (left), and the course of the main coronary vessels over the heart surface (right). Illustration by CC Patrick J. Lynch and C. Carl Jaffe, Yale University, 2006	22
2.2	Two longitudinal cuts of the heart showing the main structures of the heart. Illustration by CC Patrick J. Lynch and C. Carl Jaffe, Yale University, 2006	23
2.3	In his Tractatus de Corde (1669), Richard Lower already described the approximate helical structure of the heart.	25

2.4	Different muscular fibers. a) Appearance of the skeletal muscular fiber bundles. They appear completely parallel each other, without branching. b) Illustration of the morphology of the skeletal muscle fibers. c) Appearance of myocardium (stained with H & E at roughly 400x) in a light microscope. Branching myocardial fibers can be appreciated. Despite of this, a main direction is visible. d) 3D scheme of the locally branching fibers (image from [10]).	26
2.5	Oblique view of extended volume image from left ventricle of rat heart obtained using confocal microscopy. Note the laminar organization of myocytes. In the detail, section perpendicular to myocyte axis. (Image from the Royal Microscopical Society).	26
2.6	Different cardiac architecture models. In the first row, older models based on dissection techniques: DMB, TLV and HMVB. In the second row, most recent models based on histology: NDG, SLS, NPG and CLS.	28
2.7	Unfolding the HMBV. Different stages of the systematic dissection process of the heart.	29
2.8	Scheme of the colored band segments (a)-(c). The right ventricle (blue) and upper portion of the left ventricle (red) form the basal loop. The descendant (yellow) and ascendant (green) segments form the apical loop. AS, ascendant segment; DS, descendant segment; LS, left segment; RS, right segment. The complex spatial distribution of these segments can be appreciated by wrapping the band again and obtaining axial (d)-(f) and longitudinal (g), (h) slices.	30
2.9	Construction of the Nested Pretzel Geodesics model from two joined tori.	32
2.10	Electromechanics of the heart: a) pumping action of the heart (cardiac cycle) and b) electrical system.	33
3.1	Harmonic peaks. a) Frame in the spatial domain tagged using 2 hard frequency radio pulses along vertical and horizontal directions. b) In the frequency domain 25 harmonic peaks, each corresponding to an harmonic image. Circles indicate the main harmonic peaks associated to the main harmonic images.	36
3.2	a) Real part of the complex sinusoid. The norm of ω defines the frequency inside the window of size [H,W] and its direction determines de direction of the sinusoidal pattern. b) Gaussian envelope that determines the scale of the filter. This envelope is rotated ϕ degrees, and its main axes has sizes $\sigma_{x'}$ and $\sigma_{x'}/\lambda$. c) Product of the real part of the complex sinusoid and the gaussian envelope: Real part of the Gabor filter.	39
3.3	American Heart Association nomenclature for myocardial segments in SA views seen from apex to base. a) Basal and mid sectors: anterior (a), anterolateral (al), inferolateral (il), inferior (i) inferoseptal (is) and anteroseptal (as). b) Apical sectors: anterior (a), lateral (l), inferior (i) and septal (s).	40

3.4 Main Steps in the Computation of the Left Ventricle Dynamics. Above on the left, two consecutive frames of a basal sequence. On the right their respective bi-dimensional harmonic representations that, together with the weighting functions (in the center), conform the variational framework for robust tissue tracking. Below on the right we show the result of the HPF, where vectors have been discretized and resized for visualization purposes. On the left detail of the real dense deformation map. 42

3.5 In the first column, motion vector field estimated by HPF in a sequence of 6 TMR frames (motion detected among consecutive frames, 5) belonging to a basal slice. In the second and third columns, successive zooms of the original frame. 47

3.6 Phantoms. a) 3D dynamic myocardial model intersected by 4 representative acquisition planes. b) Basal sequence frames for phantom #2 simulating motionless background and 2 gaps without tagging pattern. 49

3.7 HPF accuracy for the 2 dynamic phantoms. In dark bold line, the mean error between the real deformation map and the estimated one along the whole systolic cycle. Vertical gray lines represent the standard deviation. Phantom #1: a) base, b) mid, c) apex and d) long axis. Phantom #2: e) base, f) apex. 51

3.8 HPF Error distribution analysis for phantom #2.: Error maps along systolic cycle in a), and image weights (α_1, α_2) of the regularization term for frame 4 in b). 52

3.9 Details for a frame of the phantom #2 after applying HPF. In a) and b) gaps (noise) have been filled with the surrounding values, due to action of the regularizing term of the variational framework. In c) we can appreciate that in still tissue and air HPF detects no motion. In d) we can observe motion detected over the left ventricular tissue. . . 52

3.10 HPF accuracy for experimental data. In dark bold line, the mean error between the real deformation map and the estimated one, along the whole systolic cycle. Vertical gray lines represent the standard deviation for a) base, b) mid, c) apex and d) long axis. 54

3.11 HPF-based contour tracking. The initial contours (first column) of basal, mid, apical and LA instances, have been tracked using HPF, and results are shown at 50% (second row) and 100% of the systolic cycle. 55

4.1 n -dimensional manifold embedded into \mathbb{R}^m . The local chart (\mathcal{U}, Φ) defines local coordinates and coordinate directions inside a neighborhood of \mathcal{M} . The inverse mapping, Ψ , defines the parametrization of a portion of \mathcal{M} 58

4.2 Atlas of local charts. a) Two local charts covering a piece of the manifold \mathcal{M} . b) A Single Charted Manifold. The deformed piece of \mathbb{R}^n , \mathcal{U} , covers the whole \mathcal{M} 59

4.3	Unfolding process of the LV in the 2D case a), and in the 3D case b). Notice that such unfoldings provide a parametrization, Ψ , between a rectangular domain and the LV.	60
4.4	Tangent Space.	61
4.5	Implicit parametrization scheme. The parametrization functions Ψ_1 and Ψ_2 put in correspondence \mathcal{M}_1 and \mathcal{M}_2 with \mathcal{V} . Since same anatomical positions in both objects (marked with \star) are assigned the same parameter \mathbf{u} , both objects are implicitly registered in \mathcal{V}	62
4.6	\mathcal{LV}_0 parametrization. a) Landmark identification (\mathcal{ED} , \mathcal{EP} , \mathbf{x}_{ant} and \mathbf{x}_{inf}) for the definition of the affine reference. b) \mathcal{LV}_0 boundaries parametrization and interpolation of intramural points, $\mathbf{x}^0(u, w)$	66
4.7	Piecewise linear parametrization function that maps all angles to a normalized interval, taking into account the proportion of septal and non-septal area.	67
4.8	Implicit Registration of two TMR sequences belonging to different subjects. Each parametrization Ψ_n^t defines a coordinate system tailored for the geometry of each subject and time. Same anatomical locations share the same parameter in Ω^2	69
4.9	Parametric directions fitting LV geometry and detail of the local coordinate systems $\{e_u, e_w\}$ (along circumferential and radial directions resp.) induced by the parametrization Ψ^t	69
4.10	Location of the LV axis. On the left hand side, we sketch the creation of the X-Ray like images I_1 and I_2 , that are used to locate keypoints A_1 and A_2 for the estimation of the apical cap. On the right images we show both projections with the 2 points (A_1 and A_2) marked with a star.	71
4.11	Location of the LV axis. Selection of appropriate LA slices and landmarking keypoints B_{11} , B_{12} , B_{21} and B_{22} for the estimation of the basal ring centroid.	71
4.12	Tomographic slices perpendicular (A) and parallel (B) to the long axis of the LV.	73
4.13	Wire-frames depicting LV silhouette. Red ones belong to the endocardium (ψ_s^0) and green ones to the epicardium (ψ_s^1). Basal ring wireframes are denoted by $s = 0$ and SA wireframes by $s = 1 \div N_{SA}$	74
4.14	Implicit registration of the \mathcal{LV}_n of different subjects. Each parametrization Ψ_n defines a coordinate system tailored for the geometry of each subject. Same anatomical location share the same parameter in Ω^3	75
4.15	Parametric directions fitting LV geometry and detail of the local coordinate systems $\{e_u, e_v, e_w\}$ (along circumferential, longitudinal and radial directions resp.) induced by the parametrization Ψ	76
5.1	Scheme illustrating that arithmetic mean provide, for observations over manifolds, a result that does not lie over the manifold.	81
5.2	The exponential map generates a radial isometry between the manifold and the tangent space. Covariance can be computed on the tangent space using standad techniques.	82

5.3 Exponential map associated to the point $\tilde{\xi}$ and its inverse. Detail on the right depicts the situation over a maximum circle. 82

5.4 Correspondence between myocardial fibers and points in the unitary disk, \mathcal{D}^1 . a) A fiber at point $\mathbf{x} \in \mathcal{LV}$ is represented by a unitary vector V expressed in terms of local references $\{e_u, e_v, e_w\}$. b) V mapped to the NPD lives in a unitary semisphere S^{2+} where is noted by ξ . ξ might be expressed in terms of a couple of angles, θ and φ , which codify respectively the orientation and the elevation angle of the fiber, with respect the loca reference. c) S^{2+} is isomorph the unitary disk \mathcal{D}^1 via orthogonal projection. Orientation and elevation angles are now codified by θ and r . Each fiber is characterized by this couple of values. 84

5.5 Coloring criteria. On the left a table that assigns (R,G,B) colors to 5 keypoints on the disk that are given in polar coordinates. Notice that for $r = 0$ all points coincide with the center of the disk. On the right, the location of these points inside the disk. 85

5.6 a) Discrete colormap using 8×3 regions. b) Relation between the uniform partition of the elevation angle and the non-uniform partition of the r -direction. 86

5.7 By rows, the 6 principal modes of variation obtained moving parameter b_n up to ± 2 standard deviations from the mean, shown in the central column. 87

5.8 Average fiber distribution in Ω^3 for 6 slices of constant radial parameter $w = \{0, 0.21, 0.35, 0.64, 0.78, 1\}$, for $w = 0$ the endocardium and $w = 1$ the epicardium. The yellow lines represent the junction between right and left ventricles at anterior (continuous line) and posterior (dashed line) walls. Apical area is labelled 'A', basal 'B' and septal 'S'. 88

5.9 Average fiber architecture over the average gross anatomy of the \mathcal{LV} . The colors (cyan and magenta) are in concordance with those in Fig. 5.8. 89

5.10 Tractography performed onto the average fiber architecture mapped to the mean LV gross anatomy. Blue fibers have been generated using seeds placed in the epicardium ($w = 1$), whereas green and red fibers have been obtained using seed placed in the midwall ($w = 0.5$) and in the endocardium ($w = 0$) respectively. **S** indicates the septal wall and the bold black line, the junction between RV and LV at anterior wall. 90

5.11 Correspondences observed between the fibers obtained performing tractography on our average model (first two images) and those in an schematic visualization of the HMVB, where the RV have been uncoupled from the LV (last image). Equivalent anatomical areas are marked with th same symbol in all images. 90

5.12 Synthesis of maps of fibre orientation obtained from DTI with ventricular architecture from histology (a-d). Canine histological pinnation patterns observed in [89] at systole (e) and diastole (f). Longitudinal reconstruction of murine optical mapped fibre angle obtained in [126] (g). 91

5.13	Coloring method applied to 3 canine hearts and to the mean model. Transition between red-most and green-most areas (which contain fibers running oppositely) clearly show the HMVB dissection path. Below on the left the legend codifying the orientation of the fiber according to the local references is depicted. On the right, the legend depicts the elevation angle according to the tone of the color.	92
6.1	Rotation computation. a) A point \mathbf{x}^0 at end-diastole (\mathcal{LV}^0) and its spatial position at time t , \mathbf{x}^t , generate two vectors considering the centroids O^0 and O^t . b) The angle of these vectors multiplied by the sign function ($S^t(\mathbf{x}^0)$), is the rotation experienced by \mathbf{x}^0 at time t . . .	96
6.2	Temporal normalization the component of the motion field V_x	99
6.3	Relation between our BEPs (shown in the center for, both, continuous and discrete cases) and the standard AHA BEP (shown in the right). .	102
6.4	Normality Patterns for basal, mid and apical rotation and torsion. . .	103
6.5	Leave-one-Out Errors for the 9 parameter configurations.	106
6.6	ROC plots for the 9 configurations showing ROC curves for the two experts and the optimal cutoff (horizontal line).	107
6.7	BEPs for ground truth provided by the clinical experts and classification given by $\mathcal{C}_6 = [V_u, V_w, S_M, S_m]$	111
6.8	Normality patterns of motion measured in <i>mm</i> . at base in 9 phases of the systolic cycle.	112
6.9	Normality patterns of motion measured in <i>mm</i> . at mid in 9 phases of the systolic cycle.	113
6.10	Normality patterns of motion measured in <i>mm</i> . at apex in 9 phases of the systolic cycle.	114
6.11	Normality patterns of circumferential strain measured in % at base in 9 phases of the systolic cycle.	115
6.12	Normality patterns of circumferential strain measured in % at mid in 9 phases of the systolic cycle.	116
6.13	Normality patterns of circumferential strain measured in % at apex in 9 phases of the systolic cycle.	117
6.14	Normality patterns of radial strain measured in % at base in 9 phases of the systolic cycle.	118
6.15	Normality patterns of radial strain measured in % at mid in 9 phases of the systolic cycle.	119
6.16	Normality patterns of radial strain measured in % at apex in 9 phases of the systolic cycle.	120
6.17	Normality patterns of maximal strain measured in % at base in 9 phases of the systolic cycle.	121
6.18	Normality patterns of maximal strain measured in % at mid in 9 phases of the systolic cycle.	122
6.19	Normality patterns of maximal strain measured in % at apex in 9 phases of the systolic cycle.	123
6.20	Normality patterns of minimal strain measured in % at base in 9 phases of the systolic cycle.	124

6.21	Normality patterns of minimal strain measured in % at mid in 9 phases of the systolic cycle.	125
6.22	Normality patterns of minimal strain measured in % at apex in 9 phases of the systolic cycle.	126
7.1	Scheme of the proposed iterative method for the creation of patient-tailored electromechanical models.	129

Chapter 1

Introduction

Historically, Cardiovascular Diseases (CVD) were mainly associated to congenital problems and constituted a minor cause of death (only about 0.4 – 0.6% of the population before 1900 [169]). The huge social and economical transformations experienced by the industrialization of countries lead to radical changes in lifestyle. By the 1930's and 1940's, the death rate from CVD was increasing at an alarming rate and it was reaching epidemical proportions. The reasons for this epidemic were not completely clear. Some scientists were convinced that there was a single cause but most researchers favored the theory that there had to be due to multiple of them. Conscious about this problem, the first large-scale comprehensive study (the Framingham Heart Study¹, FHS) to determine the causes of CVD took place after the II World War (1948). The goal of the study was to identify the factors that contribute to the development of CVD. The FHS proceeded by following (over a long period of time) the development of CVD in a large group of participants who were not initially affected. Since its beginnings until the present, the FHS has recruited people from three different generations who returned to the study every two years for a detailed medical history, physical examination, and laboratory tests. Over the years, careful monitoring of the FHS population has identified smoking, bad food habits, physical inactivity or obesity (Fig. 1.1) as some of the main risk factors. Nowadays, although advances in medicine have notoriously drop mortality (increasing life expectation) CVD dare to be the leading cause of death in developed countries. According to the World Health Organization², they already constitute approximately a 30% of all global deaths and they are projected to remain the leading cause of death in the future.

The high prevalence of CVD [2] already represents a major source of expenses for governments of developed countries. Not only in terms of resources consumed in disease prevention, detection and treatment, but also in terms of the costs of providing care for patients and the foregone economic productivity associated with inability to work due to disability or premature death [103]. The economic burden of CVD in

¹<http://www.framinghamheartstudy.org>

²<http://www.who.int>



Figure 1.1: CVD risk factors due to a non-healthy lifestyle. From left to right: smoking, bad food habits, alcohol, physical inactivity and obesity.

the EU is estimated to be €169 billion a year [103] and, for most governments, such expenses represent a considerable amount of their national income.

The term CVD includes a wide variety of pathologies affecting, both, the vascular and the cardiac systems. Since affected coronary vessels can trigger several heart diseases, it follows that most CVD impair the heart to efficiently perform its duty. In particular, the Left Ventricle (LV) which is the responsible for pumping oxygen-rich blood to the whole body. It follows that most people affected from CVD may undergo a reduced quality of life, morbidity and even premature mortality. In order to address this public health concern, physicians address two main points [32]:

- *Diagnosis.* Since CVD often impair the contractile properties of specific myocardial areas they distort their normal local function patterns [188]. It follows that early and accurate detection of myocardial Regional Wall Motion Abnormalities (RWMA) significantly contributes to a quick diagnosis [156, 34, 32] and, thus, prevents the patient to reach more severe stages.
- *Therapy and Intervention Planning.* The remodelling of the myocardial anatomy (architectural distortion) is known to be a prominent feature of many CVD at advanced stages [122, 163]. On one hand, external anatomy distortion is related to some dysfunctions such as hypertrophy. On the other hand, muscular fibers orientation plays a central role in LV electromechanical activation. Thus, their modelling would allow the design of specific interventions (such as pacemaker implantation) and therapies (such as resynchronization) that could notoriously improve the quality of life and increase life expectancy in pathologic subjects [176].

Along the last decades, medical imaging technologies have experienced huge advances that have evoked into a wide range of modalities [207, 184] allowing the visualization of specific aspects of the heart. Figure 1.2 sketches the most extended imaging modalities according to the different physical principles (X-ray, ultrasound or magnetism) used to generate the images. Each of these principles leads to different imaging variants specially suited for the visualization of one or several biological features of the LV. The table in Figure 1.2 indicates which features are properly, roughly or badly captured by each imaging technique. It follows that diagnosis from imaging

		X-Ray	Ultrasound		Magnetic Resonance				Nuclear Imaging	
		CT	SI	EC	CMR	TMR	LE	DTI	SPECT	PET
										
Physiology		X	X	X	X	X	✓	X	✓	✓
	Function									
Anatomy	Wall Motion	X	✓	✓	✓	✓	X	X	X	X
	Intramural Motion	X	✓	X	X	✓	X	X	X	X
Anatomy	Internal	X	X	X	X	X	X	✓	X	X
	External	✓	~	~	✓	~	✓	✓	~	~

CT – Computerized Tomography SI – Speckle Imaging EC - Echocardiography CMR – CINE Magnetic Resonance
 TMR – Tagged Magnetic Resonance LE – Late Enhancement DTI – Diffusion Tensor Imaging PET – Positron Emission Tomography
 SPECT - Single photon emission computed tomography ✓ - Appropriate for X - Not Appropriate for ~ - Can be used for

Figure 1.2: Different imaging modalities for the visualization of specific anatomical, functional and physiological aspects of the heart.

has become a usual and useful tool for assessing myocardial anatomy and function in clinical practice.

Visual inspection of images presents several shortcomings. In most cases physicians can only perform a qualitative evaluation, which does not provide quantitative values for obtaining objective clinical scores. The visualization of the 3D disposition of the tomographic slices provided by some modalities is unfeasible. Finally, interpretation of non-scalar (vectorial or tensorial) quantities becomes difficult or even impossible. The above limitations might lead to substantially different diagnosis, depending on the expertise of the physician (inter- and intra-observer variability). This has encouraged a lot of research in medical image analysis [58] addressing the creation of several computational models reflecting either anatomic or functional aspects of the heart [75]. Such models provide physicians with an objective interpretation of images and might help them to better understand the relation between anatomy and function. Two main approaches for modelling the anatomy and the function of the heart can be considered:

- *Single Subject Models.* They provide either anatomic or functional information of a single subject. Although they are well suited for biomechanical simulations

and the computation of functional scores, their main drawback is that they cannot include the variability observed in a given population. The lack of normality ranges for functional scores reduces its clinical value for diagnosis.

- *Statistical Models.* They consider anatomic and functional values extracted from a large population in order to compute statistical models including the variation of clinical scores. This enables a better understanding of the normal anatomy and function, as well as, the computation of the normal ranges of variation within a given population. It follows that statistical models are a valuable tool for the definition of objective criteria quantifying the degree of (anomalous) deviation of the LV function and anatomy of a subject.

The creation of statistical models of cardiac architecture and function must address three main steps (sketched in the scheme in fig. 1.3):

Data Extraction from Images (top level in Figure 1.3)

Processing of the different imaging modalities provides anatomical and functional scores which, depending on their scope or nature, might be classified as global or local scores. Global scores are scalar quantities (codifying some functional aspect) obtained for the whole LV. If a global quantity is available for each cardiac phase, then the global quantity is said to be time-evolving (e.g., LV rotation and torsion). Otherwise the quantity is said to be static (e.g., LV volume, mass, ejection fraction and cardiac output). Local scores are obtained for each single point of the LV. Coordinates of tissue points (landmarks) or vector fields codifying myocardial fibers orientation are anatomical local scores, whereas motion vector fields or strains (circumferential, radial, etc.) are functional local scores.

In the case of functional scores, they all require accurate computation of LV motion from medical imaging sequences. A critical issue is the overestimation of motion at injured areas.

Comparison Framework (middle level in Figure 1.3)

Computation of statistical models requires comparing measures obtained from different acquisitions. In the case of local scores, a faithful comparison should ensure that each image region (pixel) always corresponds to the same anatomical location for any subject and systolic phase. Thus, the following issues should be addressed:

- *Intra-patient variability* related to the change of LV geometry along the cardiac cycle.
- *Inter-patient variability* related to heart's anatomical differences among subjects and the relative position between the patient and the acquisition conditions.

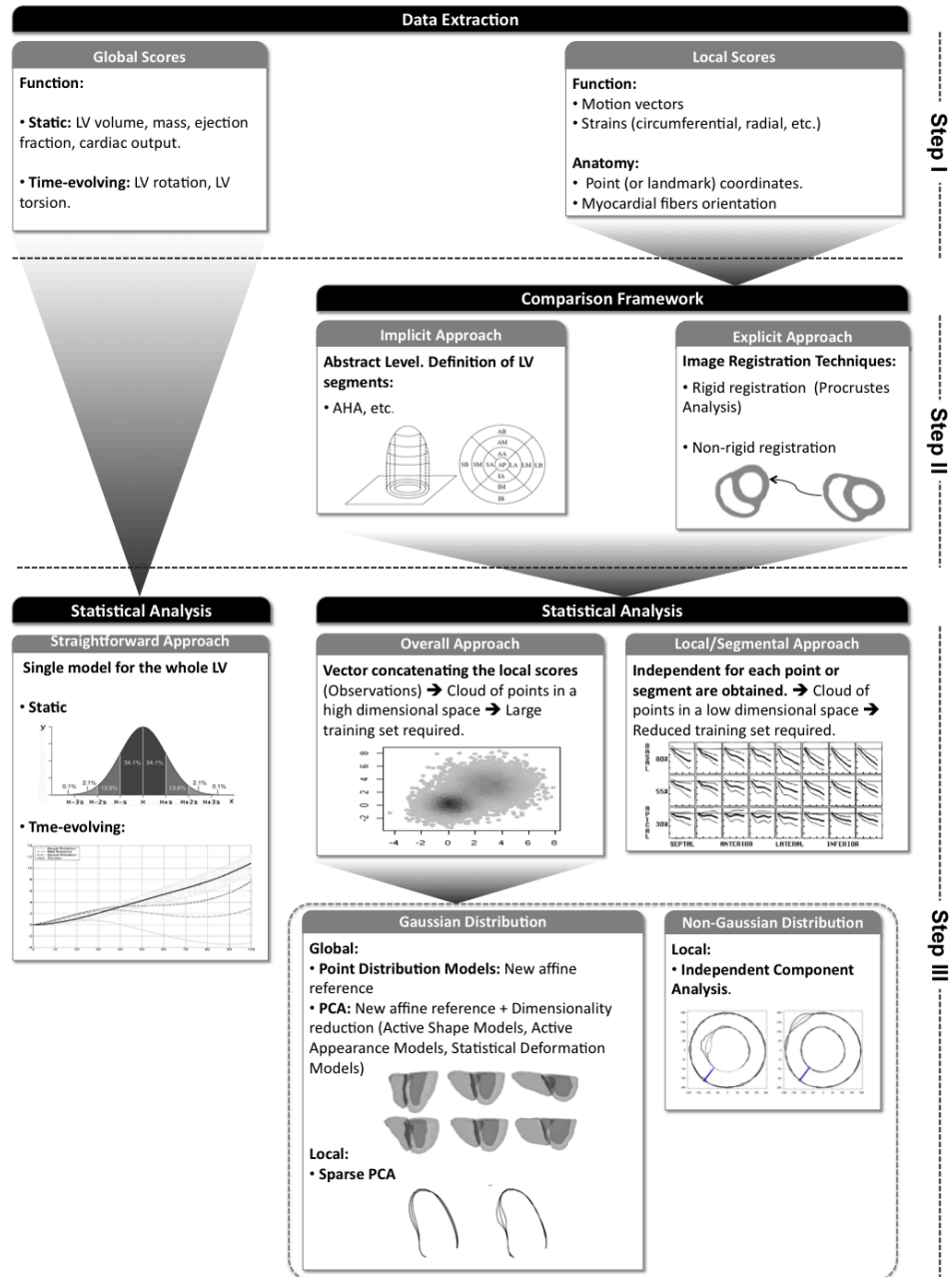


Figure 1.3: Main steps in the creation of statistical models of anatomy and function of the heart.

In order to reduce the impact of inter- and intra-patient variabilities, some sort of data alignment should be made before computing statistics. Current solutions may be split into explicit and implicit strategies. Explicit approaches use image registration techniques which seek the best transformation that matches a target image to a reference one. Implicit approaches take place in an abstract level and divide the LV in segments representing portions of tissue that are defined consistently for all patients, times and image modalities. Anatomical features and appropriate coordinate systems are generally taken into account for the definition of such segments.

The comparison framework might vary substantially depending on whether the score to be modelled represents anatomical or functional features. This suggests a lack of a common framework allowing to handle both types of features.

Statistical Analysis (bottom level in Figure 1.3)

The mathematical tools involved in the computation of statistical models depend on the nature (global / local) of the data. Global scores are straightforwardly modelled by means of descriptive statistics (mean and variance). Local scores may be modelled taking into account either the variability over the whole LV volume or at specific regions/segments. The overall approach leads to a unique statistical model for the whole LV that gathers the mean behavior of the target feature and its modes of variation. A main shortcoming is that they are not properly suited for local variability assessment which might require large training sets (not always available). Local/segmental approaches compute a statistical model for each point or segment. In this fashion they are well suited for modelling local variation without requiring large data sets.

1.1 Goals of the Thesis

The goal of this thesis is to develop general computational tools for the creation of statistical models of the LV anatomy and function, from the processing of MR images. In particular, this thesis presents two contributions to data extraction and comparison framework steps:

LV Motion Extraction. We develop a variational framework, called Harmonic Phase Flow (HPF), for the tracking of LV tissue in 2D sequences. The formulation of HPF gathers in a single equation, both, matching and regularity constraints. The distinct property of our scheme is that the regularity term is only applied at regions preventing non-reliable motion (due to noise or a corrupted tag pattern). In this fashion, the final result is a dense and continuous vector field reflecting tissue motion without overestimating it at injured areas.

Unifying Comparison Framework for Anatomical and Functional Data. We use Differential Geometry concepts to define a generic comparison framework, called Normalized Parametric Domain (NPD), suitable for:

- The comparison and fusion of several scalar and vectorial quantities obtained from the image analysis of different subjects at different times.
- The definition of tailored time-evolving local references describing the geometry of the LV for any subject at any time. These local references provide an anatomical interpretation of scores obtained over the LV.

Our generic tools are applied to statistically modelling anatomy and function:

Anatomy Modelling. We use the NPD framework to compute an anatomic atlas that jointly models the LV gross anatomy (macroscopic structure) and its fiber architecture (microscopic structure). Given that fiber directions are difficult to interpret, we also develop a fiber coloring method providing an enhanced visual anatomic interpretation of their distribution inside the LV.

Function Modelling. We extract motion using HPF and use it to compute several (global and local) LV function scores. Regarding global scores we model ventricular rotation and torsion. Regarding local scores, we consider motion and several (directional and extremal) strains and compute segmental statistical models in the NPD. Finally, we explore for the first time, the performance of different configurations in order to determine the most appropriate for accurate RWMA detection.

1.2 Magnetic Resonance Imaging

Among the different modalities (Fig. 1.2), Magnetic Resonance Imaging (MRI) arises as the most versatile. By designing different acquisition protocols MRI is able to visualize either anatomical (external and internal), functional (including intramural motion) or physiological aspects of the heart. In addition, MRI presents a good spatial resolution, it is a non-ionizing technique and it is available in many clinical centers. In the present thesis we use two variants of MR: Diffusion Tensor Imaging (DTI) and Tagged Magnetic Resonance (TMR). On one hand, DTI studies provide anatomical volumetric data of both external and internal LV anatomy. On the other hand, TMR sequences allow the visualization of 2D intramural motion of the LV.

Diffusion Tensor Imaging

Most of the human body is made up of water. In general, thermal energy causes water molecules randomly move (diffuse) through tissue. However, at areas where the microstructure of tissue is well defined, diffusion restricts to such local architecture and becomes anisotropic. This is the case of fibrous structures like white matter in the brain or myocardial fibers in the heart. Mathematically, the 3D diffusivity at each point is represented by a real-valued symmetric matrix (tensor). DTI has the ability

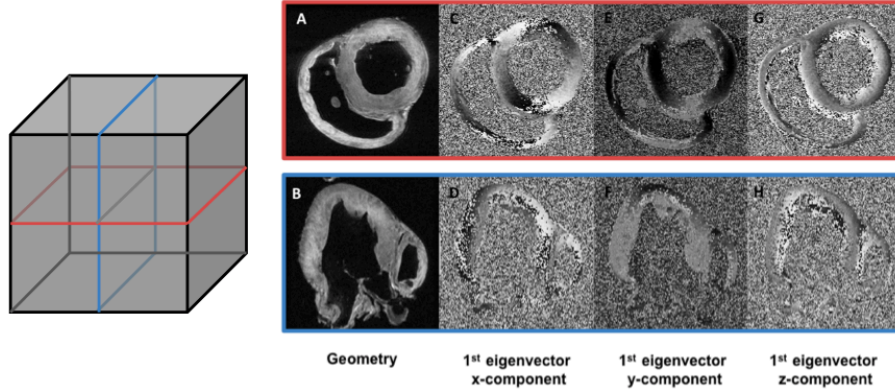


Figure 1.4: Slices of DTI volumes for 2 complementary planes: red (top row) and blue (bottom row). Geometrical volume in A and B. x , y and z components of DTI principal eigenvector in C, D; E, F and G, H respectively.

to measure such tensor at any point and, therefore, visualize the local structure of fibrous tissue. The diffusion tensor decomposes into a local eigensystem consisting of three mutually orthogonal eigenvectors representing the main diffusion directions and three eigenvalues corresponding to the diffusion rate. It has been shown [174] that the eigenvector associated to the higher eigenvalue (principal eigenvector) correlates to the main orientation of the myocardial fibers. Although it has been claimed that secondary and tertiary eigenvectors determine a laminar arrangement of the fibers [81], in this thesis we restrict to the principal eigenvector in order to study the architecture of the LV. After processing, DTI provides 2 main kinds of volumetric data. On one hand, the geometrical volume (also known as unweighted volume) is a single volume that at each voxel codifies the gross anatomy of the heart (Fig. 1.4 (A-B)). On the other hand, three volumes provide at each voxel the components of the principal eigenvector (Fig. 1.4 (C-H)). A main advantage of these volumes is that they are acquired without any motion artifact. Thus, all volumes share the same coordinates and segmentation performed on the geometric volume can be directly mapped to the eigenvector volumes.

Tagged Magnetic Resonance

TMR uses a special pulse sequence to selectively modulate the magnetic properties of the myocardium [16]. This pulse literally "prints" a set of tags forming a grid of saturated magnetization over the tissue. As the grid deforms by the underlying motion of the heart, it allows the visualization of intramural deformation. One of the main drawbacks of TMR sequences is that tags fade along time. Since by the end of the cardiac cycle tags can not be distinguished, in the present thesis we will restrict to the systolic cycle.

MR devices can be tuned in order to acquire tomographic slices in any desired

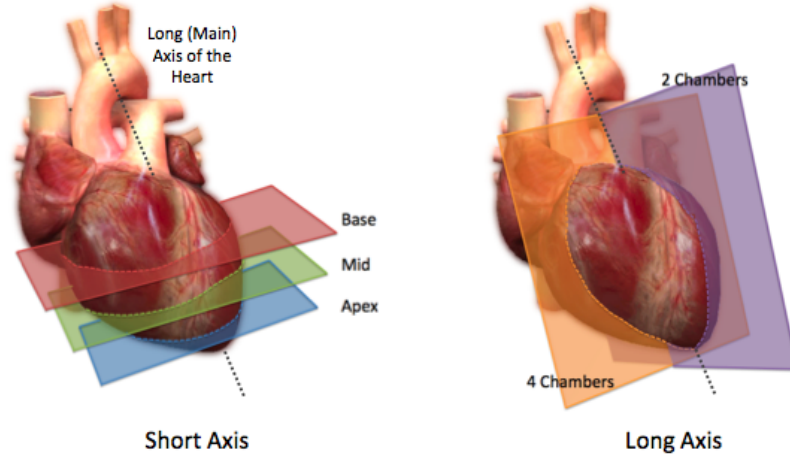


Figure 1.5: Standard acquisition slices. On the left image, we show slices perpendicular to the long axis of the heart (called short axis, SA) at the 3 levels (base, mid and apex) covering the whole LV. On the right image, we show the most common slices parallel to the long axis (called long axis, LA), These are the so called 2- and 4-chambers.

orientation. The standard acquisition protocol [36] establishes two sets of slices according to their orientation with respect to the main axis of the heart (defined as the line from base to apex). Tomographic slices perpendicular to the heart axis are called axial or short axis (SA), while those parallel to it are called longitudinal or long axis (LA). SA slices are usually acquired at three standard levels: base, mid and apex (see Fig. 1.5 left). The standard LA slices are 2-chamber and 4-chamber (see Fig. 1.5 right) views, since they allow the visualization of either the left atrium and ventricle (2 chambers) or both atria and ventricles (4 chambers). Figure 1.6 shows 4 frames (covering the systolic cycle) of 5 TMR sequences belonging to the standard SA and LA views. In SA sequences (first 3 rows) the LV present a 'O'-shaped structure, while in LA sequences (last 2 rows) is a 'U'-shaped structure. Notice how tag deform with tissue as the systolic cycle evolves.

1.3 An Overview of the State of the Art

Since the final applications of this thesis are anatomic and function models of the LV and, given that one of the goals is developing unifying tools, we report the state-of-the-art for anatomy and function modelling.

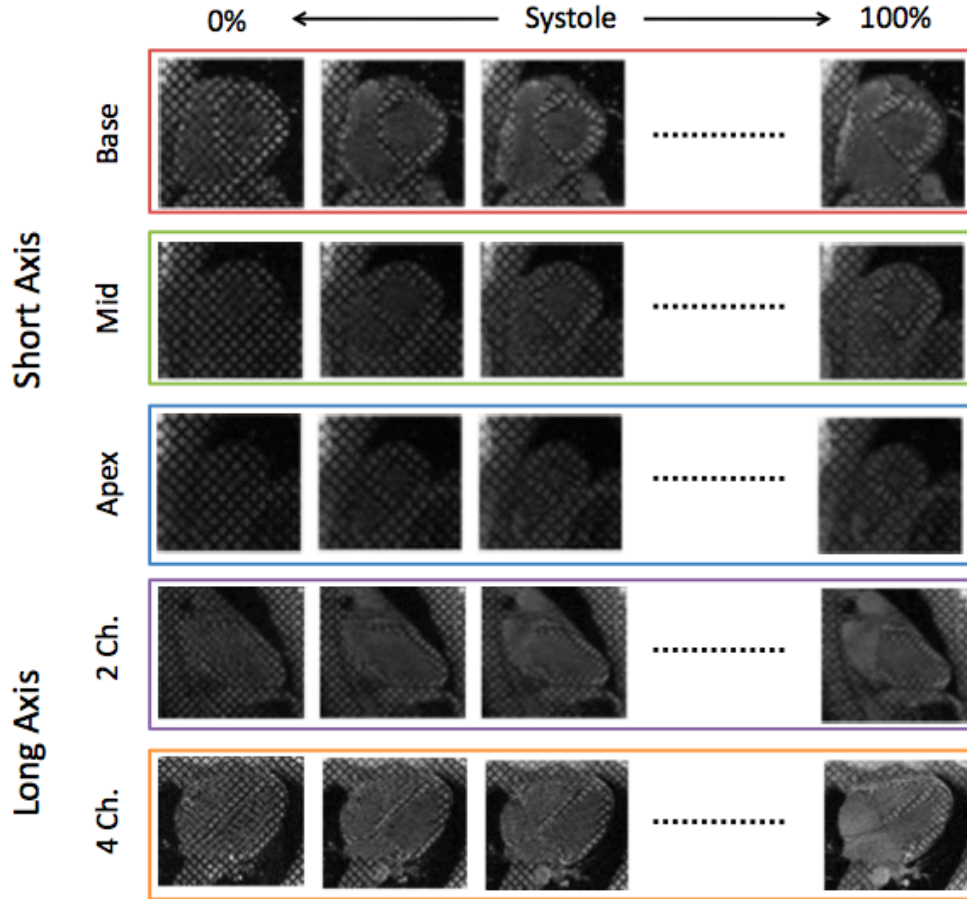


Figure 1.6: TMR sequences. The first 3 rows belong to the SA view and stand for basal, mid and apical tomographic slices respectively. The 2 bottom rows belong to the LA view and stand for 2- and 4-Chambers respectively.

1.3.1 Anatomy Modelling

Gross Anatomy

Data Extraction

The processing of medical images provides sets of landmarks, contours or image potentials that represent the main anatomic features to which geometric models representing LV gross anatomy are fitted. This fitting is done either minimizing the distance to the extracted points (e.g., least squares [29]), maximizing the similarity between image intensities (e.g., moments, correlation methods [140] or mutual information [118, 164]), or deforming an initial template under image-derived potentials

[28, 43, 91, 97, 125, 128, 166]. In any case, existing LV models may be split [65] into global and local approaches.

Global methods use simple geometric shapes given by a few number of parameters [57, 205] usually describing simple geometric primitives. In order to get shapes closer to the LV anatomy, some approaches combine several primitives. The model described in [35] combines a cylinder and an ellipsoid to obtain a kind of truncated bullet that resembles the LV wall. Other approaches [20, 127] use superquadrics since they include shapes that resemble cubes, octahedra, cylinders, lozenges or spindles, with rounded or sharp corners. An alternative way for obtaining a wider range of shapes, is considering a linear combination of basis functions with global support, such as surface harmonic descriptors [123], sinusoidal basis functions [180] or elliptical Fourier series [181]. The main drawback of global models is that the modification of any parameter affects the overall shape of the model, which often leads to rough approximations of the LV shape.

Local models use piecewise polynomial surfaces (such as bicubic Hermite patches or B-Splines [210, 213, 101, 171] or, recently, Doo-Sabin surfaces [144, 143]) in order to get models more adapted to local anatomic changes. Since each polynomial influences only a portion of the surface, such models ensure fine adjustments to the LV boundaries. In order to fit local models some authors use hybrid schemes [76, 117]. In these schemes global models are used to obtain a first approximation of the LV followed by extra deformations able to capture finer details of the LV.

Comparison Framework

The common approach to statistically model LV geometry in a given population consists of selecting a set of landmarks over the LV and concatenate their components into a single vector (called observation) that codifies the overall shape. Next, statistical analysis over a set of observations (training set) is performed. Since shapes should be independent on scale, orientation and position, such affinities are removed first. This is achieved by means of Procrustes Analysis [72] which aligns each shape so that the squared distance to the mean is minimized.

Statistical Analysis

The set of all aligned observations forms a cloud in a high dimensional space. Often this cloud is assumed to follow a Gaussian distribution. In such case, the population is modelled by fitting a new affine reference with the origin coinciding with centroid and the axes aligned to the ellipsoid-shaped cloud. This approach is commonly known as Point Distribution Models (PDM) [44]. The axes (called modes of variation) are given by the eigenvectors of the covariance matrix and describe the way in which shapes tend to move together. Eigenvectors corresponding to the largest eigenvalues describe the most significant modes of variation. Since the indicators are always partially correlated, most of the variation exhibited in the training set can usually be explained by a small number of modes. Hence, the dimension of the model can be reduced using Principal Component Analysis (PCA) [94]. PCA applied to shapes is commonly known as Active Shape Models (ASM) [46, 44] which have been widely

used to obtain 2D and 3D shape models of the LV in [46, 148] and [201, 124, 112] respectively.

PDM are discrete approaches which are based on the statistical modelling of a set of anatomical landmarks describing the geometry of the anatomical structure. By its linear formulation, PDM complexity and computational cost is very low which makes them useful in many computer vision applications (e.g. face segmentation). However, in the case of anatomical structures, the ability of PDM to capture the variability of finer details requires a massive selection of landmarks. This has led to designing computational methods [66] for the automatic generation of huge sets of landmarks over anatomical structures. The maximum resolution in the representation of shapes can be achieved by considering continuous models. Such models explore the variability of shapes by performing statistics directly over the diffeomorphic mappings required to register anatomies to a reference one [49, 80]. A main inconvenience is that the space of diffeomorphic mappings is an infinite dimensional space without vector space structure. This forces the development of special statistical models with a complex formulation.

Fiber Architecture

Data Extraction

Although the modelling of the LV gross anatomy has been widely addressed, the inclusion of its internal architecture is a relatively new issue. The exact distribution of myocardial is still unknown and controversial (see Sec. 2.2 for more details) but there is a general consensus that their architecture plays a critical role in myocardial function. Therefore, fiber architecture models should be taken into account in electrical and mechanical simulations applied to the planning of patient-specific therapies [176, 175].

Initially, histological studies were the only source of knowledge describing the myocardial architecture. However, the reconstruction of the entire ventricular fiber structure obtained from histological studies presents two main drawbacks. On one hand the reconstruction process can take several weeks per heart, and few laboratories have the expertise to do it. On the other hand, it can only be performed on fixed hearts, which fixation is prone to alter the fiber architecture. Recently, Diffusion Tensor Imaging (see Subsec. 1.2) has emerged as a new powerful tool for the rapid measurement of the whole cardiac architecture at a reasonable spatial resolution. DTI directly provides a 3D description of the fiber architecture and several authors have used them to study both, the fiber [68, 80, 186] and the laminar sheet [80, 186] orientations. These works, however, have been limited to the extraction of scalar values derived from the diffusion tensor such as inclination or insertion angles [81, 82]. Others have also studied the primary eigenvector values describing the fiber orientation in single subjects [186].

Comparison Framework

Comparison of different DTI studies is achieved by registering their geometric (unweighted) volumes to a reference volume (geometry). The deformation field obtained after the matching process is used to map scalar, vectorial or tensorial quantities to a common reference for the statistical analysis. A critical issue is the choice of the reference geometry, since it might hinder the matching if it is an outlying anatomy. One solution is registering volumes to average geometries [153]. Other approaches [137, 33, 81] use Large Deformation Diffeomorphic Metric Mappings (LDDMM) in order to find invertible transformation minimizing the impact of the reference anatomy.

Statistical Analysis

Few researchers have addressed the creation of statistical models (atlases) of the whole cardiac fiber architecture so far. This is mainly due to the fact that diffusion tensors are symmetric positive definite matrices that do not belong to any vector space. Thus, classical Euclidean multivariate statistics are not consistent. In [153] Riemannian geometry, based on either affine-invariant [63, 110, 151] or Log-Euclidean [12] metrics, have been used for the computation of first and second order statistics of the whole diffusion tensors.

In spite of the notorious break-through of DTI technology, in its current state it presents some shortcomings. The spatial resolution achieved by DTI is still far from the one provided by histological studies. Besides, since both, the preparation of hearts and the protocols for the acquisition of DTI volumes are complex, most studies restrict to few samples, usually of animal hearts. This leads to statistical analysis based on small populations that may result in biased models. A most important shortcoming is its high sensitivity to motion artifacts, which limits DTI acquisition to excised hearts (in-vitro). This fact impairs the creation of patient-tailored models of fiber architecture. Conscious about this, some authors have addressed mapping statistical atlases of myocardial architecture to the gross anatomy of alive subjects [186]. Given that most atlases have been created using canine hearts, the first step is to compare the canine mean fiber architecture to the orientation of a human heart. The study reported in [153] shows that there are no significant differences in fiber orientations among both species. This promising scenario enables the possibility of mapping an average fiber distribution to the gross anatomy to any subject, allowing the creation of patient-specific models of the heart. Such models would become a valuable tool for the design of tailored therapies such as resynchronization.

1.3.2 Function Modeling

Data Extraction

Currently, clinical routine involves the computation of global indicators such as ventricular volumes [93, 115, 191], ventricular mass [5, 61, 134], ejection fraction [191] or cardiac output. Such values can be easily obtained from conventional imaging techniques such as echocardiography [93, 19] or CINE magnetic resonance [150], and constitute a gold standard for subject assessment [115]. However, although these descriptors give an overall glimpse of the LV global function, they are unable to properly

localize RWMA [155]. Wall Motion (WM) provides a more localized assessment of the ventricular function [111, 121]. Coarser methods for WM detection are restricted to the endocardial wall [70, 129, 177, 178], whereas improved ones detect motion in both, endocardium and epicardium [7, 131, 96, 24, 142, 111, 121]. However, the lack of identifiable landmarks inside the myocardium, restricts the computation of WM along the normal (radial) direction, whereas the true motion also takes place along tangential (circumferential) direction and inside the tissue. It follows that WM is unable to properly detect RWMA. Local indicators have been proven to be more effective for the detection of RWMA [34]. The basis for the computation of local indicators is the extraction of motion inside the myocardial tissue.

First approaches for circumferential motion detection considered anatomical landmarks [214] which were restricted to myocardial coronary bifurcations. Eventhough standard techniques for interpolating and approximating were applied, the set of landmarks was too sparse to faithfully estimate motion. In addition, since coronary vessels run over the epicardium, motion estimation could not be extended to the whole LV. An alternative is considering implanted landmarks over the myocardium [204, 14]. Although more landmarks were available, a main inconvenient is its highly invasive nature, which limits its application to human hearts. Moreover, this technique still does not provide any landmark in the endocardium or midwall.

Currently the most extended approach for the computation of intra-mural motion consists of tracking induced landmarks over the LV tissue. The reference modality to estimate intramural motion is TMR although speckle imaging is gaining notorious repercussion [8, 79, 143]. Motion vector fields constitute themselves an indicator of local function and are used to derive several other local indicators such as strains. Strains are well suited to assess the local contractile behavior of the LV since they measure the local deformation suffered by an object (with respect to a reference shape) along any desired direction. The estimation of motion not only allows the obtention of such local scores, but also allows the computation of other global scores that were not fully available before. This is the case of ventricular rotation and torsion. Although they are oversimplified values, they reflect the overall cardiac function since they relate to the LV ejection and filling [79].

Regarding TMR, many image processing techniques have been developed in order to extract motion data. We might differentiate between those working in the image spatial domain and those working in its frequency (Fourier) domain. In the first group [211, 100, 77] the dark stripes are considered as target features to be tracked along the sequence. A main problem is that contrast between tissue and tags diminishes in time (fading effect [146]), which lows their performance at advance stages of the cardiac cycle. Furthermore these techniques lead to sparse displacement fields that have to be further interpolated to the whole myocardium. These drawbacks can be overcome by means of a variational approach modelling brightness variation. The most popular trends are optical flow techniques [55, 56, 154] for tracking motion and non-rigid registration [37, 104, 105]. Further approaches [41] provide a hierarchical (coarse to fine) decomposition of the displacement field using cosine orthogonal functions. Although they provide motion fields defined on the whole image, compensating the

fading effect [77] leads to complicated numeric schemes prone to reduce computational efficiency. In the second group we have the spectral methods which use frequency content of the tagged sequences to estimate motion. The most representative method in this group is the HARmonic Phase (HARP) [145, 146], which tracks the phase of the Fourier coefficients associated to the tagged pattern. Although such methods allow tracking motion at any time of the cardiac cycle they have two main limitations. On one hand, since they use a global Fourier transform they can not properly deal with inhomogeneous deformations usual at advanced stages of the systolic cycle. On the other hand, there is not any continuity constrain on the vector field which might lead to discontinuous fields at end-systole. In [15] modelling of tissue local deformation is addressed by using a bank of Gabor filters, but still no continuity on the vector field is forced.

Comparison Framework

Global clinical scores allow straightforward comparison across patients. However, in the case of local (or regional) values, a faithful comparison should ensure that each image region (pixel) always corresponds to the same anatomical location in the LV for any subject and systolic phase (handling intra- and inter-patient variabilities). We consider that current solutions might be split into explicit and implicit approaches.

Explicit approaches use image registration techniques (see [119, 216, 71] for a review). Along the last decades many registration methods have been developed. In intensity-based methods, image texture or grey levels are considered in order to put in correspondence the reference and target images [118, 140, 164]. Feature-based methods register images by point-by-point correspondence of a sparse set of anatomical landmarks common to any subject [172]. Finally, hybrid methods use a first coarse feature-based registration, followed by an intensity-based refinement [22, 137]. Any of these registration approaches, require the selection of an appropriate transformation model and the estimation of its parameters. The simplest ones are the affine (rigid) transformations [60, 140, 172] but, unless there is an affinity between the target and the reference images/objects (usually not the case in medical imaging) these are limited to be used as the first approach in hybrid methods. Otherwise rough registrations are obtained. Non-rigid (or elastic) methods are the most popular in medical imaging since they have the ability of locally warping the target to align with the reference more precisely. Several types of non-rigid transformations have been used: in [52] they use the ICP method [26] and in [37] Multilevel Free-Form deformations (MFFDs) [167]. Once a type of transformation is chosen (either rigid or non-rigid), in order to find the most appropriate parameters some criteria has to be optimized. If sparse features are considered, transformations often seek to minimize distance between same landmarks in both images using least squares [11] or the chamfer matching method [31]. On the other hand, when working with intensity-based methods, transformations are expected to maximize pixel/voxel similarity measures using moments, correlation methods [140] or mutual information [118, 164].

Registration approaches have two main weaknesses. On one hand, the election of the reference anatomy might introduce inaccuracies in the registration process if the chosen reference anatomy is an extremal of the population [27]. On the other hand,

registration does not provide intuitive coordinates for moving over the LV domain. Since this hinders the definition of anatomical segments, some approaches [164] require further processing.

Implicit approaches take place in an abstract level and are based on the subdivision of the LV in segments. By taking into account anatomical features, segments represent portions of tissue consistently defined for any subject, time and image modality. In this manner, inter- and intra-patient LV shape variations are removed and the values in each segment are comparable across subjects. The grounds for LV segment definition were established by the American Heart Association (AHA) [36] in order to standardize LV perfusion and function analysis among different image modalities. Their proposed 17-segment model arises as a tradeoff between anatomical considerations and usability in clinical practice. Although AHA partition has been extensively used [165, 212, 164], some authors [23, 42, 25, 189] consider more segments in order to provide more continuous approaches. Segment definition requires coordinate systems adapted to the LV anatomy. The default coordinate system in images is the Cartesian one. Cartesian (rectangular) coordinates are not the best suited in the case of curved surfaces like the LV (see the square regions in Fig. 1.7 (a), (d)). Moreover, any vectorial-dependent indicator defined over the LV (such as motion or directional strains) expressed in this rectangular coordinate system lacks of an anatomical meaning. The above limitations have motivated searching for alternative coordinate systems better adapted to the geometry of the LV. Usual changes include polar coordinates [106] for the 2D case, and cylindrical [53, 54, 189], spherical [212, 42], planispheric [51] or prolate spheroidal coordinates [141, 160] for the 3D case (fig. 1.7 (b), (c), (e)). These coordinates define segments better matching the LV geometry and provide more descriptive segments (see curved regions given by polar coordinates shown in Fig. 1.7 (e)). Besides motion can be decomposed into significant components (such as circumferential, radial or longitudinal [51]) and strains can be computed along such coordinate directions [54]. However, they still present two main shortcomings:

- Coordinate directions are a rough approach of the LV geometry and do not completely fit it. In other words, these coordinates model (parameterize) an oversimplified geometry unable to account for the patient-specific (local) anatomic shape of the LV.
- Coordinates are fixed (usually at end-systole) for all sequence frames, though the LV is an object which deforms along the cardiac cycle.

Statistical Analysis

The creation of normality patterns for global function indicators is straightforward and is given by the ranges (defined by $mean \pm std$) of scalar quantities. However in the case of local/regional indicators more elaborated approaches must be considered.

Like gross anatomy models, the overall approach concatenates all computed indicators (scalar values and vectors) of a given subject into a single vector. Such models

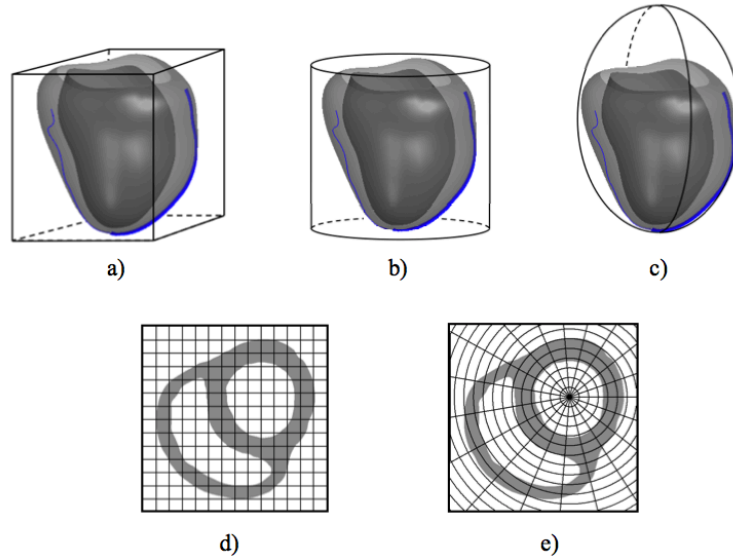


Figure 1.7: Different cardiac coordinate systems. Cartesian coordinates in a) and d) for 3D and 2D respectively. More adapted coordinates are cylindrical b) and prolate spheroidal c) for 3D; and polar e) for 2D.

are called Active Appearance Models (AAM) [45, 47] in the case of scalar values and Statistical Deformation Models (SDM) [159, 157, 158, 152] in the case of motion. In any case, statistical modelling is based on PCA analysis. A main drawback is that principal components given by PCA are not well suited for modelling regional behaviors. Several methods have been proposed to overcome this limitation. In [30] they use multivariate linear regression to select appropriate principal components, and in [111] they use sparse PCA. When the cloud of observations follow an unknown distribution, the common approach is to use Independent Component Analysis (ICA) [92] that inherently handles local behaviors of signals [185].

A common property of overall approaches is that feature vectors belong to high dimensional spaces. It follows that a large training set (often difficult to gather) might be required in order to obtain consistent statistical models. An alternative to overall approaches is to divide the LV in several segments and consider a different model for each of them. Segmental approaches are, by design, appropriated for straight evaluation of RWMA and might admit more reduced training sets. This last property allows modelling attributes along cardiac cycle or considering multiple descriptors. Local functional indicators have been modelled using this approach. In [119], they use a partition of the LV composed of 12 sectors along the circumferential direction, and 6 levels along the longitudinal one. Regarding radial direction, they just focus at midwall. In each region functional data analysis is applied in order to compute normal patterns of circumferential strain. In [133], 12 segments distributed into 4 sectors and 3 levels, is used. They also restrict computations at midwall, but they cover a wide

range of local function indicators such as circumferential, radial and longitudinal motion and strains, and several shears. Finally in [164] *1st-order* attributes are used to obtain AHA-based segmental descriptions of the LV function.

1.4 Main Contributions of the Thesis

The main contributions of this thesis are the following:

LV Motion Extraction. TMR images are characterized by two sets of linearly independent sparse features (tags) reflecting the intramural motion suffered by the myocardium along the cardiac cycle. These features have the main inconvenient of vanishing in time and present a high signal-to-noise ratio. In this thesis we propose a variational method (the Harmonic Phase Flow, HPF) which formulation gathers the estimation of motion of both sets of features and imposes smoothness constrains just at those areas where noise might affect tags. Since HPF provides a dense motion field over the whole LV, no further interpolation process is required. By using Gabor filter banks, HPF is able to track inhomogeneous tissue deformations all over the systolic cycle. Finally, the selective regularity constrain provides a smooth vector field which does not overestimate motion at injured areas.

Unifying Comparison Framework for Anatomical and Functional Data.

Although existing cardiac coordinate systems (prolate spheroidal, cylindrical,..) are usually referred to as LV parameterizations, from the point of view of Differential Geometry, they do not parameterize, indeed, the LV volume. This follows from the fact that coordinate curves do not fit the LV geometry, but other geometries (eg. cylinders) roughly approximating the LV true geometry. Although such coordinates significantly simplify computations, they are not accurate enough for defining neighborhoods (required for regional function assessment or statistical analysis). Furthermore, such coordinate systems require a further registration step in order to suppress across-subject variability and allow statistical analysis of regional scores.

In this thesis we introduce the Normalized Parametric Domain (NPD) framework which reports two main contributions. On one hand, we apply Differential Geometry concepts for defining a true parametrization of the LV volume (regarded as a manifold). Such a coordinate system tailored to each LV anatomy completely unfolds its geometry. Therefore the definition of neighborhoods adapted to the LV geometry is straightforward. On the other hand, by taking into account common anatomical features in the definition of the LV parametrization, we implicitly register LV domains. Since the parametric domain is always the unitary cube, one can define positions on the LV relatively to its boundaries. Besides, the NPD provides a comparison framework for local scores (e.g. fiber orientation and RWMA assessment) statistical analysis.

Anatomy Modelling. A trend in computational modelling consists on the design of patient-tailored models allowing a faithful representation of the LV anatomy.

This might require the fitting of anatomical atlases to the subject under consideration. However, current approaches for building anatomic statistical models of the LV, consider separately the gross geometry and the fiber architecture. In this thesis we propose using the NPD as unifying framework for modelling both of them. The formulation of the NPD framework, that relies on the parametrization (defined by means of B-Spines) of the LV in the manifold sense, provides an easy formulation and a computationally efficient implementation. On one hand, we use B-Spines control points in order to model the gross geometry of the LV as in Point Distribution Models. On the other hand, myocardial fibers are modelled in the NPD using Riemmanian metrics.

The fiber architecture has generated a heated debate in the literature with several proposed concepts (some of them) mutually incompatible. One of the most controversial concepts is the Helical Myocardial Ventricular Band (HMVB) of Dr. Torrent-Guasp. We have used the NPD framework for the definition of an anatomical-based colormap allowing the enhancement of the tissue structure. In particular, this coloring method allows the visualization of two concentric populations of fibers that might support the HMVB concept.

Function Modelling. In order to properly assess myocardial integrity, normality patterns of quantitative scores reflecting function are required. It has been shown that local scores are better suited for RWMA detection. However, up to our knowledge, current normality patterns address independent models for each score. We consider that in order to obtain more sensitive descriptors, the fusion of local scores should be taken into account. In this thesis the NPD framework is used to fuse several local indicators (2D displacement and different strains) in order to obtain multidimensional function descriptors. We have explored the performance of different configurations of these descriptors in order to seek the most appropriate for the detection of RWMA. The validity of these models is assessed separately for healthy and pathological population. For the first group leave-one-out error is used whereas, for the second, the ability to detect injured regions is evaluated using ground truth maps provided by several experts. Inter-observer variability is measured using ROC curves. Our statistical analysis suggests that the best LV functional feature space is given by 2D motion components and 2D maximum and minimal strains.

1.5 Structure of the Thesis

The thesis is structured as follows. In Chapter 2 we provide a brief background on anatomic and functional aspects of the heart, with special stress on the different concepts describing fiber architecture. Chapters 3 and 4 constitute the theoretical core and describe the main tools presented in this thesis, the Harmonic Phase Flow and the Normalized Parametric Domain respectively. In Chapter 5 the NPD framework is used in order to build an atlas jointly addressing the gross anatomy and the fiber architecture of the LV. In Chapter 6 NPD framework and HPF are used for the computation of normality patterns of, both, global and local function scores. Finally,

conclusions and future work are given in Chapter 7. Experiments are presented at the end of Chapters 3, 5 and 6.

Chapter 2

Anatomy and Function of the Heart

2.1 Gross Anatomy of the Heart

The heart is a muscular organ of the circulatory system that constantly pumps blood to deliver oxygen and nutrients to the cells, tissues and organs of the whole body. The heart is located in the chest between the lungs, behind the sternum and above the diaphragm. The heart size of an adult is about that of a fist, and its weight is about 250-300 g. Its gross anatomy can be decomposed into three main parts consisting of coronary vessels, chambers and valves.

2.1.1 Coronary Vessels

Heart delivers oxygenated blood to the whole body, including itself. Coronary vessels are the responsible of the circulation of blood inside the heart muscle. The vessels that deliver oxygen-rich blood to the myocardium are called coronary arteries, whereas those that remove the deoxygenated blood are called coronary veins.

The blood leaving the left ventricle exits through the aorta (the body's main artery) towards several parts of the body. Two coronary arteries, referred to as the "left" and "right" coronary arteries, emerge from the beginning of the aorta, near the top of the heart. The initial segment of the left coronary artery branches into two slightly smaller arteries: the left anterior descending coronary and the left circumflex coronary arteries. The left anterior descending coronary artery is embedded in the surface of the front side of the heart. The left circumflex coronary artery circles around the left side of the heart and is embedded in the surface of the back of the heart. The coronary arteries branch into progressively smaller vessels and, whereas larger vessels travel along the surface of the heart, the smaller branches penetrate the heart muscle (see Fig. 2.1 (right)).

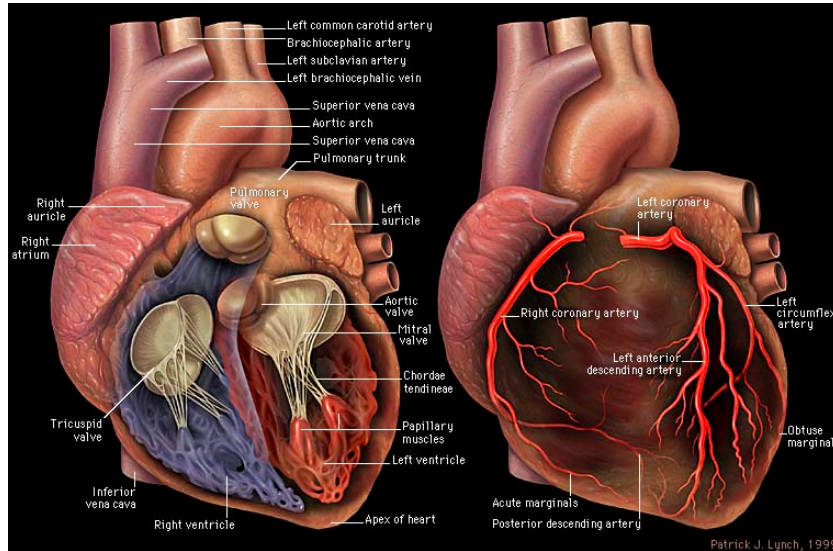


Figure 2.1: Location of the four valves of the heart (left), and the course of the main coronary vessels over the heart surface (right). Illustration by CC Patrick J. Lynch and C. Carl Jaffe, Yale University, 2006

2.1.2 Chambers

Four chambers may be distinguished in the heart. The upper ones are called left and right atria, and the lower ones Left and Right Ventricles (LV and RV, respectively). The common designation thus, splits the heart into right and left sides. Between both sides, a separating wall called septum (or septal wall) keeps the mechanisms of left and right sides apart. Muscular tissue including LV and RV is known as myocardium (see Fig. 2.2) and the outer and inner walls are called epicardium and endocardium respectively.

The two atria act as collecting reservoirs for blood returning to the heart while the two ventricles act as pumps to eject the blood to the body:

Right Atrium. Receives de-oxygenated blood from the body through the superior vena cava (head and upper body) and inferior vena cava (legs and lower torso). The tricuspid valve, which separates the right atrium from the right ventricle, opens to allow the de-oxygenated blood collected in the right atrium to flow into the right ventricle.

Right Ventricle. Receives de-oxygenated blood as the right atrium contracts. Once the ventricle is full, flows into the pulmonary artery towards the lungs.

Left Atrium. Receives oxygenated blood from the lungs through the pulmonary vein. As the contraction triggered by the sinoatrial node progresses through the atria, the blood passes through the mitral valve into the left ventricle.

Left Ventricle. Receives oxygenated blood as the left atrium contracts. The blood passes through the mitral valve into the left ventricle. The aortic valve leading into the aorta is closed, allowing the ventricle to fill with blood. Once the ventricle is full, it contracts, the mitral valve closes and the aortic valve opens. The closure of the mitral valve prevents blood from backing into the left atrium and the opening of the aortic valve allows the blood to flow into the aorta and flow throughout the body.

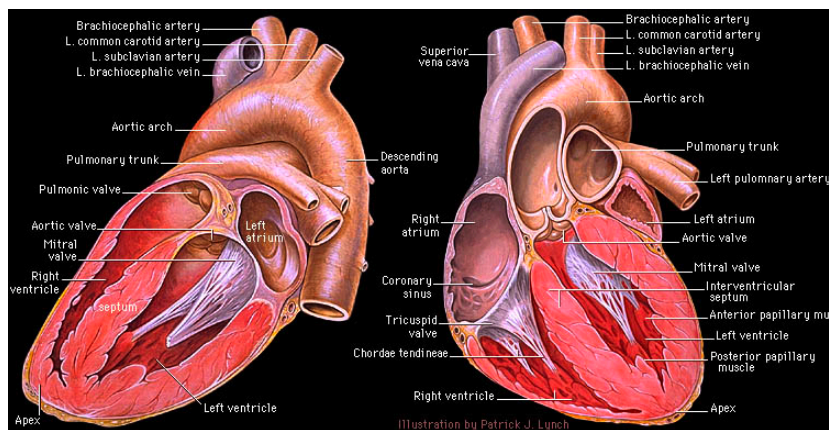


Figure 2.2: Two longitudinal cuts of the heart showing the main structures of the heart. Illustration by CC Patrick J. Lynch and C. Carl Jaffe, Yale University, 2006

2.1.3 Valves

As in any pumping system, the heart comes complete with valves to prevent the back flow of blood. Four valves are found in the heart (see Fig. 2.1 (left)):

Tricuspid Valve. The tricuspid valve separates the right atrium from the right ventricle. It opens to allow the de-oxygenated blood collected in the right atrium to flow into the right ventricle. It closes as the right ventricle contracts, preventing blood from returning to the right atrium; thereby, forcing it to exit through the pulmonary valve into the pulmonary artery.

Mitral Value. The mitral valve separates the left atrium from the left ventricle. It opens to allow the oxygenated blood collected in the left atrium to flow into the left ventricle. It closes as the left ventricle contracts, preventing blood from returning to the left atrium; thereby, forcing it to exit through the aortic valve into the aorta.

Pulmonary Valve. The pulmonary valve separates the right ventricle from the pulmonary artery. As the ventricles contract, it opens to allow the de-oxygenated blood collected in the right ventricle to flow to the lungs. It closes as the ventricles relax, preventing blood from returning to the heart.

Aortic Valve. The aortic valve separates the left ventricle from the aorta. As the ventricles contract, it opens to allow the oxygenated blood collected in the left ventricle to flow throughout the body. It closes as the ventricles relax, preventing blood from returning to the heart.

The valves are able to perform efficiently their task thanks to the papillary muscles and the chordae tendineae. The papillary muscles attach to the lower portion of the interior wall of the ventricles. They connect to the chordae tendineae, which attach to the tricuspid valve in the right ventricle and the mitral valve in the left ventricle. The contraction of the papillary muscles opens these valves. When the papillary muscles relax, the valves close. The chordae tendineae are tendons linking the papillary muscles to the tricuspid valve in the right ventricle and the mitral valve in the left ventricle. As the papillary muscles contract and relax, the chordae tendineae transmit the resulting increase and decrease in tension to the respective valves, causing them to open and close. The chordae tendineae are string-like in appearance and are sometimes referred to as "heart strings."

Although the microscopic level of the heart has been widely studied, there is an intermediate step that still represents a main obstacle in order to fully understand the cardiac function. The heart architecture, linking the microscopic to the macroscopic myocardial structure, allowing to perform the pumping action with optimal mechanical efficiency.

2.2 Fiber Architecture of the Heart

The approximate helical architecture of the heart has been known for centuries [116] (Fig. 2.3). Nevertheless, a complete and consistent anatomical description of cardiac structure has not been achieved yet. This issue is currently one of the most controversial aspects of the modern cardiology and, several conceptual architectural models have been proposed [69] so far. Some of them seem to be mutually incompatible while others may be true representations of the heart when considered from different perspectives. There is, however, a general consensus that cardiac architecture plays a critical role in many functional aspects of the heart, such as electrical propagation [162, 187] or force production [109]. In addition, it is also accepted that myocardium may undergo architectural alterations in many heart diseases [163, 190, 208] and in arrhythmogenesis [39]. It is, thus, a field of huge interest that may benefit either surgical procedures and resynchronization therapies.

The main aim of the myocardial architecture conceptual models is to give a description of the spatial distribution of myocardial fibers agreeing with dissectional-, histological- and imaging-based observations. Such conceptual models, in addition, should provide maximal mechanical efficiency in the systole and diastole processes and explain the observed gross function of the heart.

Giving a definition of myocardial fiber is not an easy task. In contrast to the skeletal muscle, which fibers gather in distinct parallel bundles (see Fig. 2.4 (a) and

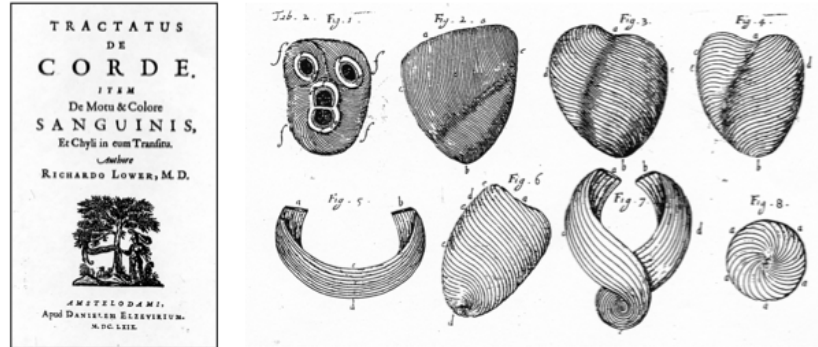


Figure 2.3: In his *Tractatus de Corde* (1669), Richard Lower already described the approximate helical structure of the heart.

(b)), myocardial fibers do not arrange into any structure (corresponding to a 'fiber') such as one can isolate. The myocardial body consists of aggregates of myocytes joined via intercalated discs at their ends that branch [64, 90] from one to another forming a three-dimensional net (see Fig. 2.4 (c) and (d)). Still, despite this fiber branching, they follow a preferential pathway minimizing the variation of the orientation along successive myocytes (Fig. 2.4 (c)). This preferred pathway constitutes the concept of myocardial fiber.

Ventricular myocardium has been shown to have a complex laminar structure, in which myocytes are grouped by perimysial collagen into branching layers (myolaminae) \approx 4 cells thick [13, 40, 48, 108, 174, 215] (see Fig. 2.5). Adjacent layers branch and interconnect, but are separated by "cleavage planes", across which direct myocyte-to-myocyte coupling is absent [108]. The laminar structure was already described in detail in [88, 87, 89]. However, the first quantitative histological analysis was not performed until [108] and further mathematical models were not obtained until [107]. Although this structure have been recognized by most researchers, some of them have played down its significance, emphasizing instead the mesh-like nature of cardiac structure [10].

2.2.1 Techniques for Measuring Cardiac Architecture

Traditionally, cardiac architecture observations and measurements have been obtained by means of dissectional [62, 73, 74, 99, 113, 120, 161, 168, 170, 195] and histological [64, 90, 108, 182, 183] studies. A main advantage of dissection techniques is that they allow to observe (naked eye) the overall cardiac architecture. In contrast, histological techniques used in conjunction with confocal or electron microscopy allow the visualization of portions of tissue at high resolution. However, such techniques present several drawbacks. On one hand, the dissectional studies are considered to be destructive, irreproducible and quantitative measurements difficult to obtain. On the other hand, reconstruction of the entire ventricular fiber microstructure from histological

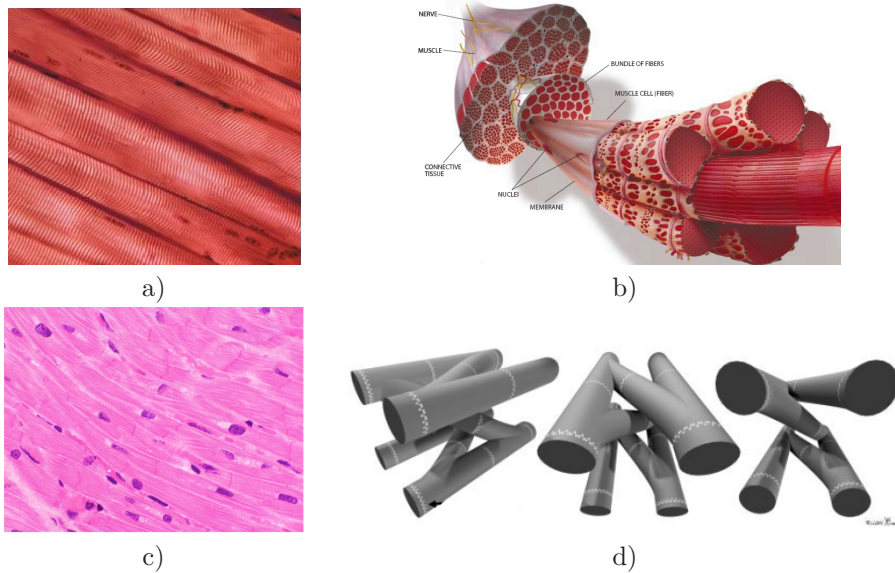


Figure 2.4: Different muscular fibers. a) Appearance of the skeletal muscular fiber bundles. They appear completely parallel each other, without branching. b) Illustration of the morphology of the skeletal muscle fibers. c) Appearance of myocardium (stained with H & E at roughly 400x) in a light microscope. Branching myocardial fibers can be appreciated. Despite of this, a main direction is visible. d) 3D scheme of the locally branching fibers (image from [10]).

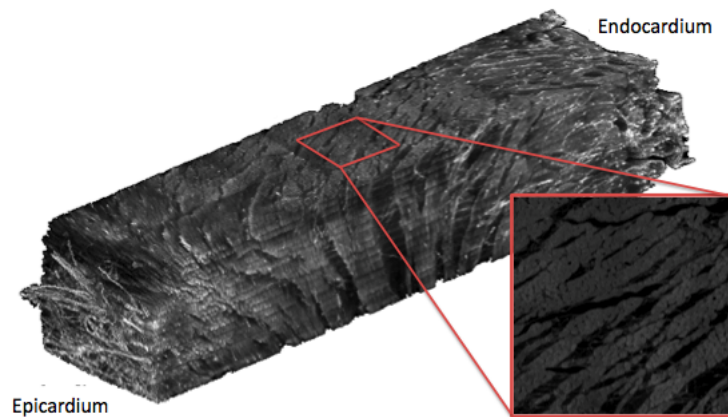


Figure 2.5: Oblique view of extended volume image from left ventricle of rat heart obtained using confocal microscopy. Note the laminar organization of myocytes. In the detail, section perpendicular to myocyte axis. (Image from the Royal Microscopical Society).

slices can take several weeks per heart and few laboratories have the expertise to do it. Furthermore, reconstruction can only be performed on fixed hearts and fixation may alter the architecture from the normal viable state [174].

Recently, Diffusion Tensor Imaging (DTI), a technique for measuring the self-diffusion of protons in fibrous tissue, has emerged as a powerful new tool for the rapid measurement of cardiac architecture at high spatial resolution. DTI provides a 3-dimensional tensor which diagonalizes in three orthogonal eigenvector. Histological studies have demonstrated that the primary eigenvector correlates well to myofiber direction [174] and that the secondary and tertiary eigenvectors are tangent and normal to the myolaminae plane [137, 38, 40, 81, 83, 199]. By the same time, new microscopic techniques using polarized light (PL) analysis have been thoroughly developed [200] for the analysis of muscular fibers.

Contrarily to DTI, PL is able to capture only principal direction of myofibers misleading sheet structures. Such structure is codified by secondary and tertiary eigenvectors (in DTI). However, it has been hypothesized [82, 199] that a sorting problem can occur when the magnitudes of both eigenvectors are similar, invalidating the estimated laminar structure. A further PL limitation concerns the range of definition of some measurements. More precisely the elevation angle can not be fully measured.

A main advantage of these imaging techniques is that they provide digital data sets prone to be statistically studied but, a common drawback, concerns their (low) spatial resolution. The resolution of DTI is approximately $300 \times 300 \times 1000 \mu\text{m}^3$ and although PL outperforms such resolution with $100 \times 100 \times 500 \mu\text{m}^3$ it still may be not enough to fully capture fiber and sheet structures ($\approx 50 \mu\text{m}$ [108]).

Since each technique may be appropriate to to visualize/measure architectural information at different levels, it is not surprising that many models coexist. This suggests that in order to obtain a faithful description of the fiber architecture, the association of several of the former techniques might be required.

2.3 Conceptual Models of Cardiac Architecture

Along the last century several (at least 7) conceptual models trying to describe the architecture of the heart have been proposed and none of them has clearly blunt among the others. Figure 2.6 describes current heart architecture concepts in chronological order. Despite the technical advances in medical imaging, all models (even the latest ones) base on dissectional and histological studies.

The first models were developed by means of dissectional techniques (first row in Fig. 2.6). This group includes the Distinct Muscle Bundles (DMB) model stated by Rob and Rob in 1942 [161], the Three-Layered Ventricle (TLV) model proposed by Rushmer in 1953 [168] and Torrent-Guaspar Helical Myocardial Ventricular Band (HMVB) in 1954 [192]. Most recent models have been formulated by means of histological techniques (second row in Fig. 2.6), supported by microscopy technologies

systolic function. Further studies [74] have endorsed this model while (paradoxically) also accepting that the separation of layers is artificial since the orientation of fibres changes gradually.

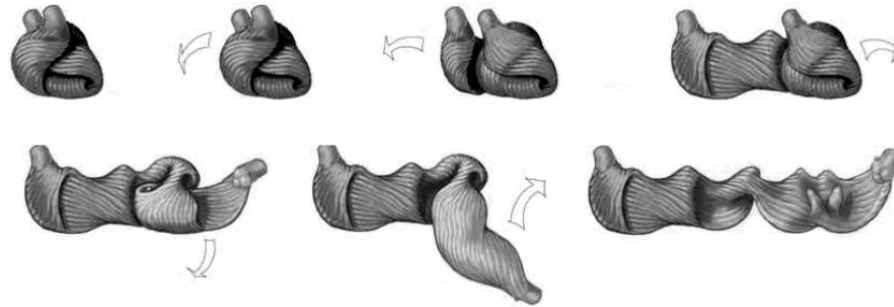


Figure 2.7: Unfolding the HMBV. Different stages of the systematic dissection process of the heart.

2.3.2 Helical Myocardial Ventricular Band Model

The Helical Myocardial Ventricular Band concept was developed during the last 50 years by Dr. Torrent-Guasp after more than 1000 anatomical dissections of hearts belonging to different species [98]. He discovered certain areas where the courses of bundles of fibers crossed each other in different planes (cleavage planes). These planes provided landmarks for a systematic unfolding (dissection) of the ventricular band. From such dissection process he concluded that the complex structure of the myocardium is due to a double-loop helical orientation of a single muscular band that extends from the pulmonary artery to the aorta, with a 180-degree twist in its middle part [193, 194, 196] (see Fig. 2.7). Over the band, he distinguished four segments (see their complex spatial distribution in Figure 2.8): right segment (RS), left segment (LS), descendent segment (DS) and ascendent segment (AS); playing a crucial role in the heart function. Torrent-Guasp suggested that ventricular electromechanical activation is anisotropically propagated following the myocardial band and takes place in the following sequence: right ventricular segment and left ventricular segment (basal loop) → descendant segment → ascendant segment (apical loop); and such propagation would explain the gross cardiac function. After contraction of the basal loop has taken place, subsequent contraction of the descendant segment pulls the basal loop downward and toward the apex, thereby shortening the longitudinal axis of the ventricular cavities, reducing its volume, and twisting the base clockwise and the apex counterclockwise leading to ventricular ejection. Contraction of the ascendant segment follows, which generates a rapid upward displacement of the base of the heart that increases the ventricular longitudinal axis and volume and untwists the ventricles. Thus, the HMVB arises not only as an anatomic but also functional model that allowed to predict cardiac mechanics before the first magnetic resonance descriptions appeared in the literature [197, 114, 133]. The ventricular myocardium is described to work as an agonist-antagonist unit [84].

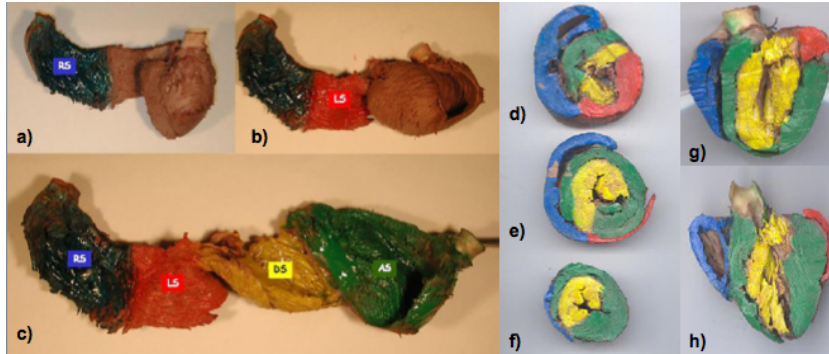


Figure 2.8: Scheme of the colored band segments (a)-(c). The right ventricle (blue) and upper portion of the left ventricle (red) form the basal loop. The descendant (yellow) and ascendant (green) segments form the apical loop. AS, ascendant segment; DS, descendant segment; LS, left segment; RS, right segment. The complex spatial distribution of these segments can be appreciated by wrapping the band again and obtaining axial (d)-(f) and longitudinal (g), (h) slices.

Implications of the HMVB

The HMVB has notorious implications in several fields in which the impact is presumed to be of importance:

- The anatomy of the band might explain why diastolic dysfunction occurs before systolic alteration of function. Early diastolic dysfunction before systolic dysfunction seen in diseases such as hypertension and other entities could be explained by damage-associated hypertrophy [203] first involving the thinner ascendant segment and later the more robust descendant segment.
- In surgery for heart failure, it seems appropriate once the helical conformation of the ventricle is known, to plan surgery in such a way as to spare the helical ventricular anatomy. In an initial study by Torrent-Guasp and colleagues [67, 198], they proposed four theoretic possibilities of surgically reducing left ventricular volume without impairing the helical structure of the ventricles were considered. The most logical approach seems to spare the apical loop (small volume and the true motor of the ventricle) and reduce the basal loop.
- In resynchronization therapy, an explanation of why some patients respond to the device implantation whereas others fail to improve is not forthcoming. The issue is not that the left ventricle should contract simultaneously (most of the indexes developed are aimed at the detection of this phenomenon); rather, what is crucial is the sequence of contraction of the descendant and ascendant segments. In fact, knowledge of the natural sequence of electromechanical ventricular activation [17, 1] should open the way to study the effects of selective stimulation of the segments of the band on ventricular function, and should provide a rationale for ventricular pacing protocols.

Controversies about the HMVB

The HMVB concept has arisen as one of the most controversial models. There are two main sources of criticism. The first concern, common to all dissectional techniques, is the reproducibility of the dissection process. In the case of the HMVB, however, the unfolding process follows anatomical landmarks that can be systematically identified, thus, ensuring reproducibility. The second and most powerful criticism comes along with some evidences that point to a smooth change in fiber orientation across the myocardium [9, 10]. The main opponents claim that if fiber angle changes smoothly across the wall, the myocardial band cannot exist. However, recent evidences pointing to two sheet populations, could prove that the HMVB unfolding process follows measurable anatomic features.

2.3.3 Simple and Complex Laminar Structure Models

The Simple Laminar Structure model (Fig. 2.6 (e)) states that the myocardial wall consists of an ordered laminar structure, separated by extensive cleavage planes that run approximately radially from endocardium to epicardium. In tangential sections the plane of the laminae coincides with local fiber orientation. Layers are about 4 ± 2 myocytes across and $48.4 \pm 20.4 \mu m$. thick (in the dog). Components of the connective tissue matrix connect adjacent laminae.

The Complex Laminar Structure model (Fig. 2.6 (g)) is still an early model that needs to be formalized or organized into a complete conceptual model. It reveals, for the first time, alternating transmural families of predominant sheet angles. This may have important implications in understanding wall mechanics in the normal and the failing heart.

2.3.4 Nested Doughnut and Pretzel Geodesics Models

The Nested Doughnut Geodesics model, also known as Streeter's conjecture, is a topological model restricted to the LV that assumes myocardial fibers to run like geodesics (paths of shortest length) on a nested set of toroidal bodies of revolution (doughnuts). The formulation of this conjecture was based on a very limited sample of the LV wall [136]. Was in [4] where NDG was formally validated to the whole LV (at least for fetal life), using a property of the geodesics. The condition that geodesics running on surfaces with symmetry of revolution have at each point an equal value of the Clairaut constant $r \cos(\theta)$ (for r is the distance of the considered point to the axis of revolution and θ is the angle) was confirmed to happen in the LV.

In [95], Streeter's conjecture was extended to the whole myocardium by formulating the Nested Pretzel Geodesics topological model. So far, such model elaborated by visually analysis of fetal subjects, stands as a conjecture and further mathematical and experimental validations are still to be done. NPG states that fibers run also in the right ventricle like geodesics on a nested set of toroidal bodies that are no more of

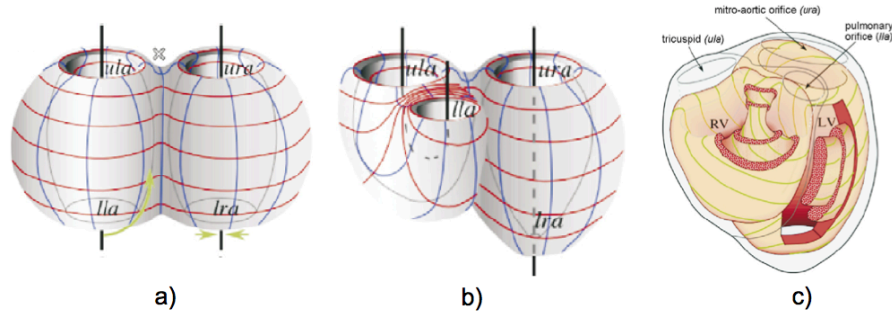


Figure 2.9: Construction of the Nested Pretzel Geodesics model from two joined tori.

revolution. To understand this model, see Figure 2.9 where two tori form a 'pretzel' with a lattice on the surface to grasp further deformations (in blue the meridians, in red the parallels, lla: lower left aperture; lra: lower right aperture; ula: upper left aperture; ura: upper right aperture). The torus on the left is bent in such a way that the lower aperture comes up close to the upper aperture (RV) and the lower aperture of the right torus constricts to a point where no lumen is left (LV). Notice that the topological model restricted to the LV coincides with the NDG.

NPG has been compared to the HMVB model and reported conclusions state that, during fetal period, there is clearly no compatibility between them. However, they also recognize that after birth, major adaptations occur and some evidences supporting the HMVB emerge.

2.4 Gross Function of the Heart

The overall pumping action of the heart starts with the simultaneous contraction of the two atria. This contraction serves to give an added push to get the blood into the ventricles at the end of the slow-filling portion of the pumping cycle called "diastole." Shortly after that, the ventricles contract, marking the beginning of "systole." The aortic and pulmonary valves open and blood is forcibly ejected from the ventricles, while the mitral and tricuspid valves close to prevent backflow. At the same time, the atria start to fill with blood again. After a while, the ventricles relax, the aortic and pulmonary valves close, and the mitral and tricuspid valves open and the ventricles start to fill with blood again, marking the end of systole and the beginning of diastole. It should be noted that even though equal volumes are ejected from the right and the left heart, the LV generates a much higher pressure than does the right ventricle. Certainly the LV is the most important chamber in the heart since is the responsible to deliver oxygenated blood to any part of the body.

This overall pumping action arises as the net result of several electrophysiologic mechanisms taking place in a microscopic level. The myocardial cells (myocytes) ex-

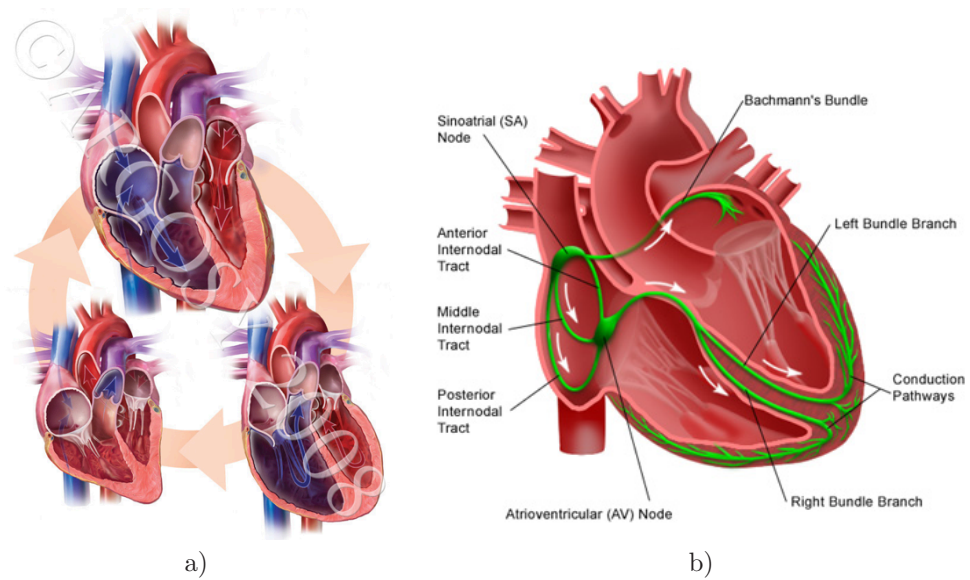


Figure 2.10: Electromechanics of the heart: a) pumping action of the heart (cardiac cycle) and b) electrical system.

periment a change in voltage across their membrane (depolarization), which leads to an action potential. Although contraction may happen spontaneously, it is normally in response to an electrical impulse. This impulse starts in the sinoatrial (SA) node, a collection of pacemaker cells located at the junction of the right atrium and superior vena cava. These specialized cells depolarize spontaneously, and cause a wave of contraction to pass across the atria. Following atrial contraction, the impulse is delayed at the atrioventricular (AV) node, located in the septal wall of the right atrium. From here His-Purkinje fibres allow rapid conduction of the electrical impulse via right and left branches, causing almost simultaneous depolarization of both ventricles, approximately 0.2 seconds after the initial impulse has arisen in the sinoatrial node. Depolarization of the myocardial cell membrane causes a large increase in the concentration of calcium within the cell, which in turn causes contraction by a temporary binding between two proteins, actin and myosin. The cardiac action potential is much longer than that of skeletal muscle, and during this time the myocardial cell is unresponsive to further excitation.

Chapter 3

Harmonic Phase Flow

In this Chapter, we provide a novel variational approach to the computation of LV motion observed in TMR sequences. Firstly, we introduce a bi-dimensional representation space for TMR images given by a filtering process using Gabor filter banks. The phase of the Gabor responses is a property of tissue that remains constant along the cardiac cycle [145] and is closely related to local deformations [18]. Meanwhile, the amplitude of the Gabor response indicates the reliability of the local pattern detected by the Gabor filter. Secondly, we define a functional in a Sobolev space [59] combining the optical flow [86] of the two Gabor phases into a variational framework which regularizes the deformation field just at areas where the Gabor amplitude drops. The resulting deformation map is a dense and continuous vector field which we call Harmonic Phase Flow (HPF). The method accuracy has been tested using, both, synthetic dynamic phantoms and real sequences manually marked by an expert.

3.1 Harmonic Images

Spatial Modularization of Magnetization (SPAMM) [16] is a tagging protocol that allows "printing" two sets of tags over the myocardium at initial time (end-diastole). Each set of tags is generated by applying several hard radio frequency pulses along two perpendicular directions, $\omega_1, \omega_2 \in \mathbb{R}^2$. These tags deform by the underlying motion of the heart, allowing the visualization of intramural motion. The main inconvenient of SPAMM is the fading effect (tags vanish in time), which restricts its use to the systolic cycle.

Mathematically, any frame of a TMR sequence $\{I(x, y; t)\}_{t=0}^{T_{ES}}$ might be expressed [146] as the following sum:

$$I(x, y; t) = \sum_{r,s=0}^{R,S} I_0(p(x, y; t))c(t)e^{i(W_{r,s,p}(x,y;t))} = \sum_{r,s=0}^{R,S} I_{r,s}(x, y; t) \quad (3.1)$$

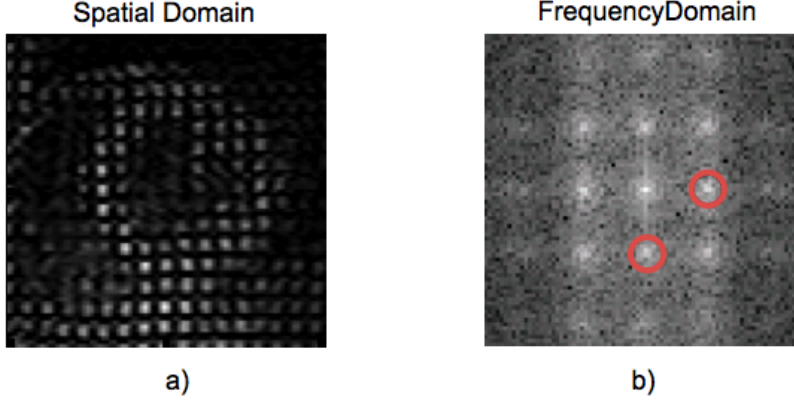


Figure 3.1: Harmonic peaks. a) Frame in the spatial domain tagged using 2 hard frequency radio pulses along vertical and horizontal directions. b) In the frequency domain 25 harmonic peaks, each corresponding to an harmonic image. Circles indicate the main harmonic peaks associated to the main harmonic images.

for $W_{r,s} = r\omega_1 + s\omega_2$, R and S depending on the number of applied radio frequency pulses; $p(x, y; t)$ the reference map that relates a spatial point (x, y) at a given time t to its associated material point at time $t = 0$; $\langle \cdot, \cdot \rangle$ the scalar product; I_0 the underlying ordinary MR image (without tags) and c a function modelling the fading effect. The $I_{r,s} \in \mathbb{C}$ images are called harmonic images. Thus, any tagged frame is a sum of complex harmonic images. In the frequency domain, each harmonic image produces an harmonic peak (see Fig. 3.1).

Note that the phase of the harmonic images, $\Phi_{r,s}(x, y; t) = \langle W_{r,s}, p(x, y; t) \rangle$, is defined by a linear relation between the tagging frequency and the reference map [146]. This fact indicates that phase is a property of tissue that remains constant along the systolic cycle. Thus, these phases are good candidates for tracking purposes. Since, in practice, phase cannot be properly retrieved, the principal wrapped value [146, 179] defined in the range $[-\pi, \pi)$ is used instead. This is called angle image, $a_{r,s}$, and it provides motion information in a direction close to $W_{r,s}$.

In order to extract 2D motion, two angle images associated to linearly independent harmonic frequencies are required. We will use angle images associated to the main frequencies $W_{1,0} = \omega_1$ and $W_{0,1} = \omega_2$. $I_{1,0}$, $I_{0,1}$ are the main harmonic images and $a_{1,0}$, $a_{0,1}$ the main angle images. From now on, we will note them I_1 , I_2 , a_1 and a_2 for short.

3.2 Tracking Issues

In image processing terms, tracking [86, 21] addresses finding the trajectory of a given object in an image sequence. In a mathematical framework, object tracking turns into

determining a vector field $V(x, y; t)$ for each time t , best matching two consecutive frames.

One of the most popular approaches for motion tracking is the Optical Flow [86]. Such technique relies on the assumption that the intensity of image structures keeps approximately constant. This is, for any point (x, y) in the image $I(x, y; t)$, at a small time later, its intensity must keep constant. This condition is formulated as

$$I(x + dx, y + dy; t + dt) = I(x, y; t) \quad (3.2)$$

Applying the Taylor formula, the left term in equation (3.2) becomes

$$I(x + dx, y + dy; t + dt) = I(x, y; t) + \frac{\partial I}{\partial x} dx + \frac{\partial I}{\partial y} dy + \frac{\partial I}{\partial t} dt + \dots \quad (3.3)$$

where the dots stand for higher order terms. Substituting equation (3.2) in equation (3.3) and keeping the first order term, we get

$$\frac{\partial I}{\partial x} dx + \frac{\partial I}{\partial y} dy + \frac{\partial I}{\partial t} dt = 0 \quad (3.4)$$

Dividing through by dt , we have

$$\frac{\partial I}{\partial x} u + \frac{\partial I}{\partial y} v + \frac{\partial I}{\partial t} = 0 \quad (3.5)$$

for

$$\frac{dx}{dt} = u \quad \frac{dy}{dt} = v \quad (3.6)$$

which is called the optical flow constraint equation.

Lets denote $V = (u, v)$, $I_x = \frac{\partial I}{\partial x}$, $I_y = \frac{\partial I}{\partial y}$, $I_t = \frac{\partial I}{\partial t}$ and $\nabla I = (I_x, I_y)$. Then, equation (3.5) may be reformulated as

$$\langle \nabla I, V \rangle + I_t = 0. \quad (3.7)$$

We note that, from a mathematical point of view and under the brightness constancy assumption, object tracking converts into finding the isosurfaces of the uni-parametric family of images, $I(x, y; t)$, defining the sequence. Since only one equation (3.7) is available, in order to uniquely determine the two unknowns (u and v) smoothness constraints are usually added.

In our case, tagged sequences fail at the condition of brightness constancy due to the fading effect. Nevertheless, we have seen that angle images fulfills it. Thus, equation (3.7) will be applied to the angle images a_1 and a_2 . Moreover, since we have

two different images related to tissue motion, u and v might be fully determined by solving the optical flow system independently for each point:

$$\begin{cases} \langle \nabla a_1, V \rangle + a_{1t} = 0 \\ \langle \nabla a_2, V \rangle + a_{2t} = 0 \end{cases} \quad (3.8)$$

We note, however, that this would yield irregular vector fields since there is no constraint on the spatial continuity of the vector. In the following section, we use these equations in a variational framework as matching term, in order to obtain continuous deformation maps.

3.3 Harmonic Phase Flow

3.3.1 Retrieving Angle Images

In order to obtain the angle images associated to a given tagged frame, its main harmonic images ($I_1, I_2 \in \mathbb{C}$) need to be determined (i.e., filtered). If tags were a regular grid, band pass Gabor filters centered at the main spectral peaks, (ω_1, ω_2) , would suffice. However, grid regularity just holds at initial time and as the systolic cycle evolves, tags lose their initial ideal shape. Thus, the previous filter would give lower response in most of the myocardial regions. The highest response are given, at each point, by the Gabor filter with the most similar frequency and scale of the underlying tag pattern.

A Gabor filter is the product of a complex sinusoid, that determines the frequency, by a gaussian envelope that determines the scale.

$$\Gamma(x, y) = C \underbrace{e^{-i2\pi(\frac{\omega_x x}{W} + \frac{\omega_y y}{H})}}_{\text{Frequency}} \cdot \underbrace{e^{-\frac{(x')^2 + (\lambda y')^2}{2\sigma^2 x'}}}_{\text{Scale}} \quad (3.9)$$

Each part of the Gabor filter formula has its own parameters that can be independently tuned:

- *Frequency Parameters* (see Fig. 3.2 (a)):
 - $\omega = (\omega_x, \omega_y)$ is a 2D vector that determines the frequency and the orientation of the pattern with its norm and angle respectively.
 - H and W determines the height and the width of the window in which we define the filter. These parameters are fixed and have the same values as the image to be filtered.
- *Scale Parameters* (see Fig. 3.2 (b)):

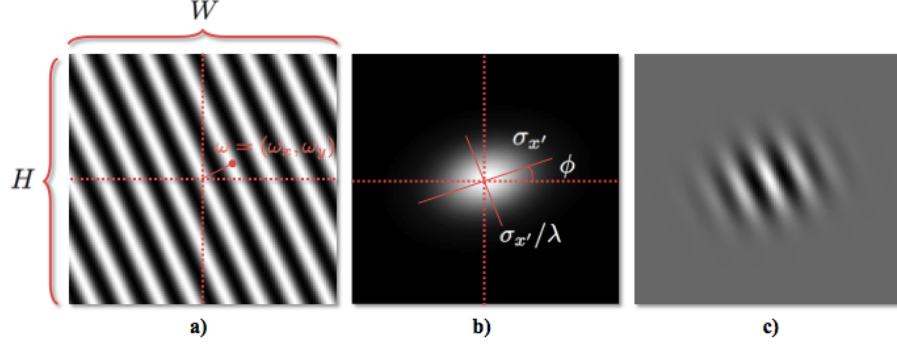


Figure 3.2: a) Real part of the complex sinusoid. The norm of ω defines the frequency inside the window of size $[H, W]$ and its direction determines the direction of the sinusoidal pattern. b) Gaussian envelope that determines the scale of the filter. This envelope is rotated ϕ degrees, and its main axes have sizes $\sigma_{x'}$ and $\sigma_{x'}/\lambda$. c) Product of the real part of the complex sinusoid and the Gaussian envelope: Real part of the Gabor filter.

- $x' = x \cos \phi + y \sin \phi$ and $y' = -x \sin \phi + y \cos \phi$ define the rotation of the Gaussian envelope.
- $\sigma_{x'}$ determines the size of the gaussian envelope along its x' direction.
- λ defines the degree of anisotropy of the gaussian envelope.

We design two Gabor filter banks, one for each tagging direction given by ω_k 's, tuned to isolate the I_k 's. We note that, since tissue local deformation is not large, the frequencies of the Gabor filters should be close to the main frequencies. If we write each principal frequency in polar coordinates, $\omega_k = r_k e^{-i\theta_k}$, then nearby frequencies are given by:

$$\omega = (r_k + \Delta r) e^{-i(\theta_k + \Delta\theta)} \quad (3.10)$$

We define the new parameters $\hat{r}_k = r_k + \Delta r$ and $\hat{\theta}_k = \theta_k + \Delta\theta$. Regarding to scale aspects, we consider $\sigma_{x'}$ to be Q times the period of the frequency. With these redefinitions we obtain a Gabor filter bank governed by 5 parameters. We denote a parameter configuration by $\rho = (\hat{r}_k, \hat{\theta}_k \mid \phi, Q, \lambda)$ and the 5 dimensional domain where ρ takes values by \mathcal{P} .

We recall that image sequences come from 2 different standard acquisition views, SA and LA views, which are in turn divided into basal, mid and apical and 2- and 4- chambers respectively (see Fig. 1.5). The heart muscle anatomy [17] strongly influences the motion that the myocardium undergoes in those different views/levels (fig. 1.6). Following the AHA nomenclature for myocardial segments [36] (see Fig. 3.3) the following behavior for the different sequences (seen from apex to base) along the systolic cycle can be observed:

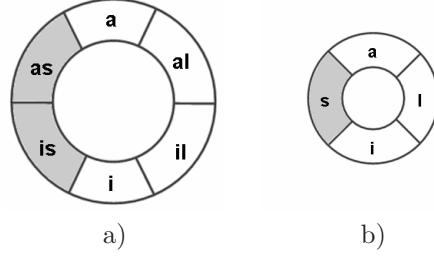


Figure 3.3: American Heart Association nomenclature for myocardial segments in SA views seen from apex to base. a) Basal and mid sectors: anterior (a), anterolateral (al), inferolateral (il), inferior (i) inferoseptal (is) and anteroseptal (as). b) Apical sectors: anterior (a), lateral (l), inferior (i) and septal (s).

- *Base:* All segments less anterior and anterolateral, that undergo radial shortening, rotate counterclockwise at the beginning of the systolic cycle. They rapidly (at 15% of systole approx.) turn to clockwise rotation together to the rest of the segments until the end of the systolic cycle, first row).
- *Mid:* Is the most simple as it mainly presents isotropic radial shortening with few rotation depending on if the acquisition plane approaches to the base or to the apex, second row).
- *Apex:* Presents a counterclockwise rotation together to a contractile component almost homogeneous for all the LV less the inferior sector in which shortening is stronger, third row).
- *Long Axis:* The most basal levels present the highest longitudinal shortening which gradually diminish as they approach to apex, which remains almost still during the whole cardiac cycle. By the other hand LV thicken as they approach to apex, fourth row).

These observations have motivated to design a tailored bank of filters for each of the 4 kinds of sequences. Each filter bank is characterized by its parameter domain that we denote by \mathcal{P}_k^{LA} , \mathcal{P}_k^B , \mathcal{P}_k^M and \mathcal{P}_k^A , with $k = \{1, 2\}$. Parameter values for each domain are specified in table 3.1. Value ranges are given using the notation for vector definition of MATLAB: $(a : h : b)$.

Let I_k , $k = \{1, 2\}$ be the couple of harmonic images associated a tagged image belonging to a certain acquisition plane $l \in \{B, M, A, LA\}$. We obtain them by assigning to each pixel, the maximum response of the bank of filters:

$$I_k(x, y; t) = I(x, y; t) * \Gamma_{\hat{\rho}} \quad \hat{\rho} = \max_{\rho \in \mathcal{P}_k^l} |I(x, y; t) * \Gamma_{\rho}| \quad (3.11)$$

This convolution (filtering) has been implemented in the Fourier space were this operation becomes a simple product as stated by the convolution theorem.

Table 3.1: Parameter ranges of the Gabor filter banks for each type of sequence

	\hat{r}_k	$\hat{\theta}_k$	ϕ	Q	λ
\mathcal{P}_k^B	$(\frac{r_k}{2} : \frac{r_k}{6} : 2r_k)$	$(\frac{\theta_k - \pi}{36} : \frac{\pi}{72} : \frac{\theta_k + \pi}{36})$	$(\frac{-\pi}{18} : \frac{\pi}{18} : \frac{\pi}{18})$	(2, 3)	(1, 2)
\mathcal{P}_k^M	$(\frac{r_k}{2} : \frac{r_k}{6} : \frac{3r_k}{2})$	$(\frac{\theta_k - \pi}{90} : \frac{\pi}{90} : \frac{\theta_k + \pi}{90})$	$(\frac{-\pi}{18} : \frac{\pi}{36} : \frac{\pi}{18})$	(3)	(1)
\mathcal{P}_k^A	$(\frac{r_k}{2} : \frac{r_k}{28} : \frac{3r_k}{2})$	$(\frac{\theta_k - \pi}{18} : \frac{\pi}{126} : \frac{\theta_k + \pi}{18})$	$(\frac{-\pi}{18} : \frac{\pi}{36} : \frac{\pi}{18})$	(3)	(1)
\mathcal{P}_k^{LA}	$(\frac{r_k}{2} : \frac{r_k}{6} : \frac{3r_k}{2})$	$(\frac{\theta_k - \pi}{30} : \frac{\pi}{30} : \frac{\theta_k + \pi}{30})$	$(\frac{-\pi}{18} : \frac{\pi}{36} : \frac{\pi}{18})$	(3)	(1)

The respective phases of I_k , Φ_k , define a bivariate harmonic representation, of the TMR image I . On the other hand, their amplitudes $|I_k|$ indicate the reliability of the local pattern detected by the Gabor filters, in the sense that low values correspond to noise. Amplitudes serve to integrate the two phases in a variational framework which regularizes the deformation field just at areas where the amplitude drops while restoring the underlying motion otherwise.

3.3.2 Variational Approach to LV Motion

The LV motion between two consecutive sequence times, t and $t+1$, is given by the 2D vector field (or deformation map), $V(\mathbf{x}) = (u(\mathbf{x}), v(\mathbf{x}))$ for $\mathbf{x} = (x, y)$, best matching their bivariate harmonic representations. In variational terms, this reduces to finding the minimum of the following energy functional:

$$\varepsilon = \underbrace{\sum_{k=1}^2 \int \|\Phi_k^{t+1}(\mathbf{x}) - \Phi_k^t(\mathbf{x} + V)\|^2}_{\text{Matching}} + \underbrace{\int \|\nabla V\|^2}_{\text{Regularity}} \quad (3.12)$$

for Φ_k^t and Φ_k^{t+1} the harmonic phases of tag images at time t and $t+1$ and the regularity term, $\|\nabla V\|^2 = \|\nabla u\|^2 + \|\nabla v\|^2$, the norm of the gradient of the vector field. In our case, since, in fact, we handle a tracking problem, we substitute the matching term by its optical flow [86] first order approximation. By forcing the optical flow condition, the two summands in the matching term convert into:

$$\begin{cases} \varepsilon_1 \equiv \Phi_{1x}u + \Phi_{1y}v + \Phi_{1t} = \nabla\Phi_1 \cdot V + \Phi_{1t} \\ \varepsilon_2 \equiv \Phi_{2x}u + \Phi_{2y}v + \Phi_{2t} = \nabla\Phi_2 \cdot V + \Phi_{2t} \end{cases} \quad (3.13)$$

for Φ_{kx} , Φ_{ky} , Φ_{kt} , the partial derivatives of the k -th phase at time t . If we note by ε_{reg}^2 the regularity term, then the generic tracking energy becomes:

$$\varepsilon = \int (\varepsilon_1^2 + \varepsilon_2^2) + \int \varepsilon_{reg}^2 \quad (3.14)$$

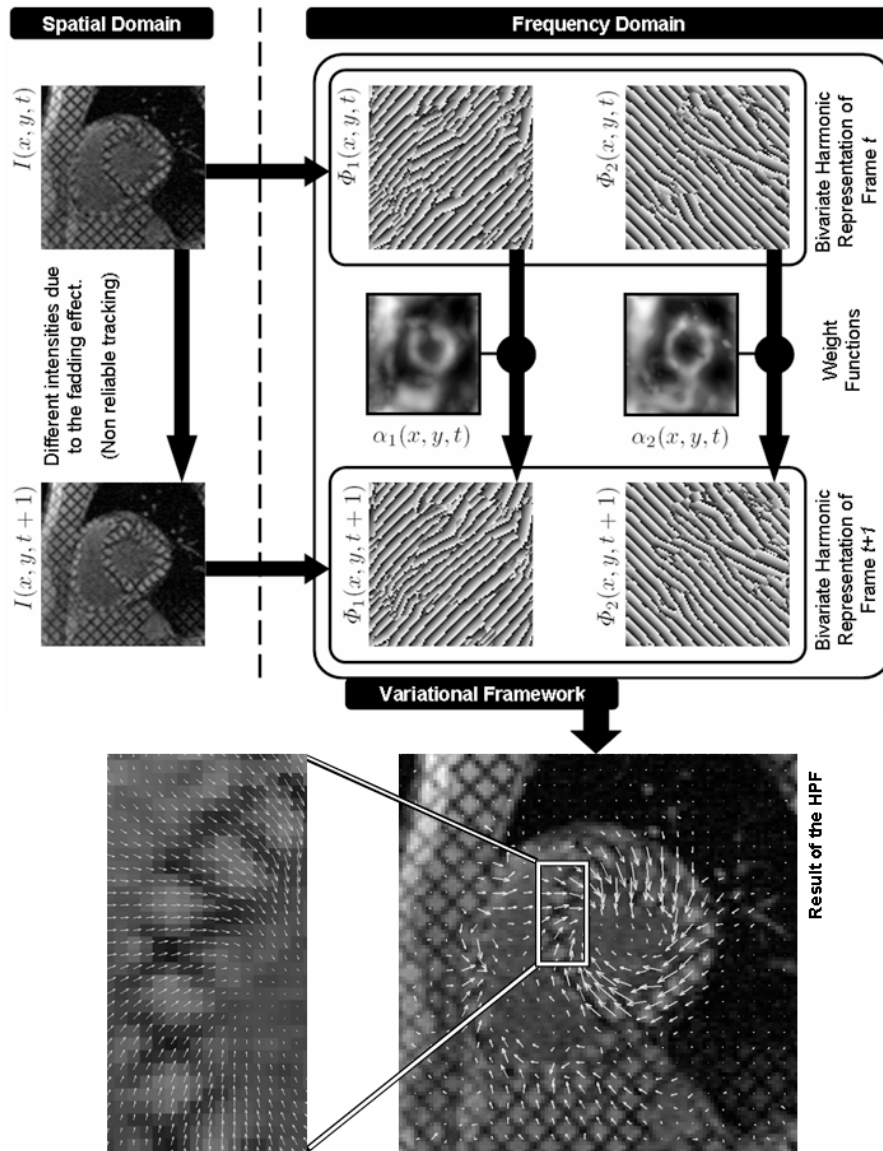


Figure 3.4: Main Steps in the Computation of the Left Ventricle Dynamics. Above on the left, two consecutive frames of a basal sequence. On the right their respective bi-dimensional harmonic representations that, together with the weighting functions (in the center), conform the variational framework for robust tissue tracking. Below on the right we show the result of the HPF, where vectors have been discretized and resized for visualization purposes. On the left detail of the real dense deformation map.

Taking into account that the phase of a complex number is given by the imaginary part of its logarithm, the spatio-temporal derivatives of the phase can be computed without any wrapping effect as:

$$\Phi_{k\ell} = \frac{\left[\operatorname{Re}(I_k) \frac{\partial \operatorname{Im}(I_k)}{\partial \ell} - \operatorname{Im}(I_k) \frac{\partial \operatorname{Re}(I_k)}{\partial \ell} \right]}{|I_k|^2} \quad (3.15)$$

where $\ell = \{x, y, t\}$ and Re , Im stand for the real and imaginary parts of a complex number. Provided that the matching terms ε_k are fully given in terms of phase derivatives, we can use phases Φ_k in the tracking process even without knowing them explicitly. Recall that only their wrapped version a_k was available.

At areas with low signal to noise ratio (e.g. in the presence of thermal noise), the phases Φ_k are not reliable and, thus, should not be taken into account for motion tracking. By adding a weighting function to the energy (3.14) the latter requirement is achieved:

$$\varepsilon = \int (1 - (\alpha_1 + \alpha_2)/2)^2 \varepsilon_{reg}^2 + [\alpha_1^2 \varepsilon_1^2 + \alpha_2^2 \varepsilon_2^2] dx dy \quad (3.16)$$

where α_1 and α_2 depend on the amplitudes of I_k and are normalized in order to take values in the range $[0, 1]$:

$$\alpha_i(x, y) = \frac{|I_i|}{\|I_i\|_\infty} \quad (3.17)$$

for $\|\cdot\|_\infty$ standing for the maximum norm of a bounded function.

Since in the variational framework given by (3.16) the proposed weights depend (at each point) on the amplitude of the filtered images, the smoothness constraint is only applied at areas where the filtering response drops. Low amplitude responses correspond to myocardial areas without noticeable tagging pattern or simply background noise. In both cases, the phase does not provide any information about motion and should not be taken into account. At these areas, the vector field is linearly interpolated using the nearest reliable values. Meanwhile at clearly tagged zones, the smoothing term vanishes and only phase image motion accounts for the computation of HPF. It follows that cardiac motion discontinuities can be retrieved as far as they are detected by the tagging pattern.

We note that the proposed regularity term extends, in some sense, the formulation reported in [147]. Regularity constraints of the type suggested in [147] preserve sharp changes provided that we have an image map measuring the probability of having a meaningful discontinuity. Such map is usually defined in terms of the gradient magnitude of the target function/vector field. In the case of deformation maps in biomedical imaging, a large gradient might possibly be product of a noisy match and, thus, alternate measures are required. Modifying the metric for the L^2 regularity term is the easiest way of obtaining a weighted Laplacian (like in [147]) ensuring

special treatment of singularities in the case that they are not defined in terms of the unknown input. We conclude that the proposed scheme generalizes the ideas reported in [147] without increasing the complexity of the numeric scheme (no hyper-parameter extra minimization is required) and providing a good robustness to noise.

Applying the Euler-Lagrange equations to (3.16), we get:

$$\begin{aligned} [A_{11}u + A_{12}v + A_{13}] &= (1 - \alpha)^2 \Delta u - 2(1 - \alpha)(\alpha_x u_x + \alpha_y u_y) \\ [A_{21}u + A_{22}v + A_{23}] &= (1 - \alpha)^2 \Delta v - 2(1 - \alpha)(\alpha_x v_x + \alpha_y v_y) \end{aligned} \quad (3.18)$$

where $\alpha = \frac{(\alpha_1 + \alpha_2)}{2}$, Δ is the Laplacian operator and the coefficients A_{ij} are equal to:

$$\begin{aligned} A_{11} &= (\alpha_1^2 \Phi_{1x}^2 + \alpha_2^2 \Phi_{2x}^2) \\ A_{12} &= (\alpha_1^2 \Phi_{1x} \Phi_{1y} + \alpha_2^2 \Phi_{2x} \Phi_{2y}) \\ A_{13} &= (\alpha_1^2 \Phi_{1x} \Phi_{1t} + \alpha_2^2 \Phi_{2x} \Phi_{2t}) \\ A_{21} &= A_{12} \\ A_{22} &= (\alpha_1^2 \Phi_{1y}^2 + \alpha_2^2 \Phi_{2y}^2) \\ A_{23} &= (\alpha_1^2 \Phi_{1y} \Phi_{1t} + \alpha_2^2 \Phi_{2y} \Phi_{2t}) \end{aligned}$$

The solution to the system (3.18) is the deformation map that we call *Harmonic Phase Flow*.

Figure 3.4 sketches the main steps involved in the computation of LV motion. Above on the left, we can appreciate two incoming consecutive frames of a tagged sequence for which we want to estimate the deformation among them. On the right, we show their wrapped bi-dimensional harmonic representation which is depicted via stripe-like images. Images shown in the center, that resemble the first frame without tags, are the weight functions and represent the local reliability of the harmonic representation. The phases and the weights are combined using the variational framework defined in (3.16) to obtain the dense harmonic phase flow shown below.

3.3.3 Numerical Issues

The solution to the HPF flow is computed using an iterative finite difference scheme. Let

$$g = \begin{pmatrix} \alpha_1^2 & 0 \\ 0 & \alpha_2^2 \end{pmatrix},$$

$\alpha = \frac{(\alpha_1 + \alpha_2)}{2}$ and $\Phi = (\Phi_1, \Phi_2)$, then the Euler-Lagrange equation (3.18) has the compact writing given by:

$$\begin{aligned} (\Phi_x g \Phi'_x)u + (\Phi_x g \Phi'_y)v + \Phi_x g \Phi'_t &= (1 - \alpha)^2 \Delta u - 2(1 - \alpha) \langle \nabla \alpha, \nabla u \rangle \\ (\Phi_x g \Phi'_y)u + (\Phi_y g \Phi'_y)v + \Phi_y g \Phi'_t &= (1 - \alpha)^2 \Delta v - 2(1 - \alpha) \langle \nabla \alpha, \nabla v \rangle \end{aligned} \quad (3.19)$$

for $\langle \cdot, \cdot \rangle$ denoting the scalar product and $'$ the transpose of a vector. The system (3.19) can be solved by treating u and v as functions of time and solving the gradient descent scheme:

$$\begin{aligned} u_t(x, y, t) &= -[(\Phi_x g \Phi_x)u(x, y, t) + (\Phi_x g \Phi_y)v(x, y, t) + \Phi_x g \Phi_t - \\ &\quad - (1 - \alpha)^2 \Delta u(x, y, t) + 2(1 - \alpha) \langle \nabla \alpha, \nabla u(x, y, t) \rangle] \\ v_t(x, y, t) &= -[(\Phi_x g \Phi_y)u(x, y, t) + (\Phi_y g \Phi_y)v(x, y, t) + \Phi_y g \Phi_t - \\ &\quad - (1 - \alpha)^2 \Delta v(x, y, t) + 2(1 - \alpha) \langle \nabla \alpha, \nabla v(x, y, t) \rangle] \end{aligned} \quad (3.20)$$

The steady-state of the above system of linear parabolic partial differential equations is the solution to the Euler-Lagrange problem (3.18).

The first derivatives of the equation coefficients are computed using centered derivatives. In order to set up the discrete iterative solution, let the indexes i, j and n correspond to the continuous variables x, y and t , respectively, and let the spacing between pixels be h_x and h_y and the time step h_t . Then the partial derivatives can be approximated by finite differences as:

$$\begin{aligned} u_t &= \frac{1}{h_t}(u_{i,j}^{n+1} - u_{i,j}^n) \\ v_t &= \frac{1}{h_t}(v_{i,j}^{n+1} - v_{i,j}^n) \\ u_x &= \frac{1}{2h_x}(u_{i,j+1} - u_{i,j-1}) \quad u_y = \frac{1}{2h_y}(u_{i-1,j} - u_{i+1,j}) \\ v_x &= \frac{1}{2h_x}(v_{i,j+1} - v_{i,j-1}) \quad v_y = \frac{1}{2h_y}(v_{i-1,j} - v_{i+1,j}) \\ \Delta u &= \frac{1}{h_x^2}(u_{i,j+1} - 2u_{i,j} + u_{i,j-1}) + \frac{1}{h_y^2}(u_{i+1,j} - 2u_{i,j} + u_{i-1,j}) \\ \Delta v &= \frac{1}{h_x^2}(v_{i,j+1} - 2v_{i,j} + v_{i,j-1}) + \frac{1}{h_y^2}(v_{i+1,j} - 2v_{i,j} + v_{i-1,j}) \end{aligned}$$

Substituting these expressions into (3.20) and assuming equal spacing for pixels, namely h , we get our iterative approach to HPF computation:

$$\begin{aligned}
u_{i,j}^{n+1} &= u^n + r(u_{i+1,j}^n + u_{i,j+1}^n + u_{i-1,j}^n + u_{i,j-1}^n - 4u_{i,j}^n) - \\
&\quad - \frac{(1-\alpha)h_t\alpha_x}{h}(u_{i,j+1}^n - u_{i,j-1}^n) - \frac{(1-\alpha)h_t\alpha_y}{h}(u_{i-1,j}^n - u_{i+1,j}^n) - \\
&\quad - (a_{11}h_tu^n + a_{12}h_tv^n + b_1h_t) \\
v_{i,j}^{n+1} &= v^n + r(v_{i+1,j}^n + v_{i,j+1}^n + v_{i-1,j}^n + v_{i,j-1}^n - 4v_{i,j}^n) - \\
&\quad - \frac{h_t(1-\alpha)\alpha_x}{h}(v_{i,j+1}^n - v_{i,j-1}^n) - \frac{h_t(1-\alpha)\alpha_y}{h}(v_{i-1,j}^n - v_{i+1,j}^n) - \\
&\quad - (a_{22}h_tv^n + a_{21}h_tu^n + b_2h_t)
\end{aligned} \tag{3.21}$$

for $a_{11} = (\Phi_x g \Phi_x)$, $a_{12} = a_{21} = (\Phi_x g \Phi_y)$, $a_{22} = (\Phi_y g \Phi_y)$, $b_1 = \Phi_x g \Phi_t$ and $b_2 = \Phi_y g \Phi_t$. The r coefficient is defined as the ratio:

$$r = \frac{(1-\alpha)^2 h_t}{h^2} \tag{3.22}$$

and determines the convergence of the iterative scheme [6, 209]. According to standard arguments of theory of numerical methods, since all coefficients are bounded, the scheme (3.21) converges as far as $r \leq 1/4$. Assuming unitary pixel spacing we have that:

$$r \leq \frac{h_t \max((1-\alpha)^2)}{h^2} \leq h_t \max((1-\alpha)^2) \tag{3.23}$$

Therefore the convergence condition is guaranteed provided that the time step satisfies:

$$h_t \leq \frac{1}{4 \max((1-\alpha)^2)} \tag{3.24}$$

We recall that α measures the response to the Gabor filter. Therefore the scheme speed increases in the rate that the tagging pattern is well defined.

Figure 3.5 shows the final result of HPF after convergence, in a basal systolic TMR sequence composed of 6 frames. Since motion is estimated among consecutive frames, we show vector fields just in the first 5 frames. Two main observation can be done. On one hand HPF just detects motion in moving structures and not in the still background (see first column of figure 3.5). On the other hand, the motion field provided by HPF is smooth (see third column of figure 3.5).

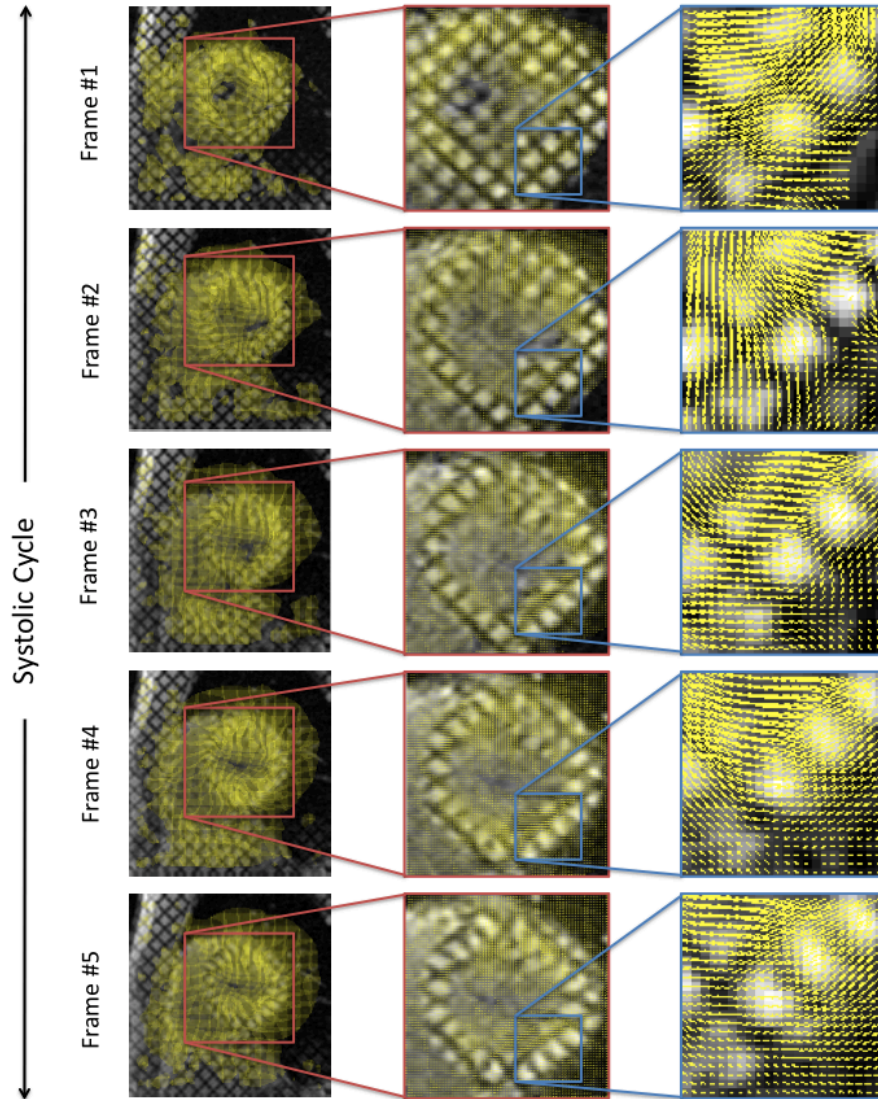


Figure 3.5: In the first column, motion vector field estimated by HPF in a sequence of 6 TMR frames (motion detected among consecutive frames, 5) belonging to a basal slice. In the second and third columns, successive zooms of the original frame.

3.4 Experiments

3.4.1 Synthetic Data

In order to assess the performance of the proposed HPF, we have created a 3D dynamic model (Fig. 3.6 (a)). The geometry of the 3D model at initial time (end-diastole) is

obtained by considering 2 prolate spheroids that intersect at the apical cap. Points between these two surfaces are tissue points called, at initial time, material points. Material points have been tagged using the SPAMM tagging equations given in [206]. They have been evolved according to the principal motions that the LV undergoes along the systolic cycle:

- *Torsion*: which is the angular difference between the most basal and most apical parts of the LV.
- *Radial Shortening*: that makes the tissue to collapse towards the long axis of the LV.
- *Longitudinal Shortening*: which causes the base to contract towards the apex which, on the other hand, remains almost still.

The parameter ranges for these principal motions (obtained empirically) are sketched in Table 3.2. They vary from 0° to 12° for torsion, from 0% to 18% for radial shortening and from 0% to 12% for longitudinal shortening. The model used in the present paper is composed of 7 frames corresponding to a uniform sampling of the parametric ranges. The discretization (7 frames/systolic cycle) has been chosen to produce the mean number of frames per systolic cycle we have in our experimental data. Two different 2D motion phantoms have been considered. A first phantom (phantom #1 shown in Fig.3.6 (a)) is obtained by intersecting the model with planes representing the four acquisition cuts (base, middle, apex and LA). Since there is no motion information missing, phantom #1 provides the base line for any systematic errors in HPF. In order to assess HPF ability for restoring missing information and preserving discontinuities at myocardial borders, a second phantom (phantom #2, shown in Fig. 3.6 (b)) has been generated from phantom #1. Phantom #2 undergoes constant rotation and includes surrounding still tissue, that induce discontinuities in the tagging pattern. It also includes noisy areas where the tagging pattern is not well defined or, even, missed. Thus, this phantom allows to test the HPF performance in more severe conditions.

Table 3.2: Motion parameters of the 3D phantom for each frame of the systolic cycle.

	t_0	t_1	t_2	t_3	t_4	t_5	t_6
<i>Torsion</i>	0°	2°	4°	6°	8°	10°	12°
<i>Rad.Comp.</i>	0%	3%	6%	9%	12%	15%	18%
<i>Long.Comp.</i>	0%	2%	4%	6%	8%	10%	12%

HPF Accuracy on Synthetic Data

The Euclidean norm of the difference between the ground truth deformation used to generate our dynamic phantom and the HPF flow is a measure of accuracy for each

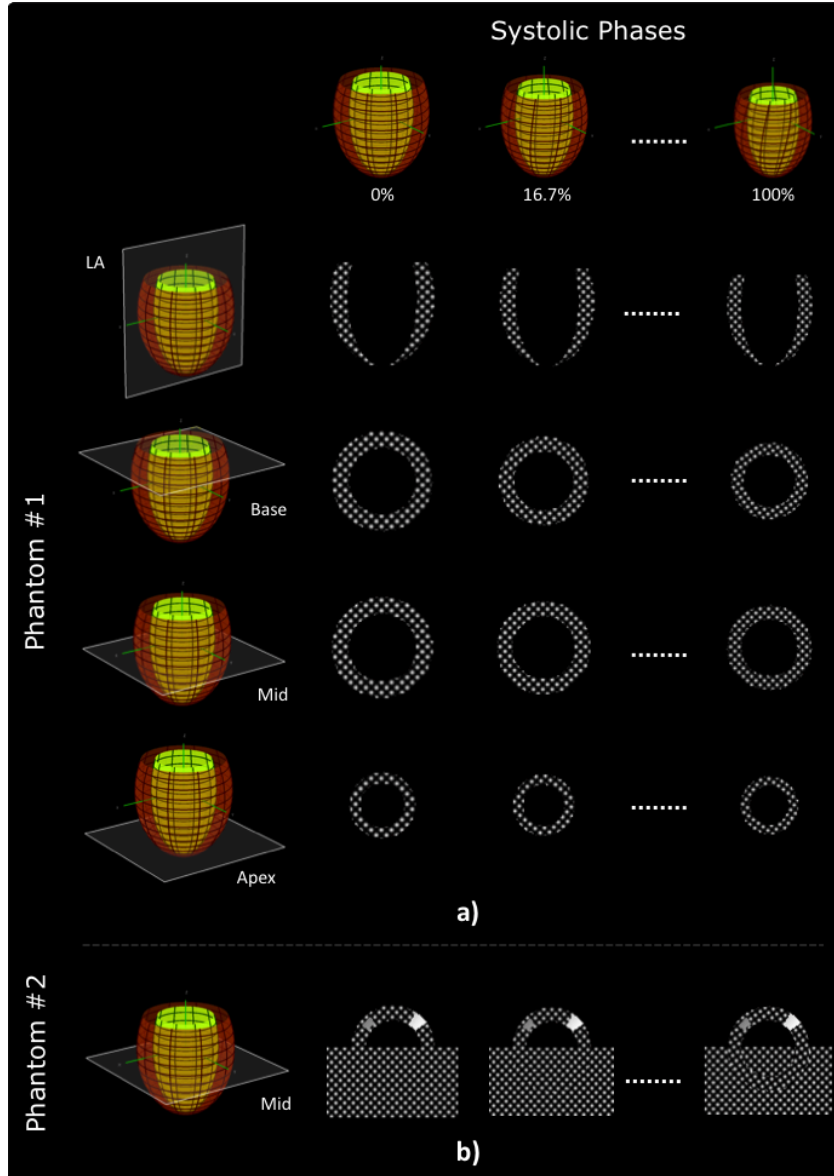


Figure 3.6: Phantoms. a) 3D dynamic myocardial model intersected by 4 representative acquisition planes. b) Basal sequence frames for phantom #2 simulating motionless background and 2 gaps without tagging pattern.

image pixel. The mean and standard deviation for all image pixels, provide the error range for a given frame (i.e. time). We denote by μ_l^t and σ_l^t the mean and standard deviation respectively for a given time, t , and an acquisition plane, $l \in \{B, M, A, LA\}$.

The character B stands for basal cuts, M stands for mid cuts, A stands for apical cuts and LA stands for long axis cuts. The values obtained for the 7 frames of the phantom are interpolated (cubically) to the whole systolic cycle in order to provide a continuous error measure of the sequence.

Figure 3.7 shows the error values (in pixels) along the systolic cycle for each of the levels / views for phantom #1 (Fig. 3.7 (a)-(d)), and for base and apex for phantom #2 (fig. 3.7 e) and f)). The dark bold line represents μ_t^t , while vertical gray lines represent σ_t^t . The errors (vertical axis) are given in pixels. Both phantoms present a similar error tendency with mean error curves (below 0.3 pixels) almost constant along the systolic cycle. In order to localize any increase in errors, their spatial distribution has been explored. Error maps along systole for the basal sequence of phantom #2 are shown in figure 3.8 a). Two interesting conclusions are extracted from the analysis of these error maps:

- In general there is not any significant increase in error at myocardial boundary points with the exception of frame 4, which presents an error of 1 pixel at the lower part of the boundary. For this frame there is a sharp discrepancy between myocardial and external tagging patterns. Since the amplitude of the Gabor response depends on the strength of the main tagging pattern, at those points it has a significant decrease in α_i 's values (as shown in Fig.3.8 (b)). Such decrease in the weights introduces a fake activation of the regularizing term which increases HPF error. A new measure of Gabor phase consistency is currently under development.
- The vector field extension provided by HPF successfully restores deformation maps at gaps provided that their inner motion conforms to the motion available at their boundaries. It follows that HPF achieves a high accuracy for the empty region at the left upper part of phantom #2. Meanwhile, in the case of the region located at the right upper part of phantom #2 the error increases due to insufficient information at its boundary.

The quality of the deformation field restored by HPF is illustrated in fig. 3.9.

3.4.2 Real Data

Our data set is composed of a total number of 21 volunteers, 15 males and 6 females aged between 23 and 55 (30.7 ± 7.5). For each subject, several (ranging from 6 to 8) short axis tagging sequences covering the LV from base to apex were acquired. Also 4 equidistributed long axis planes (including 2 and 4 chambers) were obtained. In order to avoid misalignments due to breathing, sequences were recorded in breath-hold. For the acquisition of the tagged sequences, a Siemens Avanto 1.5 T (Erlangen, Germany) equipment was used. Images have an in-plane spatial resolution ranging from $1.56 \times 1.56 \text{ mm}^2/\text{pixel}$ to $1.97 \times 1.97 \text{ mm}^2/\text{pixel}$ and a thickness of 6 mm. per cut. The flip angle is 14, the repetition time is 46 ms. and the echo time is 3.8 ms.

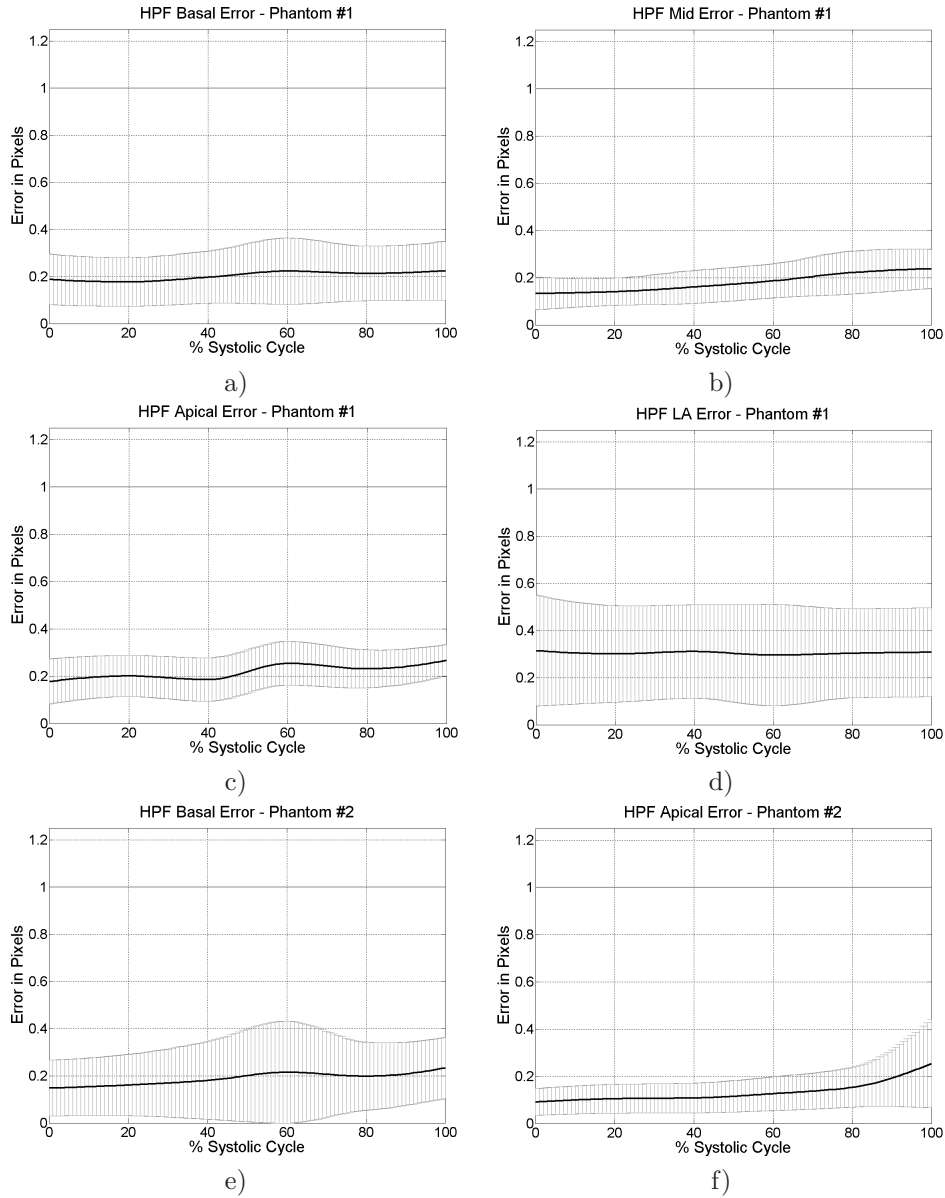


Figure 3.7: HPF accuracy for the 2 dynamic phantoms. In dark bold line, the mean error between the real deformation map and the estimated one along the whole systolic cycle. Vertical gray lines represent the standard deviation. Phantom #1: a) base, b) mid, c) apex and d) long axis. Phantom #2: e) base, f) apex.

Our sequences have approximately 7 frames (of mean size 89×94 pixels) per systolic cycle.

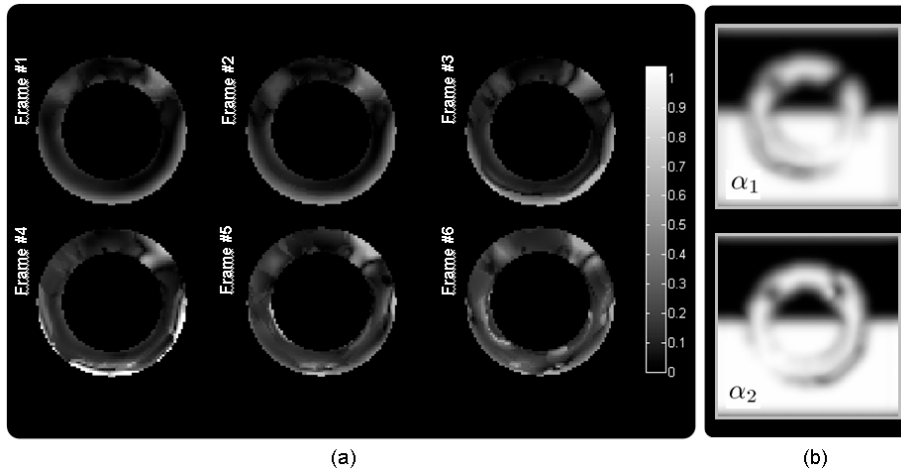


Figure 3.8: HPF Error distribution analysis for phantom #2.: Error maps along systolic cycle in a), and image weights (α_1, α_2) of the regularization term for frame 4 in b).

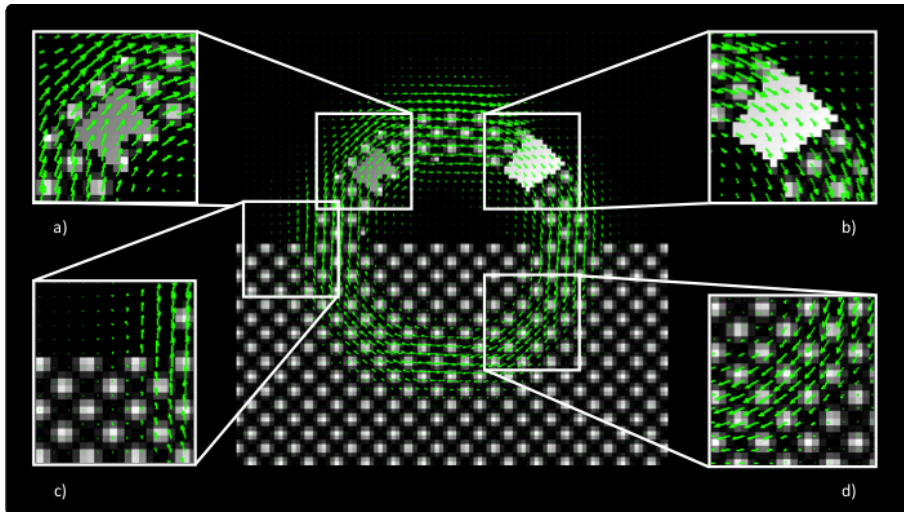


Figure 3.9: Details for a frame of the phantom #2 after applying HPF. In a) and b) gaps (noise) have been filled with the surrounding values, due to action of the regularizing term of the variational framework. In c) we can appreciate that in still tissue and air HPF detects no motion. In d) we can observe motion detected over the left ventricular tissue.

TMR sequences used in this thesis have been provided by Xavier Alomar from the Department of Radiology at Clínica la Creu Blanca.

In a standard PC(Intel® Pentium® D CPU 3.00GHz.) processing sequences using MATLAB takes about 2.6 min. for basal sequences, 0.8 min. for mid sequences, 3.1 min. for apical sequences and 2.8 min. for LA sequences. The former processing times for the computation of HPF include the two main steps: tuning of the Gabor filter banks for each view and iterative solving of equation (3.20). In all cases, equation (3.20) converges in about 125 iterations independently of the considered sequence view. The difference in times is essentially due to the filtering process. The number of filters to apply depends on the complexity of the motion observed. In this sense, since mid sequences present the simplest behavior they have a smaller bank of filters.

HPF Accuracy on Real Data

For assessing experimental accuracy, we have analyzed 7 cases randomly selected. For each sequence, we have automatically (and randomly) selected $N(= 25)$ points uniformly spread inside the LV at the initial frame. An expert was asked to manually track these points along the systolic cycle, which provided us with an "expert-dependent" sparse ground truth. For each sequence, its error has been computed as in the previous section. Precision results for each type of sequence (Basal, Mid, Apical and LA) are given by the mean and standard deviation computed over the 7 cases.

Results can be seen separately for each type of sequence in figure 3.10, where the mean is depicted in dark bold line and the standard deviation is represented in vertical gray lines. As in the previous section, error ranges are given in pixels. Although the error is higher than in synthetic sequences, the mean error is close to pixel accuracy. In fact, it keeps within subpixel accuracy with the exception of the basal cut between 50% and 80% of the systolic cycle. We attribute this fact to the presence of large zones with noise over the myocardium. It follows that the reliable information provided by the HARP images is so sparse that HPF restores a flow that is prone to differ from the true motion.

In figure 3.11 we show the HPF-based tracking of the myocardial tissue in 3 stages covering the systolic cycle. Contours have been segmented manually at the initial frame and automatically evolved in further stages.

3.5 Discussion

HPF accuracy has been tested in, both, synthetic and experimental data. We have generated 2 synthetic models. The first one (phantom #1) considers the main basic cardiac motions and serves to set HPF base-line error. The second one introduces background still tissue and gaps in tag pattern. In this way we have explored HPF capabilities for preserving discontinuities at myocardial borders as well as information filling. In all cases, HPF achieved subpixel accuracy (0.3 pixels average) along the whole cycle which shows that there are not any systematic errors. The analysis of error distribution for phantom #2 prompts 2 interesting properties. Firstly, HPF properly retrieves motion information in the presence of gaps in the tagging pattern.

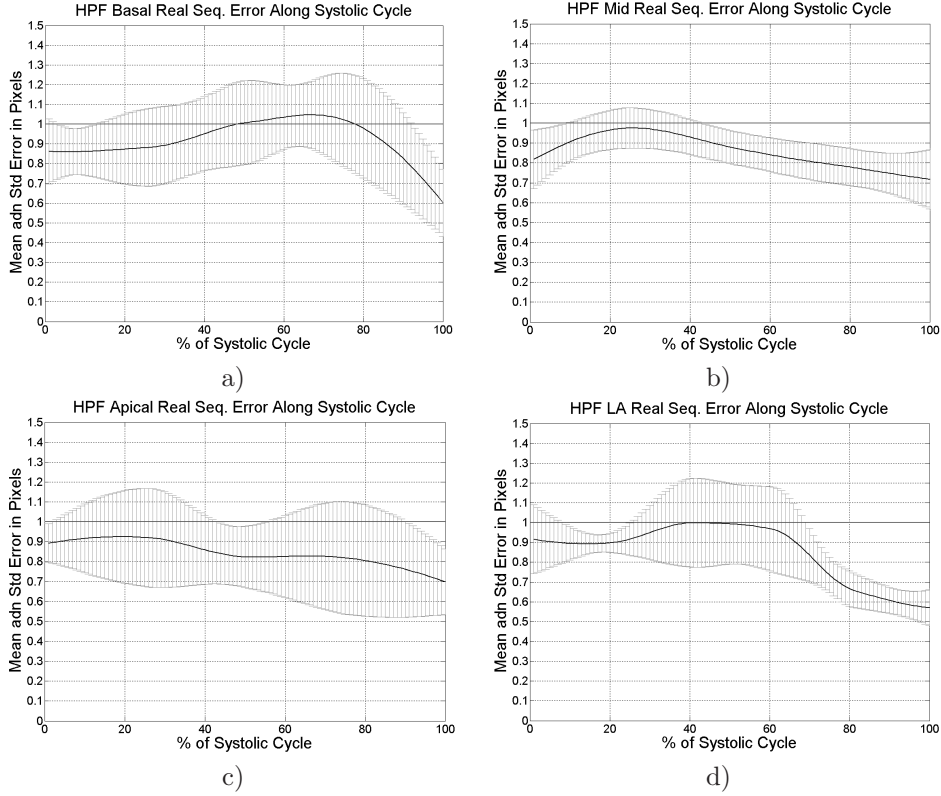


Figure 3.10: HPF accuracy for experimental data. In dark bold line, the mean error between the real deformation map and the estimated one, along the whole systolic cycle. Vertical gray lines represent the standard deviation for a) base, b) mid, c) apex and d) long axis.

Secondly, HPF preserves motion discontinuities as far as tags do not present a sharp corner-like pattern. This might produce a decrease in HPF accuracy at some parts of the myocardial borders. This is common to all existing methods and, in our case, might be solved by modifying the weighting functions.

For experimental data we used a set of 7 sequences for each level and view. Myocardial points were manually tracked by an expert in order to provide the ground truth deformation to be compared to the HPF estimation of motion. We note that, in this way, statistics do not take into account inter-observer variability. With the exception of a short interval in the basal sequences where it reaches 1.2 pixels, in all cases the mean error, although higher than in synthetic data, achieved subpixel accuracy. The increase in error in real sequences is due to thermal noise which corrupts the HARP images. Constancy in error along the systolic cycle proves the method robustness to the fading effect.

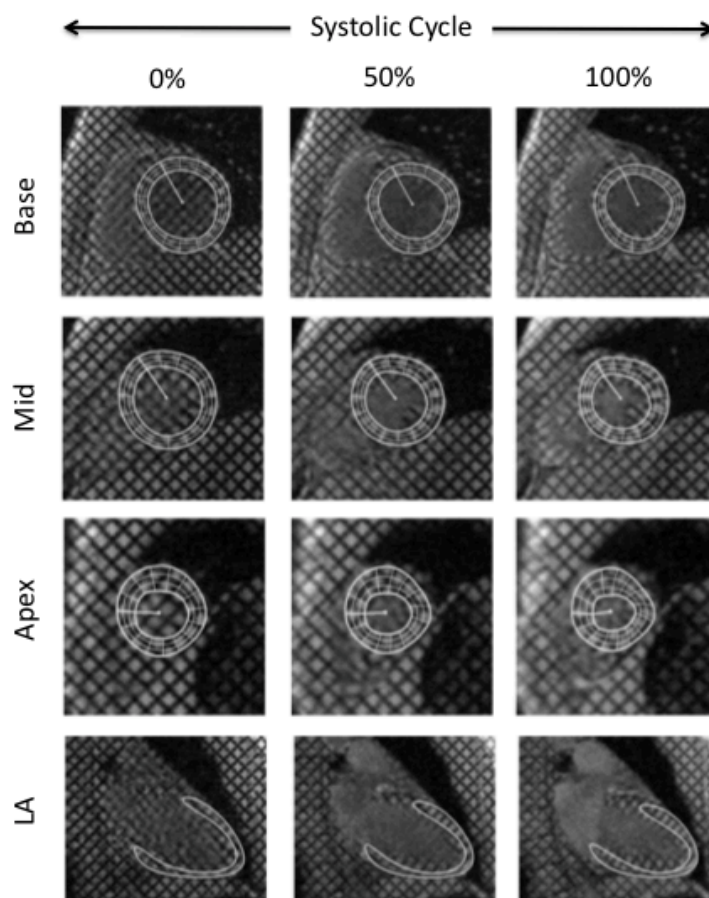


Figure 3.11: HPF-based contour tracking. The initial contours (first column) of basal, mid, apical and LA instances, have been tracked using HPF, and results are shown at 50% (second row) and 100% of the systolic cycle.

Chapter 4

Normalized Parametric Domain

In this Chapter, we introduce a unified comparison framework that jointly addresses the definition of time-evolving coordinate systems tailored for the geometry of each LV in different subjects (unfolding of the LV) and the implicit registration of LV geometries of different subjects at different times. This framework is called Normalized Parametric Domain (NPD) and it is based on the parametrization of manifolds in the context of Differential Geometry.

We apply the NPD framework to the LV. Since the ultimate goal is modelling the LV anatomy (including fibers) and function, the NPD is computed for the LV in TMR sequences acquired at SA views and the whole LV in DTI volumes.

4.1 Background on Manifolds

Mathematics involved in the definition and handling of manifolds may be found in [135]. In this section we just provide intuitive interpretations of concepts supporting the definition of the NPD framework.

Manifolds

A property that characterizes any manifold (\mathcal{M}) is that, seen on a small enough scale, it resembles the Euclidean space \mathbb{R}^n of a given dimension n , which is called the manifold dimension. By Nash's theorem [138], manifolds can always be embedded (immersed) into a bigger m -dimensional Euclidean space, which is called the ambient space of the manifold.

Intuitively, a manifold can be considered as the result of doing patchwork. That is, \mathcal{M} can be made by "cutting" pieces of \mathbb{R}^n , "deforming" them and smoothly "gluing" them together one by one in order to achieve the desired shape. In mathematical terms, for any point $\mathbf{x} \in \mathcal{M}$, there exists an open neighborhood \mathcal{U} of \mathbf{x} homeomorphic

to an open set \mathcal{V} of \mathbb{R}^n . This means that there exists a mapping $\Phi : \mathcal{U} \rightarrow \mathcal{V}$ that is continuous with inverse well defined and also continuous (fig. 4.1). In the case that the manifold has boundary (e.g. cylinder), neighbors of the boundary are homeomorphic to closed sets of \mathbb{R}^n , which boundary maps to the manifold boundary.

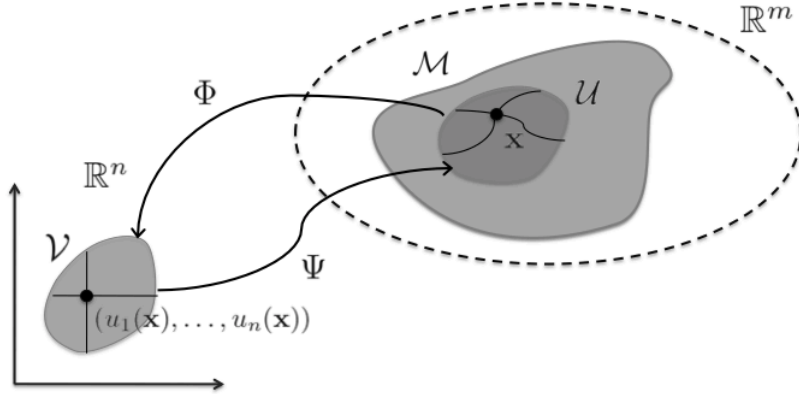


Figure 4.1: n -dimensional manifold embedded into \mathbb{R}^m . The local chart (\mathcal{U}, Φ) defines local coordinates and coordinate directions inside a neighborhood of \mathcal{M} . The inverse mapping, Ψ , defines the parametrization of a portion of \mathcal{M} .

Parametrization of Manifolds

The way to move over manifolds and locate specific points is by means of coordinate charts. Since manifolds are locally equivalent (homeomorphic) to \mathbb{R}^n , any point $\mathbf{x} \in \mathcal{U}$ can be identified to a point in \mathbb{R}^n via Φ :

$$\Phi(\mathbf{x}) = (u_1(\mathbf{x}), \dots, u_n(\mathbf{x})) \quad (4.1)$$

This n -tuple is called the *local coordinates* of \mathbf{x} and \mathcal{U} is called a *coordinate neighborhood*. Thus, every point that is sufficiently close to \mathbf{x} can be uniquely described by n independent parameters called *local coordinates*. The curves provided by the u_i 's over the manifold are called *coordinate directions* or *coordinate curves*. The pair (\mathcal{U}, Φ) is called *local chart* or *local coordinate system*, $\mathcal{V} = \Phi(\mathcal{U})$ is called parametric domain and $\Psi = \Phi^{-1}$ parametrization. In Figure 4.1 we can appreciate an n -dimensional manifold embedded into the ambient space \mathbb{R}^m sketching all these concepts.

Atlases of Local Charts

In general, only one open neighborhood \mathcal{U} (equivalently, one parametric domain \mathcal{V}) is not enough to cover (parameterize) all the manifold and, thus, more than one local chart is required. A family of local charts $\{(\mathcal{U}_\alpha, \Phi_\alpha)\}_{\alpha \in A}$ such that $\cup_{\alpha \in A} \mathcal{U}_\alpha$ covers

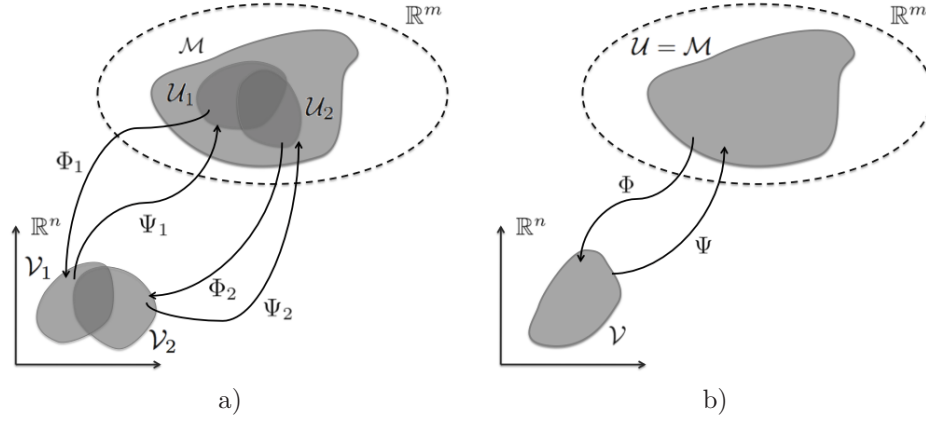


Figure 4.2: Atlas of local charts. a) Two local charts covering a piece of the manifold \mathcal{M} . b) A Single Charted Manifold. The deformed piece of \mathbb{R}^n , \mathcal{U} , covers the whole \mathcal{M} .

the whole \mathcal{M} is said to be an *atlas* of \mathcal{M} and intuitively can be interpreted as doing patchwork (Fig. 4.2 (a)). The map $\Phi_2 \circ \Psi_1 : \mathcal{V}_1 \cap \mathcal{V}_2 \rightarrow \mathcal{V}_1 \cap \mathcal{V}_2$ is called coordinate change. The condition of differentiable manifold requires that $\Phi_2 \circ \Psi_1$ is differentiable. That is, the gluing is smooth.

In the particular case that the manifold can be covered with a single chart (Fig. 4.2 (b)), no coordinate changes are required for the description of the manifold. In such case, the parametrization of the manifold can be regarded as an unfolding process. Figure 4.3 illustrates such unfolding process in the case of LV in 2D SA views (Fig. 4.3 (a)) and for the whole LV volume in 3D (Fig. 4.3 (b)).

Tangent Space of a Manifold

The set of local charts endows the manifold with a topology (i.e., neighbors). The geometry arises with the definition of directions (e.g., left-right, up-down) in each open neighborhood. Directions in differentiable manifolds are given at each point \mathbf{x} by its tangent space, which we will note by $T_{\mathbf{x}}\mathcal{M}$. The elements of the tangent space are called tangent vectors at \mathbf{x} and, intuitively, they describe all possible "directions" through \mathbf{x} .

Tangent vectors are defined by means of parameterizations as follows. If (\mathcal{V}, Ψ) is a parametrization $\Psi : \mathcal{V} \subset \mathbb{R}^n \rightarrow \mathcal{U} \subset \mathbb{R}^m$ given by $\Psi(\mathbf{u}) = (\Psi_1(\mathbf{u}), \dots, \Psi_m(\mathbf{u}))$, then the differential of Ψ , $D\Psi$, defines a linear map given by the Jacobian matrix:

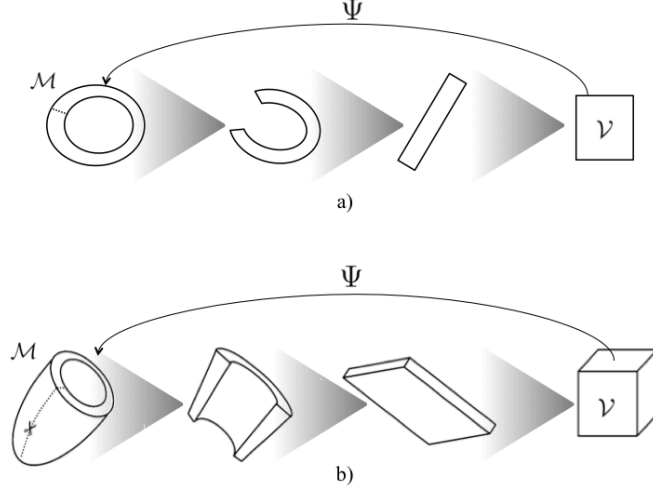


Figure 4.3: Unfolding process of the LV in the 2D case a), and in the 3D case b). Notice that such unfoldings provide a parametrization, Ψ , between a rectangular domain and the LV.

$$\begin{aligned}
 D\Psi(\mathbf{u}) &= (\nabla_{u_1} \Psi(\mathbf{u}), \nabla_{u_2} \Psi(\mathbf{u}), \dots, \nabla_{u_n} \Psi(\mathbf{u})) = \\
 &= \begin{pmatrix} \frac{\partial \Psi_1}{\partial u_1}(\mathbf{u}) & \frac{\partial \Psi_1}{\partial u_2}(\mathbf{u}) & \dots & \frac{\partial \Psi_1}{\partial u_n}(\mathbf{u}) \\ \frac{\partial \Psi_2}{\partial u_1}(\mathbf{u}) & \frac{\partial \Psi_2}{\partial u_2}(\mathbf{u}) & \dots & \frac{\partial \Psi_2}{\partial u_n}(\mathbf{u}) \\ \vdots & \vdots & \ddots & \vdots \\ \frac{\partial \Psi_m}{\partial u_1}(\mathbf{u}) & \frac{\partial \Psi_m}{\partial u_2}(\mathbf{u}) & \dots & \frac{\partial \Psi_m}{\partial u_n}(\mathbf{u}) \end{pmatrix}
 \end{aligned} \tag{4.2}$$

The Jacobian matrix maps vectors from \mathbb{R}^n to the tangent space at $\mathbf{x} = \Psi(\mathbf{u})$. The columns of $D\Psi$ (which correspond to applying the map to the canonical basis of \mathbb{R}^n , $\{\epsilon_1, \dots, \epsilon_n\}$) constitute a basis of the tangent space. The associated unitary vectors

$$e_1(\mathbf{u}) = \frac{\nabla_{u_1} \Psi(\mathbf{u})}{\|\nabla_{u_1} \Psi(\mathbf{u})\|_2}, \dots, e_n(\mathbf{u}) = \frac{\nabla_{u_n} \Psi(\mathbf{u})}{\|\nabla_{u_n} \Psi(\mathbf{u})\|_2} \tag{4.3}$$

also span the tangent space and will constitute our local basis on the manifold (see Fig. 4.4).

Notice that in the case that the manifold has equal dimension than the ambient space ($n = m$), the matrix in equation (4.2) becomes squared and defines an isomorphism in \mathbb{R}^m that can be regarded as a local change of coordinates.

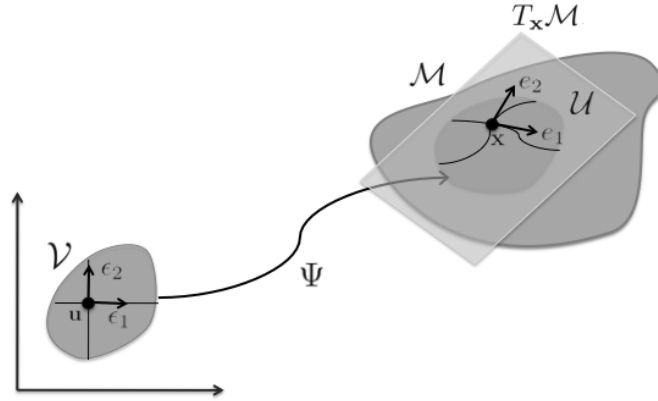


Figure 4.4: Tangent Space.

4.1.1 Mapping Data to the Parametric Domain

Scalar quantities are defined on \mathcal{M} by any real valued function $f : \mathcal{M} \rightarrow \mathbb{R}$. It follows that they can be directly mapped to the parametric domain by considering the composition

$$(f \circ \Psi) : \begin{array}{l} \mathcal{V} \longrightarrow \mathcal{M} \longrightarrow \mathbb{R} \\ \mathbf{u} \longmapsto \Psi(\mathbf{u}) \longmapsto (f \circ \Psi)(\mathbf{u}) \end{array} \quad (4.4)$$

In the case of vector fields, they are defined over \mathcal{M} by multi-valued real functions $V : \mathcal{M} \rightarrow \mathbb{R}^n$ and they are mapped to the parametric domain by applying the inverse of the Jacobian matrix, $D\Psi^{-1}$. The inverse $D\Psi^{-1}$ is also a linear map and, by definition, it maps the basis $\{e_i\}_i$ onto

$$\frac{\epsilon_1}{\|\nabla_{u_1} \Psi(\mathbf{u})\|_2}, \dots, \frac{\epsilon_n}{\|\nabla_{u_n} \Psi(\mathbf{u})\|_2} \quad (4.5)$$

which is a resized version of the canonical basis of \mathbb{R}^n , $\{\epsilon_i\}_i$. It follows that the mapping of V onto the parametric domain is given by its components in the basis $\{\epsilon_i\}_i$ up to a scale factor:

$$D\Psi^{-1}(V) = D\Psi^{-1} \left(\sum_i V_i e_i \right) = \sum_i (V_i D\Psi^{-1}(e_i)) = \sum_i \frac{V_i}{\|\nabla_{u_i} \Psi\|_2} \epsilon_i \quad (4.6)$$

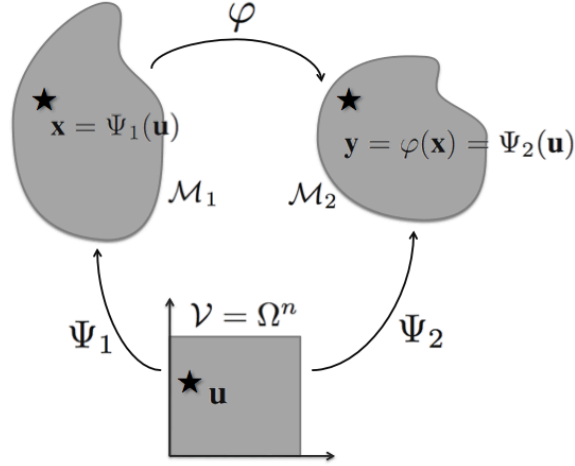


Figure 4.5: Implicit parametrization scheme. The parametrization functions Ψ_1 and Ψ_2 put in correspondence \mathcal{M}_1 and \mathcal{M}_2 with \mathcal{V} . Since same anatomical positions in both objects (marked with \star) are assigned the same parameter \mathbf{u} , both objects are implicitly registered in \mathcal{V} .

That is, in order to move vectorial quantities from \mathcal{M} to \mathcal{V} , it suffices to consider their components in terms of the coordinate systems of the tangent space, and dividing it by the correspondent factor.

4.2 Normalized Parametric Domain Framework

Most anatomical structures are homeomorphic to closed shapes (such as cylinders in the case of bones, spheroids in the case of liver or semi-spheroids in the case of the LV). Since by definition, atlases are given by open coverings, all of them would require more than one chart to be completely parameterized. However, since periodicity constrains may be imposed in, at least, one direction, in practice, a single local chart parameterizes the whole object. In fact, all shapes that represent a given anatomical structure (the LV of all possible subjects at all possible cardiac phases, for instance) admit a common parametric domain, which identifies to the unitary cube $\Omega^n = [0, 1] \times \dots \times [0, 1]$. We call Ω^n Normalized Parametric Domain.

Let Θ^n be the set of all n-dimensional manifolds that represent a given anatomical structure (the LV of all possible subjects at all possible cardiac phases, for instance). Given $\mathcal{M}_1, \mathcal{M}_2 \in \Theta^n$, since they are diffeomorphic (i.e., one is a deformation of the other) there exists a smooth mapping $\varphi : \mathcal{M}_1 \rightarrow \mathcal{M}_2$ with a smooth inverse. The diffeomorphism φ ensures that there exists a couple of parameterizations Ψ_1 and Ψ_2 sharing the same parametric domain. This follows from the fact that, given one (of the infinite) parameterizations of \mathcal{M}_1 , $\Psi_1 : \Omega^n \rightarrow \mathcal{M}_1$, then $\Psi_2 = \varphi \circ \Psi_1 : \Omega^n \rightarrow \mathcal{M}_2$ is

a parametrization of \mathcal{M}_2 using the same parametric domain. An interesting property is that such parameterizations assign equal parameters to equivalent locations (see Figure 4.5), this is, $\varphi(\Psi_1(\mathbf{u})) = \Psi_2(\mathbf{u}), \forall \mathbf{u} \in \Omega^n$. In this case, the manifolds \mathcal{M}_1 and \mathcal{M}_2 are implicitly registered to Ω^n via Ψ_1 and Ψ_2 .

Notice that for any couple of manifolds \mathcal{M}_i and \mathcal{M}_j implicitly registered in the parametric domain, either scalar or vectorial quantities obtained on them, may be mapped to Ω^n (Subsec. 4.1.1). This allows point-wise comparisons of data, which is the basis for any further robust statistical analysis.

Definition 4.2.1 *The Normalized Parametric Domain Framework of Θ^n , is defined as the set of parameterizations $\Psi_i : \Omega^n \rightarrow \mathcal{M}_i$ for all $\mathcal{M}_i \in \Theta^n$, fulfilling the following properties:*

1. All \mathcal{M}_i 's are implicitly registered in Ω^n .
2. The parametric directions over \mathcal{M}_i (given by Ψ_i) have an anatomic meaning.

Anatomical structures present several landmarks (curvature extremals, junctions, etc.) common to any subject and easily identifiable. The key for the definition of the NPD framework consists of assigning to these landmarks a normalized (between 0 and 1) parameter codifying their position relatively to the geometry of the organ. In particular, boundaries are assigned values of 0 or 1.

Considering pairs composed of points \mathbf{x}_i in the object, and their assigned parameters \mathbf{u}_i , the parametrization function Ψ may be built using n -dimensional B-Splines:

$$\Psi(u_1, \dots, u_n) = \sum_{i_1=1}^{M_1} \sum_{i_2=1}^{M_2} \dots \sum_{i_n=1}^{M_n} B_{i_1}(u_1) B_{i_2}(u_2) \dots B_{i_n}(u_n) P_{i_1, i_2, \dots, i_n} \quad (4.7)$$

The B_i 's are blending functions with associated knot vectors such that Ψ is defined in Ω^n . The orders of B_i polynomials determine the order of the objects along each direction and may vary according to the nature of the object that is being parameterized. The $P_{i_1, i_2, \dots, i_n} \in \mathbb{R}^n$ are $M_1 \times M_2 \times \dots \times M_n$ control points which are estimated minimizing (in the least squares sense) the following functional:

$$\sum_{i=1}^N \|\Psi(\mathbf{u}_i) - \mathbf{x}_i\|^2 \quad (4.8)$$

4.2.1 NPD Framework Properties

The NPD framework provides, both, an implicit registration to a unitary squared template and a subject-specific coordinate system adapted to the geometry of the anatomical structure. Thus, the NPD framework enjoys several advantages over existing explicit registration approaches:

- *Generic comparison framework.* The NPD framework provides a comparison domain (Ω^n) well suited for comparing and fusing different local scores of different natures (scalar, vectorial).
- *Generic abstract template.* Since the anatomies of all subjects are registered to a common domain, Ω^n , the NPD framework overcomes the problem (in registration approaches) of choosing a reference anatomy [27]. In fact, Ω^n might be considered as an abstract version of the natural coordinates proposed in [27]. Moreover, unlike the computation of natural coordinates which depends on the number of considered anatomical structures, the NPD framework is independent since it is fixed beforehand (Ω^n).
- *Identification of Specific Anatomic Locations.* The NPD framework allows to intuitively localize any anatomical point since each of them is labelled with a parameter relative to the structure boundaries and common to any subject.

On the other hand, the NPD framework enjoys the following advantages over existing coordinate systems:

- *Definition of segments/regions adapted to the subject-specific anatomy.* Since, by definition, coordinate curves faithfully describe the geometry of the anatomical structure (run parallel to its boundaries), segments adapted to such geometry are easily defined by means of a rectangular grid in Ω^n .
- *Local operations.* Local operations, such as interpolation or smoothing according to the geometry of the anatomical structure, can be done along the rectangular axis of Ω^n . For instance in the 2D case, coordinate directions over the manifold correspond to vertical (rows) and horizontal (columns) directions. This considerably simplifies the mathematical formulation and the computational cost.
- *Anatomical interpretation of vector-dependant scores.* Vectorial quantities expressed in the local reference system given by (4.3) have a clinical interpretation in terms of the anatomical structure (local references).
- *Visualization.* Values at Ω^n can be easily mapped to idealized templates (like bull's eyes plots or semiellipsoids) for a better visual interpretation of results.

4.3 Definition of the NPD for the Left Ventricle

In this section we compute the NPD framework of the LV for SA views (2D) in TMR sequences (for further LV function assessment) and for the whole volume in DTI images (for further LV anatomy modelling).

4.3.1 NPD in (2D) SA TMR Sequences

Since in the case of 2D SA views, LV can be regarded as a 2-dimensional manifold embedded into \mathbb{R}^2 , we consider the bi-dimensional NPD, $\Omega^2 = [0, 1] \times [0, 1]$. Since the LV is a time-evolving shape, we will use the superscript $t = 0, \dots, T_{ES}$ for indicating the systolic phases. Therefore \mathcal{LV}^t and Ψ^t will stand for a generic LV domain and its parametrization at time t . In the case of several subjects, the subscript n will be used to identify them and, since they may have different temporal resolution, we will denote by T_{ES_n} their end-systolic frame. A 2D point in the image, $(x, y) \in \mathbb{R}^2$, will be noted for short by \mathbf{x} . The parameter u stands for the circumferential direction, w for the radial one and the pair (u, w) will be denoted by \mathbf{u} .

The parametrization of the LV is based on anatomical features common to all subjects. This is the key for a successful implicit registration process. We propose using the segmentation of the LV boundaries to obtain a parametrization in angular and radial coordinates. The implicit registration of \mathcal{LV}^0 solves the problem of inter-patient variability. However, the intra-patient variability is still left. To register \mathcal{LV}^t for $t > 0$, we use the motion maps $\{V^t\}_{t=0}^{T_{ES}-1}$ of each sequence in order to update the parametrization at further phases of the systolic cycle. These motion maps are obtained from the analysis of TMR sequences using the Harmonic Phase Flow (HPF) method given in Chapter 3. Next, we give the details for parametrization of the LV in a two-fold process: the parametrization of \mathcal{LV}^0 and \mathcal{LV}^t , $t > 0$:

\mathcal{LV}^0 Parametrization

The parametrization of \mathcal{LV}^0 splits in 4 steps:

- *STEP1: Landmark Identification.* The inner (endocardium) and outer (epicardium) contours of \mathcal{LV}^0 are extracted and anatomical key-points are located.
- *STEP2: Anatomical Affine Reference.* An affine coordinate system based on \mathcal{LV}^0 anatomy is defined in order to account for variability in patient-device relative position.
- *STEP3: Boundaries Parametrization.* B-spline curves are fitted to endocardial and epicardial contours in the new affine reference in order to account for anatomic changes across subjects.
- *STEP4: Domain Parametrization.* Finally, the parametric map is obtained by fitting a bi-dimensional B-Spline to the domain defined by \mathcal{LV}^0 boundaries.

STEP1: Landmark Identification

Identification of anatomical landmarks is required for defining the anatomic reference and \mathcal{LV}_0 boundaries parametrization.

The set of \mathcal{LV}^0 boundary points will be denoted by \mathcal{ED} for the endocardium and \mathcal{EP} for the epicardium. Following [130], we manually identify them at positive times

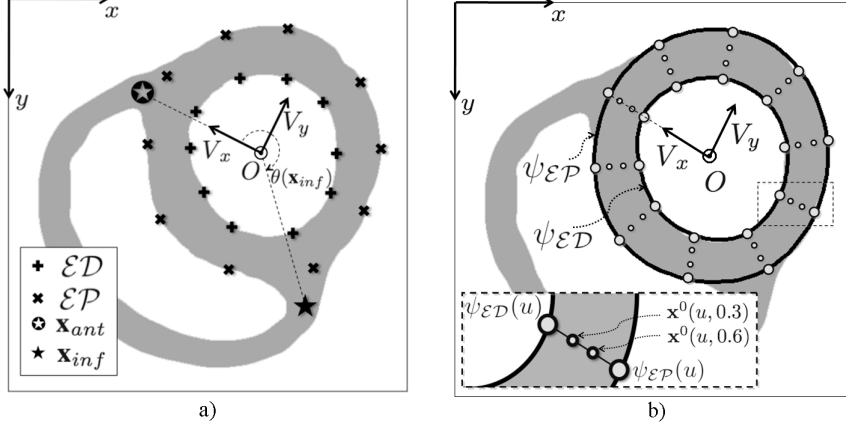


Figure 4.6: \mathcal{LV}_0 parametrization. a) Landmark identification (\mathcal{ED} , \mathcal{EP} , \mathbf{x}_{ant} and \mathbf{x}_{inf}) for the definition of the affine reference. b) \mathcal{LV}_0 boundaries parametrization and interpolation of intramural points, $\mathbf{x}^0(u, w)$.

and track them back to $t = 0$ using HPF. The number of points depends on the number of control points (linked to the degree of the blending functions) used for the B-spline. In our case, we use 12 for, both, endocardium and epicardium.

We also identify the junction points between left and right ventricles at anterior (\mathbf{x}_{ant}) and inferior (\mathbf{x}_{inf}) LV walls, respectively (fig. 4.6 (a)). \mathbf{x}_{ant} is used in the definition of the affine reference system accounting for affine variability in patient-device relative position, whereas the angular coordinates of \mathbf{x}_{inf} in such affine system serve to define the (average) portion of septal wall, G . Such value is taken into account for the definition of the circumferential coordinate (u) in order to register \mathcal{LV} anatomies. The points \mathbf{x}_{ant} , \mathbf{x}_{inf} should only indicate anatomic directions. Thus, they do not necessarily belong to the sets \mathcal{ED} and \mathcal{EP} .

STEP2: Anatomical Affine Reference

An affine coordinate system is defined by means of an origin of coordinates, O , and two linearly independent axis, V_x and V_y . The new origin is defined as the center of mass of \mathcal{ED} in order to compensate any translation among different subjects. The new x-axis, V_x , is a unitary vector starting at O and pointing to \mathbf{x}_{ant} . Finally, V_y is a unitary vector orthogonal to V_x and oriented oppositely to the septal wall. Since V_x points the same anatomical location for any LV, by setting V_x as the origin of angles, we handle any rotational disparity among different subjects. The scheme in Figure 4.6 (a) shows the anatomical reference and the image coordinate axis.

STEP3: \mathcal{LV}^0 Boundaries Parametrization

We compute a unified compact parametrization of \mathcal{LV}^0 boundaries by fitting (in the least squares sense [29]) a couple of B-Spline curves to \mathcal{ED} and \mathcal{EP} , expressed in the anatomic affine system. B-Splines are defined by a circumferential parameter,

$u \in [0, 1]$, ensuring implicit registration of \mathcal{LV}^0 across subjects.

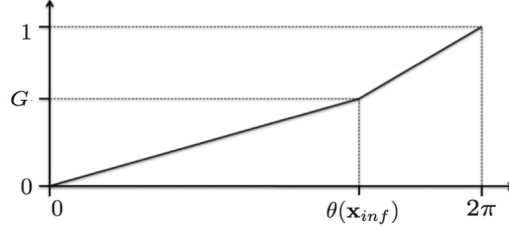


Figure 4.7: Piecewise linear parametrization function that maps all angles to a normalized interval, taking into account the proportion of septal and non-septal area.

Anatomic (implicit) registration is achieved by assigning a circumferential range $[0, G]$ to non-septal segments and $[G, 1]$ to the septal one. The transition parameter G is computed as the normalized average of the angular coordinate, $\theta \in [0, 2\pi]$, of \mathbf{x}_{inf} in the system $\{O, V_x, V_y\}$ for Q healthy volunteers:

$$G = \frac{1}{2\pi Q} \sum_{q=1}^Q \theta(\mathbf{x}_{inf}^q) \quad (4.9)$$

The normalized angular coordinate u is defined as (Fig. 4.7):

$$u(\mathbf{x}) = \begin{cases} \frac{G\theta(\mathbf{x})}{\theta(\mathbf{x}_{inf})}, & \theta(\mathbf{x}) \leq \theta(\mathbf{x}_{inf}) \\ \frac{(1-G)\theta(\mathbf{x}) + 2\pi G - \theta(\mathbf{x}_{inf})}{2\pi - \theta(\mathbf{x}_{inf})}, & \theta(\mathbf{x}) > \theta(\mathbf{x}_{inf}) \end{cases} \quad (4.10)$$

A couple of closed B-Spline curves,

$$\psi_{\mathcal{ED}}(u) = \sum_{i=1}^{M_u} R_i(u) P_i \quad \psi_{\mathcal{EP}}(u) = \sum_{i=1}^{M_u} R_i(u) P_i \quad (4.11)$$

with R_i cubic blending functions and $P_i \in \mathbb{R}^2$ control points ensuring a closed curve (i.e. $P_1 = P_{M_u-2}$, $P_2 = P_{M_u-1}$, $P_3 = P_{M_u}$) are fitted to the boundary points \mathcal{ED} and \mathcal{EP} by minimizing:

$$\sum_{\mathbf{x} \in \mathcal{ED}} \|\psi_{\mathcal{ED}}(u(\mathbf{x})) - \mathbf{x}\|^2 + \sum_{\mathbf{x} \in \mathcal{EP}} \|\psi_{\mathcal{EP}}(u(\mathbf{x})) - \mathbf{x}\|^2 \quad (4.12)$$

STEP4: \mathcal{LV}^0 Domain Parametrization

In order to get the final parametrization, $\Psi^0(u, w)$, we fit a bi-dimensional B-Spline to a uniform sampling of the radial values (normalized in the range $[0, 1]$) of

the two border splines. Since at end-diastole tissue has not any deformation, the radial direction can be linearly sampled [212]:

$$\mathbf{x}^0(u, w) = \psi_{\mathcal{E}\mathcal{D}}(u)w + \psi_{\mathcal{E}\mathcal{P}}(u)(1 - w), \quad (u, w) \in \Omega^2 \quad (4.13)$$

We evaluate the above equation at a $N_u \times N_w$ uniform grid in Ω^2 given by $u_i = (i - 1)/(N_u - 1)$ and $w_j = (j - 1)/(N_w - 1)$. This provides $N_u \times N_w$ myocardial points, $\{\mathbf{x}_{ij}^0\}_{i,j=1}^{N_u, N_w}$, at the initial time. These points are equiangular in the circumferential direction for each segment (septal and non-septal) and equidistant in the radial one. Figure 4.6 (b) shows the sampling given by a grid of 10×4 points. The close-up illustrates the linear interpolation of radial positions from the 2 boundaries.

The parametric map is obtained by fitting a bi-dimensional B-Spline surface to $\{\mathbf{x}_{ij}^0\}_{i,j=1}^{N_u, N_w}$. The B-spline surface is given by:

$$\Psi^0(u, w) = \sum_{i=1}^{M_u} \sum_{j=1}^{M_w} R_i(u)S_j(w)P_{ij} \quad (4.14)$$

for R_i cubic blending functions, S_j quadratic blending functions and $P_{ij} \in \mathbb{R}^2$ $M_u \times M_w$ control points ensuring a closed surface along the circumferential direction. Control points are given by minimizing:

$$\sum_{i=1}^{N_u} \sum_{j=1}^{N_w} \|\Psi^0(u_i, w_j) - \mathbf{x}_{ij}^0\|^2 \quad (4.15)$$

$\mathcal{L}\mathcal{V}^t$ Parametrization

The domain $\mathcal{L}\mathcal{V}^t$ is parameterized by fitting a B-spline surface to a set of points sampled on the $\mathcal{L}\mathcal{V}^t$ domain. Such points are obtained by updating points on $\mathcal{L}\mathcal{V}^0$ according to the displacement, V^t , observed between consecutive TMR images and computed by means of HPF. The $\mathcal{L}\mathcal{V}^0$ points are given by evaluating Ψ^0 at a $N_u \times N_w$ uniform sampling defined by $u_i = (i - 1)/(N_u - 1)$ and $w_j = (j - 1)/(N_w - 1)$. Myocardial points at positive times, \mathbf{x}_{ij}^t , are obtained by iteratively applying V^t (HPF-based tracking):

$$\mathbf{x}_{ij}^t = \begin{cases} \mathbf{x}_{ij}^0 & t = 0 \\ \mathbf{x}_{ij}^{t-1} + V^{t-1}(\mathbf{x}_{ij}^{t-1}), & t > 0 \end{cases} \quad (4.16)$$

The mapping Ψ^t is the minimum of the cost functional given by changing \mathbf{x}_{ij}^0 for \mathbf{x}_{ij}^t in (4.15). Notice that parameters remain fix. The above procedure ensures that, regardless the patient and time, a given parameter $(u, v) \in \Omega^2$ always corresponds to the same anatomical location in the $\mathcal{L}\mathcal{V}$.

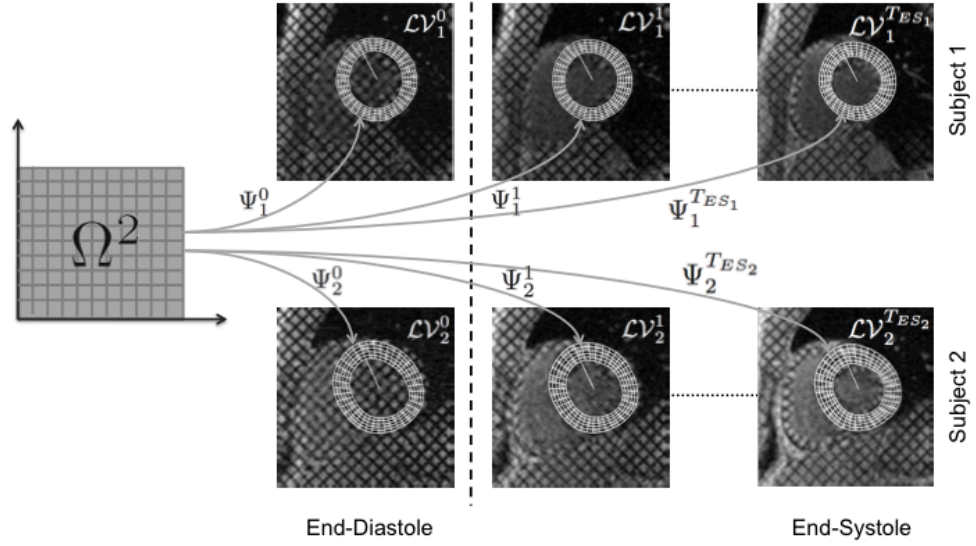


Figure 4.8: Implicit Registration of two TMR sequences belonging to different subjects. Each parametrization Ψ_n^t defines a coordinate system tailored for the geometry of each subject and time. Same anatomical locations share the same parameter in Ω^2 .

We have just defined a procedure to explicitly obtain the NPF framework for the LV as seen in 2D SA sequences. This is, we have given a means computing the parametrization maps Ψ_n^t , fulfilling the properties of the NPD framework stated in Definition 4.2.1, for any subject at any time. Figure 4.8 shows that parametric maps implicitly registers the LV in a sequence for two subjects. On the other hand, Figure 4.9 shows that the parametric directions have an anatomical meaning.

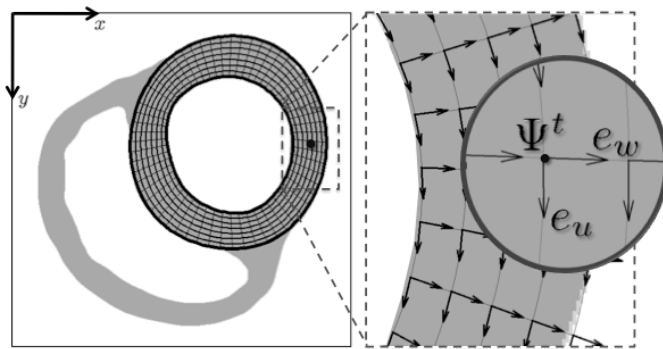


Figure 4.9: Parametric directions fitting LV geometry and detail of the local coordinate systems $\{e_u, e_w\}$ (along circumferential and radial directions resp.) induced by the parametrization Ψ^t .

4.3.2 NPD in (3D) DTI Volumes

DTI volumes are given by (3D) image blocs $I(x, y, z)$ of size $N_x \times N_y \times N_z$. It follows that, in this case, the NPD is the unitary cube $\Omega^3 = [0, 1] \times [0, 1] \times [0, 1]$. The parametric coordinates (u, v, w) stand for the circumferential, longitudinal and radial directions. As in the 2D case, a parametric point will be noted by \mathbf{u} and a 3D point in the \mathcal{LV} volume by \mathbf{x} . In this case, since DTI volumes are static, we will only use a subscript n identifying different subjects.

The parametrization of \mathcal{LV} splits in 3 steps and, as the 2D case, it uses (3D) anatomical landmarks:

- *STEP1: Landmark Identification.* In this step the main axis of the LV (long axis) is estimated. Next, several tomographic SA and LA slices from the 3D volume are selected in order to segment LV boundaries and locate anatomical landmarks.
- *STEP2: Anatomical Affine Reference.* An affine coordinate system based on \mathcal{LV} anatomy is defined in order to account for variability in patient-device relative position.
- *STEP3: \mathcal{LV} Parametrization.* Finally, the parametric map is obtained by fitting a 3D B-Spline to the domain defined by wire-frames depicting LV silhouette.

STEP1: Landmark Identification.

Localizing LV Main Axis

The LV long axis is defined as the line through the apical cap, A , and the centroid of the endocardial basal ring, B . Although excised hearts are placed in the MR device so that this axis is aligned to the z axis of the scanner, in practice this condition is not exactly fulfilled. We estimate the long axis computing A and B as follows.

Let $I(x, y, z)$ represent the DTI geometrical volume, in order to obtain A , we consider a couple of 'X-Ray like' images given by the projection of I along the x -direction (projected $y - z$ image, $I_1(y, z)$) and y -direction (projected $x - z$ image, $I_2(x, z)$):

$$I_1(y, z) = \frac{1}{N_x} \sum_{x=1}^{N_x} I(x, y, z) \quad I_2(x, z) = \frac{1}{N_y} \sum_{y=1}^{N_y} I(x, y, z) \quad (4.17)$$

These 'X-Ray' images are used to manually locate the points of the (projected) apical caps. If $A_1 = (y_1, z_1)$ and $A_2 = (x_2, z_2)$ are these positions, then the true apical cap is estimated as:

$$A = (x_2, y_1, \frac{z_1 + z_2}{2}) \quad (4.18)$$

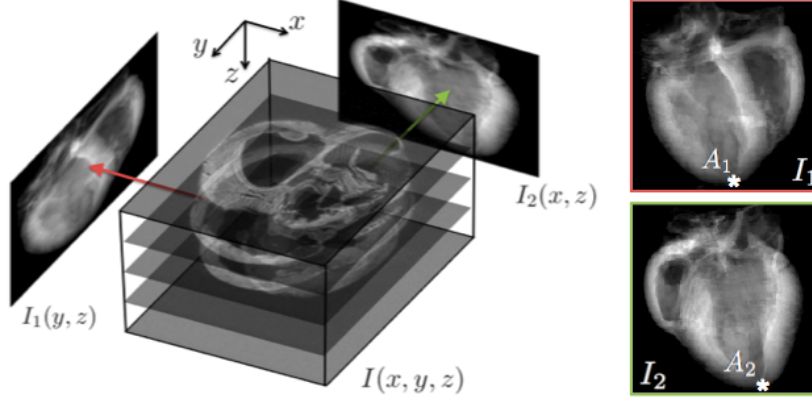


Figure 4.10: Location of the LV axis. On the left hand side, we sketch the creation of the X-Ray like images I_1 and I_2 , that are used to locate keypoints A_1 and A_2 for the estimation of the apical cap. On the right images we show both projections with the 2 points (A_1 and A_2) marked with a star.

Figure 4.10 illustrates the strategy for obtaining the 'X-Ray' images from the geometric volume and the estimation of the apical cap from them.

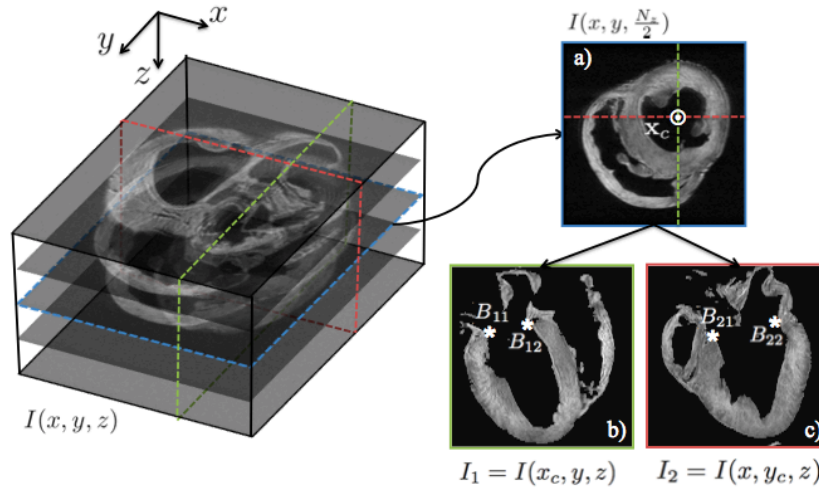


Figure 4.11: Location of the LV axis. Selection of appropriate LA slices and landmarking keypoints B_{11} , B_{12} , B_{21} and B_{22} for the estimation of the basal ring centroid.

In order to obtain the endocardial basal ring centroid, B , we proceed as follows. First (Fig. 4.11 (a)), we select the LV centroid, $\mathbf{x}_c = (x_c, y_c)$, from an intermediate SA slice given by $I(x, y, \frac{N_z}{2})$. Next, we select points on the (endocardial) basal ring on 2 LA cuts (Fig. 4.11 (b) and (c)) through \mathbf{x}_c given by $I_1 = I(x_c, y, z)$ and $I_2 = I(x, y_c, z)$. This provides 2-tuples of points (one for each image) of coordinates $\{B_{11} = (y_{11}, z_{11}), B_{12} = (y_{12}, z_{12})\}$ for I_1 and $\{B_{21} = (x_{21}, z_{21}), B_{22} = (x_{22}, z_{22})\}$ for I_2 .

Finally, the basal ring centroid is estimated by the average:

$$B = \left(\frac{x_{21} + x_{22}}{2}, \frac{y_{11} + y_{12}}{2}, \frac{z_{11} + z_{12} + z_{21} + z_{22}}{4} \right) \quad (4.19)$$

Figure 4.11 sketches the strategy for computing the basal ring centroid. The intermediate SA slice with the LV centroid \mathbf{x}_c (corresponding to the blue plane in the volume on the left) is shown in Figure 4.11 (a). The green and the red lines correspond to the 2 LA cuts through \mathbf{x}_c . Such cuts (green and red planes on the left volume) are shown in Figure 4.11 (b) and (c), respectively. The 2 points on the basal ring are marked with an asterisk.

The direction of the LV axis is defined as the unitary vector:

$$V_z = \frac{B - A}{\|B - A\|_2} \quad (4.20)$$

Slice Selection and Segmentation

We select several tomographic belonging to two different sets: those that are perpendicular to V_z (SA cuts), and those parallel to it (LA cuts). For the SA set we consider N_{SA} slices uniformly covering the LV from apex to base (Figure 4.12 (A)). For the LA set we consider N_{LA} slices uniformly covering the circumferential direction and mutually intersecting at the axis of the LV (Figure 4.12 (B)).

The basal ring profile is outlined by means of the N_{LA} LA slices, denoted as LA_l for $l = 1 \div N_{LA}$. In each slice LA_l , the two endocardial and epicardial basal edge points are manually selected. The collection of epicardial and endocardial points for all LA_l constitutes, respectively, our approximation to endocardial and epicardial wire-frames of the basal ring. They are denoted as \mathcal{W}_0^0 and \mathcal{W}_0^1 . Here the subscript 0 indicates the basal ring, whereas the superscripts 0 and 1 indicate the endocardium and epicardium respectively. The remaining contours follow from the segmentation of LV boundaries on the N_{SA} SA slices, SA_s , $s = 1 \div N_{SA}$. Endocardial points will be noted \mathcal{W}_s^0 and epicardial ones \mathcal{W}_s^1 . Here the subscript references the SA slices containing the points.

Similarly as in the 2D case, for each slice SA_s the junction between both ventricles at anterior wall is identified and denoted by \mathbf{x}_{ant}^s .

STEP2: Anatomical Affine Reference.

In 3D, an affine reference system is given by the origin O and 3 axis, V_x , V_y and V_z . The new origin is defined [212] as:

$$O = A + \frac{2}{3}(B - A) \quad (4.21)$$

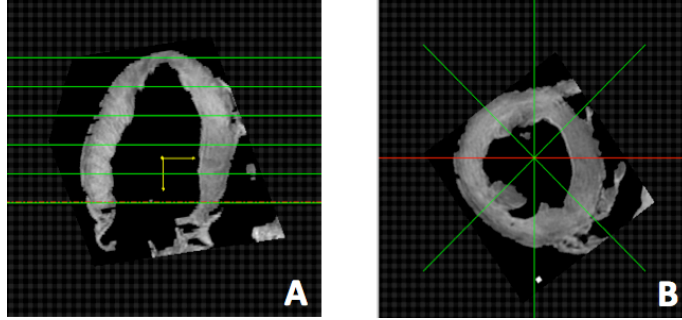


Figure 4.12: Tomographic slices perpendicular (A) and parallel (B) to the long axis of the LV.

in order to account for any translation among different subjects. The z -axis is tangent to the main axis of the LV, and is given by equation (4.20). The x -axis is given by the normalized average of the projections of $\{\mathbf{x}_{ant}^s - O\}$ onto the plane through O perpendicular to V_z . Notice that, by setting V_x as the origin of angles, we handle any rotational disparity among different subjects. Finally, V_y is a unitary vector chosen to point oppositely to the septal wall and perpendicular to V_x and V_z . In this manner, the anatomic affine reference is orthonormal and positively oriented.

STEP3: \mathcal{LV} Parametrization.

We compute a unified compact parametrization of the LV by fitting (in the least squares sense) a 3D B-Spline to the \mathcal{LV} domain. In order to fit the B-Spline we need to gather a representative (of the LV geometry) set of points and assign them normalized circumferential, longitudinal and radial parameters. Parameter assignment must take into account anatomical features in order to ensure \mathcal{LV} implicit registration across subjects.

Circumferential parameter u

Let $\theta : \mathbb{R}^3 \rightarrow [0, 2\pi]$ be a function that returns the angle of any point $\mathbf{x} \in \mathbb{R}^3$ (in the new anatomic reference) about the long axis V_z . Given a point \mathbf{x} , we assign to it a normalized circumferential parameter as:

$$u(\mathbf{x}) = \frac{\theta(\mathbf{x})}{2\pi} \in [0, 1] \quad (4.22)$$

Considering this parametrization, a closed B-Spline curve (wire-frame) can be fitted to any of the sets \mathcal{W}_s^k for $s = 0 \div N_{SA}$ and $k = 0, 1$ in the least squares sense (as done in *STEP3* of Section 4.3.1). This yields to a set of wire-frames ψ_s^k depicting the \mathcal{LV} silhouette (see Figure 4.13).

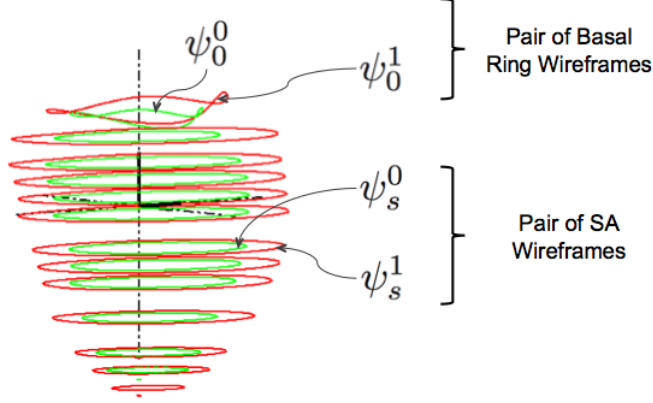


Figure 4.13: Wire-frames depicting LV silhouette. Red ones belong to the endocardium (ψ_s^0) and green ones to the epicardium (ψ_s^1). Basal ring wireframes are denoted by $s = 0$ and SA wireframes by $s = 1 \div N_{SA}$.

Radial parameter w

For each pair of wire-frames belonging to endocardium and epicardium $\{\psi_s^0, \psi_s^1\}$, we can generate points inside the \mathcal{LV} by linearly interpolating the B-Spline curves in a fixed circumferential parameter $u \in [0, 1]$. These points can be expressed as

$$\mathbf{x}_s(u, w) = \psi_s^0(u)(1 - w) + \psi_s^1(u)w \quad s = 0 \div N_{SA} \quad (4.23)$$

Now, for each of these points we already know both, their circumferential ($u \in [0, 1]$) and radial ($w \in [0, 1]$) parameters.

Longitudinal parameter v

Finally, we need to compute the normalized longitudinal parameter. Let

$$\mathbf{x}_s(u, w) = (x_s(u, w), y_s(u, w), z_s(u, w))$$

be the components of points generated by equation (4.23), we define their normalized longitudinal parameter such that points in the basal ring are assigned value 1 and the apical cap is assigned value 0. Points in between are assigned angular values (in spherical coordinates) normalized according to the angular values of their associated basal ring points. These criteria are condensed in the following equation:

$$v_s(u, w) = \frac{\pi - \arccos\left(\frac{z_s(u, w)}{\|z_s(u, w)\|}\right)}{\pi - \arccos\left(\frac{z_0(u, w)}{\|z_0(u, w)\|}\right)} \quad (4.24)$$

Volume Parametrization

For the final parametrization of the whole \mathcal{LV} , for all $s = 0 \div N_{SA}$ we consider a set of points generated with equation (4.23) using a uniform sampling of Ω^2 . Since for any of these points we know its associated set of normalized circumferential, longitudinal and radial parameters, we fit a 3D-BSpline

$$\Psi(u, v, w) = \sum_{i=1}^{M_u} \sum_{j=1}^{M_v} \sum_{k=1}^{M_w} R_i(u) S_j(v) T_k(w) P_{ijk} \quad (4.25)$$

in the least squares sense by minimizing

$$\sum_{\mathbf{x} \in \{\mathcal{W}_s^k\}} \|\Psi(u(\mathbf{x}), v(\mathbf{x}), w(\mathbf{x})) - \mathbf{x}\|^2 \quad s = 0 \div N_{SA}, \quad k = 0, 1 \quad (4.26)$$

R_i and S_j are cubic blending functions, T_k is linear (linear interpolation along radial direction) and $P_{ijk} \in \mathbb{R}^3$ are control points ensuring that the B-Spline is closed along the circumferential direction.

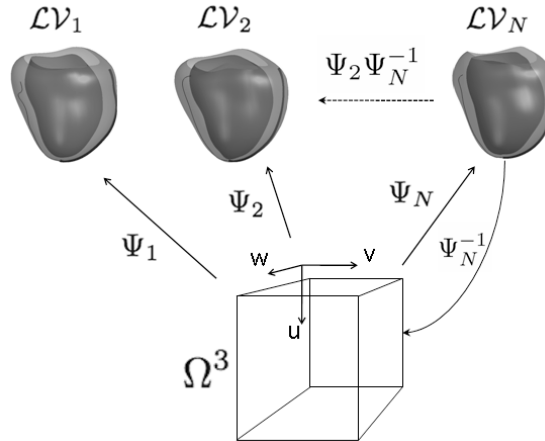


Figure 4.14: Implicit registration of the \mathcal{LV}_n of different subjects. Each parametrization Ψ_n defines a coordinate system tailored for the geometry of each subject. Same anatomical location share the same parameter in Ω^3 .

Figure 4.14 illustrates the implicit registration of \mathcal{LV} volumes for several subjects, given by their parameterizations. Figure 4.15 shows that the parametric directions are aligned with the circumferential, longitudinal and radial directions of the LV. Notice that the differential of the parametrization maps the canonical basis of \mathbb{R}^3 to the local references describing the parametric directions.

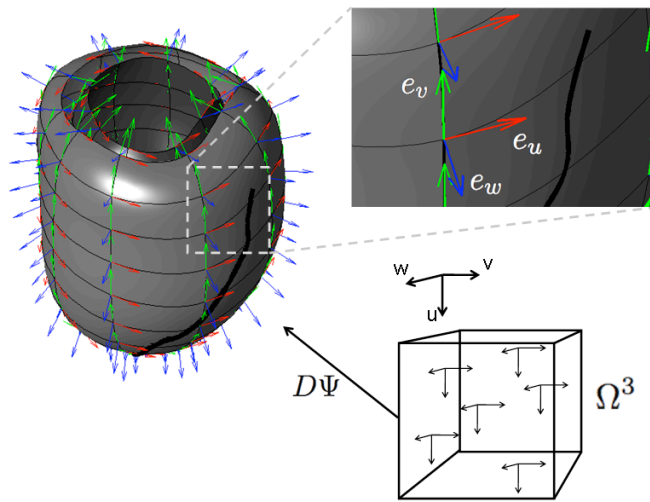


Figure 4.15: Parametric directions fitting LV geometry and detail of the local coordinate systems $\{e_u, e_v, e_w\}$ (along circumferential, longitudinal and radial directions resp.) induced by the parametrization Ψ .

Chapter 5

Anatomy Modelling

Current approaches for building statistical models of the LV consider separately the gross geometry and the fiber architecture. In this Chapter we use the NPD as unifying framework for statistically modelling both of them. Regarding the gross anatomy, we compute the average and the modes of variation of the parametric mappings for several subjects. Meanwhile for the modelling of myocardial fibers, statistical analysis over unitary vectors (lying on a semisphere) is performed in Ω^3 . In the first case, given that the parametric mappings are defined by B-Splines, we use their control points in order to compute Point Distribution Models (PDM). In the second case, since the semisphere does not have space vector structure, the addition operation is not well defined and, thus, Riemmanian metrics are required.

5.1 Gross Anatomy Modelling

The most common approach for the modelling of shape variations in anatomical structures are PDM (or Active Shape Models). They base on a discrete sampling of LV geometry, which accuracy is bounded by the sampling resolution. Continuous approaches achieve maximum resolution but require complex statistics.

5.1.1 Control Point-Based LV Atlas

By means of parametrization maps, our NPD framework has the ability to continuously describe the geometry of the LV and implicitly registering it in Ω^3 . By using B-Splines, the set of parametric maps has a vectorial structure. This follows from the fact that B-Splines are linear combinations of a finite number of blending functions weighted by control points. Thus, control points may be used to model LV shape variations as in PDM.

Consistency Condition

A main requirement for the PDM to be statistically meaningful, is that the selected landmarks must be consistent. This is, they must represent the same anatomical location for any subject. Since in our case control points play the role of anatomical landmarks, they should influence equivalent anatomical areas for any subject.

Let us see that the above consistency condition is fulfilled. For the sake of simplicity, we restrict to 1-dimensional uniform B-Splines. For a given number of control points, M , and blending functions of order n (i.e., degree $n - 1$), the number of knots, $(M + n)$, is automatically defined. The knot vector may be any sequence of $(M + n)$ non-decreasing and equidistant real numbers: $\{u_0 \leq u_1 \leq \dots \leq u_{M+n-1}\}$. The sequence defines the parametric domain $[u_0, u_{M+n-1}]$ and splits it into several portions where B-Spline basis blending functions ($B_i(t)$) have compact support. In other words, each B_i (computed using the Cox-de Boor recurrent formula [50]) vanishes outside the interval $[u_i, u_{i+n}]$. A B-Spline function f is a linear combination of the B_i 's weighted by the control points, P_i :

$$\sum_{i=1}^M B_i(t)P_i \quad (5.1)$$

In order to model constant functions $\sum_{i=1}^M B_i = 1$, equation (5.1) only makes sense in the interval $u \in [u_{n-1}, u_M]$ which, by definition (in our case), equals $[0, 1]$ for all cases. Since P_i weights B_i , its area of influence restricts to the support of B_i . Therefore, if parametric ranges correspond to equivalent anatomic structures, the consistency requirement holds. This is precisely our case since the assignment of parametric ranges have been done using equally anatomical landmarks for all subjects.

Building the Atlas

Given a training set of N subjects, we consider their parametrization (see Sec. 4.3.2):

$$\Psi_n(u, v, w) = \sum_{i=1}^{M_u} \sum_{j=1}^{M_v} \sum_{k=1}^{M_w} R_{i,n}(u)S_{j,n}(v)T_{k,n}(w)P_{ijk,n}, \quad n = 1, \dots, N$$

where $P_{ijk,n} = (P_{ijk,n}^x, P_{ijk,n}^y, P_{ijk,n}^z)$ are the control points. Following PDM, for each subject we codify its gross anatomy by concatenating the components of these control points (vector of observations). This is:

$$\mathbf{P}_n = (P_{100,n}^x, P_{100,n}^y, P_{100,n}^z, \dots, P_{M_u M_v M_w, n}^x, P_{M_u M_v M_w, n}^y, P_{M_u M_v M_w, n}^z) \quad (5.2)$$

belonging to $\mathbb{R}^{3 \times M_u \times M_v \times M_w}$.

The geometry of the LV (and objects in general) is independent on its scale, orientation and position. Thus, before performing any statistical analysis of the training shapes, such variations must be removed. In our case, the removal of these transformations can be directly done over the control points since B-Splines are invariant under a scale, rotation and translation of the control points. This is achieved using Procrustes Analysis [72].

The set of all aligned observations, $\{\mathbf{P}_n\}_{n=1}^N$, form a cloud of points in $\mathbb{R}^{3 \times M_u \times M_v \times M_w}$, that we assume to follow a Gaussian distribution. In order to capture the statistics of the shape variations, we compute a PDM. First of all, the mean shape ($\bar{\mathbf{P}}$) and covariance matrix (S) are computed:

$$\bar{\mathbf{P}} = \frac{1}{N} \sum_{n=1}^N \mathbf{P}_n \quad (5.3)$$

$$S = \frac{1}{(N-1)} \sum_{n=1}^N (\mathbf{P}_n - \bar{\mathbf{P}})(\mathbf{P}_n - \bar{\mathbf{P}})^T \quad (5.4)$$

The eigenvectors (ϕ_n) of S encode the modes of variation of the mean model and the eigenvalues (λ_n), the relevance of such mode. Since in our case $N \ll 3 \times M_u \times M_v \times M_w$, at most N eigenvectors (spanning the subspace generated by the observations) can be obtained. Dimensionality reduction is achieved by considering just the most relevant modes of variation (principal components). Such relevancy can be measured by the proportion of the total variance explained by each eigenvector, which is given by its corresponding eigenvalue. The number of selected eigenvectors, d , is chosen so that the model represents a given percentage, *prc*, of the total variance given by the sum of all the eigenvalues:

$$\Gamma = \sum_{n=1}^N \lambda_n \quad (5.5)$$

Therefore, d is the smallest number such that,

$$\sum_{n=1}^d \lambda_n \geq \frac{prc\Gamma}{100} \quad (5.6)$$

where the eigenvalues are sorted in descending order ($\lambda_n \leq \lambda_{n+1}$).

Considering the first d modes of variation, each shape \mathbf{P} in the training set can be approximated by projecting it into the subspace spanned by $\{\phi_n\}_{n=1}^d$. This is

$$\mathbf{P} \approx \bar{\mathbf{P}} + \Phi b \quad (5.7)$$

where $\Phi = (\phi_1 | \phi_2 | \dots | \phi_d)$, and

$$b = \Phi^T(\mathbf{P} - \bar{\mathbf{P}}). \quad (5.8)$$

In addition, equation (5.7) may be used to generate new shapes similar to those of the training set by moving the parameter $b = (b_1, \dots, b_d)$ in a suitable range. Since the parameters b_n are assumed to be independent and Gaussian, the variance across the training set of an individual parameter b_n is given by λ_n . We can, thus, ensure that the shape generated is similar to those in the original training set by applying limits of $\pm 2\sqrt{\lambda_n}$ to the parameter b_n . These limits represent ± 2 standard deviations along the mode.

5.2 Fiber Modelling

Unitary eigenvectors V obtained from parameterized DTI volumes are mapped to Ω^3 for their statistical analysis by considering their resized components (V_u, V_v, V_w) in the local references $\{e_u, e_v, e_w\}$ (Sec. 4.1.1). Given that we are only interested in fiber orientations (regardless the magnitude), we normalize vectors such that they belong to the unitary sphere S^2 :

$$V_u = \frac{V_u}{\sqrt{V_u^2 + V_v^2 + V_w^2}}, \quad V_v = \frac{V_v}{\sqrt{V_u^2 + V_v^2 + V_w^2}}, \quad V_w = \frac{V_w}{\sqrt{V_u^2 + V_v^2 + V_w^2}} \quad (5.9)$$

DTI eigenvectors have a randomly assigned orientation. Again, since we are only interested in their direction, we reorient vectors so that they all have the same orientation according to the longitudinal direction of the local references:

$$(V_u, V_v, V_w) = \begin{cases} (V_u, V_v, V_w), & V_v \geq 0 \\ -(V_u, V_v, V_w), & V_v < 0 \end{cases} \quad (5.10)$$

The reorientation makes eigenvectors lie in the upper (positive) semisphere (S^{2+}). The DTI vectors normalized and reoriented in Ω^3 will be noted by ξ .

5.2.1 Principal Eigenvector Statistics

The formulation of descriptive statistics (mean and standard deviation) in an Euclidean (vector) space, relies on the fact that the addition is a well defined operation. If $\{\xi_n\}_{n=1}^N$ is a set of observations of a random variable, their mean, $\bar{\xi}$ and variance, σ^2 , are estimated by:

$$\bar{\xi} = \frac{1}{N} \sum_{n=1}^N \xi_n \quad \sigma^2 = \frac{1}{N} \sum_{n=1}^N (\xi_n - \bar{\xi})^2$$

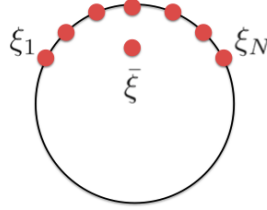


Figure 5.1: Scheme illustrating that arithmetic mean provide, for observations over manifolds, a result that does not lie over the manifold.

In the case of manifolds the above formulation does not hold because they do not present a vector space structure and, thus, the addition is not well defined. Figure 5.1 illustrates this phenomenon in the case of a circle. Notice that the arithmetic mean of several observations over the manifold does not lie in the manifold. In order to compute statistics on manifolds, the concept of mean and variance should be generalized [12, 132, 151, 153]. The key point for their extension relies on the fact that the mean is, indeed, the value that minimizes the function of the square distances

$$\min_{\bar{\xi} \in \mathbb{R}^m} \frac{1}{N} \sum_{n=1}^N \|\xi_n - \bar{\xi}\|_2^2 \quad (5.11)$$

for $\|\cdot\|_2^2$ the Euclidean distance, and the minimum of such function is the variance. Therefore, the concepts can be extended to manifolds, provided that they do have a distance. In such case, the average is the point on the manifold minimizing

$$\min_{\bar{\xi} \in \mathcal{M}} \frac{1}{N} \sum_{n=1}^N d(\xi_n, \bar{\xi})^2 \quad (5.12)$$

for d the distance in the manifold \mathcal{M} . The extension of the arithmetic mean to manifolds is called the Frechet mean [151] and manifolds endowed with a distance are called Riemmanian manifolds. The distance in a Riemmanian manifold is given by the length of the 'straight' line connecting 2 points, which is called geodesic. Although geodesics are intrinsic curves which only depend on the manifold geometry, their formulation and handling requires a parametrization. Among all possible parameterizations of a given manifold, the exponential map is specially well-suited for geodesics computation. The exponential map locally parameterizes the manifold by its tangent space. More precisely, it is an application defined in a neighborhood of each point, $\xi \in \mathcal{M}$, that maps vectors from the tangent space to points in the manifold by means of geodesics:

$$\begin{aligned} \exp_{\xi} : T_{\xi} \mathcal{M} &\longrightarrow \mathcal{M} \\ v &\longmapsto \exp_{\xi} v = \gamma_{\xi, v}(1) \end{aligned} \quad (5.13)$$

with $\gamma_{\xi,v}$ the unique geodesic satisfying $\gamma_{\xi,v}(0) = \xi$ with initial tangent vector $\dot{\gamma}_{\xi,v}(0) = v$. The inverse of \exp_{ξ} (called logarithm) maps points in \mathcal{M} to $T_{\xi}\mathcal{M}$ where standard Euclidean metrics may be used. Since the exponential map is not an isometry, the computation of the mean value requires the application of an iterative scheme [151] given by:

$$\begin{cases} \xi_0 \\ \xi_{i+1} = \exp_{\xi_i} \left(\frac{1}{N} \sum_n \exp_{\xi_i}^{-1}(\xi_n) \right) \end{cases} \quad (5.14)$$

The iterative scheme converges as long as the samples ξ_n do not cover more than one semisphere. Concerning the standard deviation, since the exponential map is a radial isometry, it is computed as the standard covariance matrix of the tangent space at $\bar{\xi}$ (see Fig. 5.2).

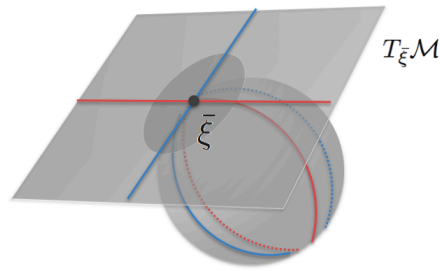


Figure 5.2: The exponential map generates a radial isometry between the manifold and the tangent space. Covariance can be computed on the tangent space using standard techniques.

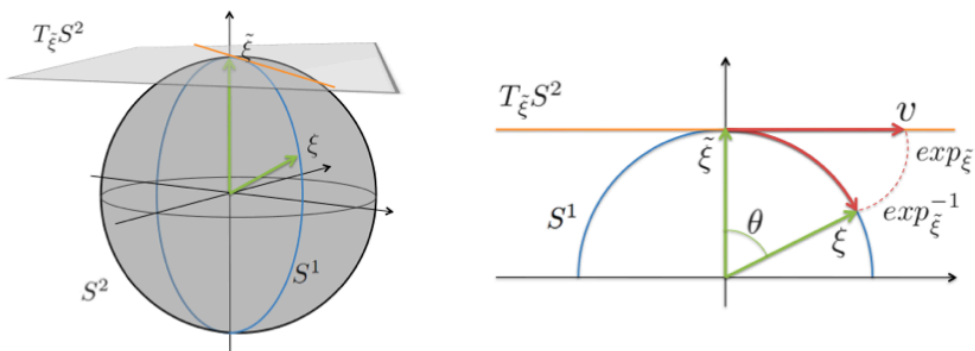


Figure 5.3: Exponential map associated to the point $\bar{\xi}$ and its inverse. Detail on the right depicts the situation over a maximum circle.

Computing the Exponential Map of the Sphere

The computation of the exponential map is a hard task in general, since it involves second order differential equations. However in the case of the sphere, it can be easily computed by means of angular differences.

Fixed a point $\tilde{\xi} \in S^2$ and given any other point $\xi \in S^2$, they generate a plane passing through the origin which intersection with S^2 provides a maximum circle, S^1 (blue circle in Figure 5.3 left). The angle, θ , between $\tilde{\xi}$ and ξ (Fig. 5.3 right) gives a relation between the circle and the tangent space $T_{\tilde{\xi}}S^2$ that preserves metrics. That is, the distance between points on the circle equals the Euclidean distance on the line generated by the intersection of the above plane and $T_{\tilde{\xi}}S^2$ (orange line in Figure 5.3).

This relation is the exponential map and in the case of the sphere is defined as follows:

$$\exp_{\tilde{\xi}}(v) = R_{(v \times \tilde{\xi}, \frac{\pi}{2} - \|v\|)} v \quad \forall v \in T_{\tilde{\xi}}S^2 / \|v\| \leq \frac{\pi}{2} \quad (5.15)$$

for R the matrix that rotates v in $\frac{\pi}{2} - \|v\|$ radians about the axis through the origin of coordinates and perpendicular to, both, v and $\tilde{\xi}$ (given by the cross product $v \times \tilde{\xi}$). Notice that in this case the exponential map is defined just in $\|v\| \leq \pi/2$. On the other hand, the logarithm map (inverse mapping) is defined as follows:

$$\exp_{\tilde{\xi}}^{-1}(\xi) = \theta \tilde{\xi}^\perp \quad (5.16)$$

where

$$\tilde{\xi}^\perp = \frac{\xi - \langle \xi, \tilde{\xi} \rangle \tilde{\xi}}{\|\xi - \langle \xi, \tilde{\xi} \rangle \tilde{\xi}\|}, \quad \theta = \arccos(\langle \xi, \tilde{\xi} \rangle)$$

In order to apply the iterative scheme (eq. 5.14), we set the initial value to

$$\xi_0 = \frac{\frac{1}{N} \sum_{n=1}^N \xi_n}{\|\frac{1}{N} \sum_{n=1}^N \xi_n\|} \quad (5.17)$$

which is the arithmetic mean of the observations, normalized in order to lie in S^2 . Figure 5.3 right, shows the details of the relation between points in the maximum circle and vectors in the tangent space.

5.3 Visualization of Fibers Architecture

In this Section we develop a coloring method for the enhanced visualization of the fiber disposition in the LV according to their orientation referred to the local references.

The method is designed to maximize the contrast between zones that contain fibers running in opposite directions.

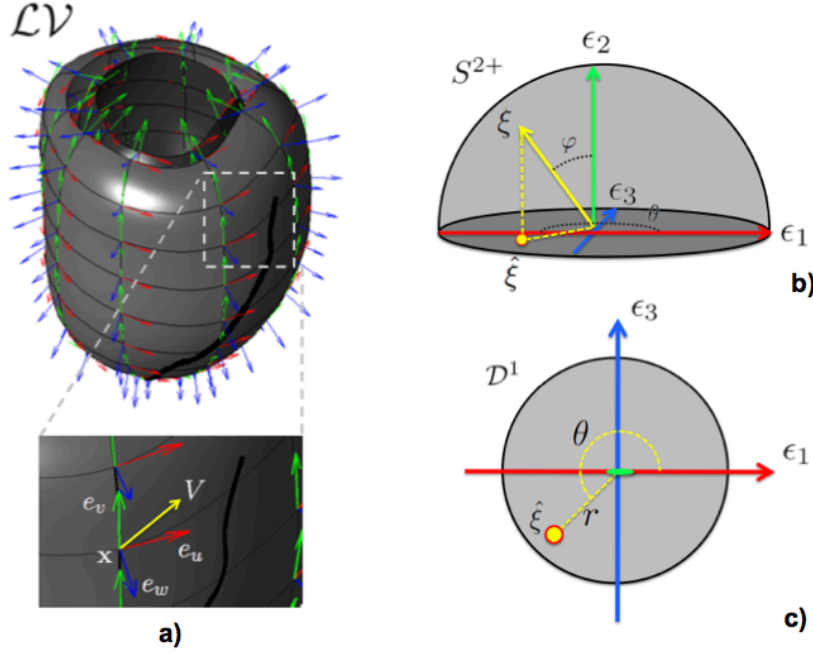


Figure 5.4: Correspondence between myocardial fibers and points in the unitary disk, \mathcal{D}^1 . a) A fiber at point $\mathbf{x} \in \mathcal{LV}$ is represented by a unitary vector V expressed in terms of local references $\{e_u, e_v, e_w\}$. b) V mapped to the NPD lives in a unitary semisphere S^{2+} where is noted by ξ . ξ might be expressed in terms of a couple of angles, θ and φ , which codify respectively the orientation and the elevation angle of the fiber, with respect the loca reference. c) S^{2+} is isomorph the unitary disk \mathcal{D}^1 via orthogonal projection. Orientation and elevation angles are now codified by θ and r . Each fiber is characterized by this couple of values.

For any $\mathbf{x} \in \mathcal{LV}$, let $V(\mathbf{x})$ be the unitary eigenvector codifying the direction of a fiber at this point (Fig. 5.4 (a)) and ξ its normalized and reoriented version in Ω^3 , which lies in S^{2+} (Fig. 5.4 (b)). In spherical coordinates, ξ might be expressed in terms of two angles θ and φ :

$$\xi(\theta, \varphi) = (\cos(\varphi)\cos(\theta), \cos(\varphi)\sin(\theta), \sin(\varphi)), \quad \theta \in [0, 2\pi], \quad \varphi \in \left[-\frac{\pi}{2}, \frac{\pi}{2}\right] \quad (5.18)$$

where θ codifies the orientation of the fiber and φ its elevation angle. By orthogonal projection onto the plane $z = 0$, the positive semisphere identifies (i.e., is isomorphic) to the unitary disk \mathcal{D}^1 (see Fig. 5.4 (c)). Let $\hat{\xi}$ be the projection of ξ onto \mathcal{D}^1 . In polar coordinates, $\hat{\xi}$ might be expressed in terms of an angle and a radius:

$$\hat{\xi}(\theta, r) = r(\cos(\theta), \sin(\theta)), \quad \theta \in [0, 2\pi], \quad r \in [0, 1] \quad (5.19)$$

where $r = \cos(\varphi)$. Now r codifies the elevation angle. That is, the smaller r is, the higher the elevation of the fiber is. This way, any fiber is assigned a pair of values characterizing its orientation relative to the local reference (describing anatomical directions): θ and r , for $\theta \in [0, 2\pi]$ and $r \in [0, 1]$. In order to provide an enhanced visualization of the myocardial fibers structure, we assign them a color according to their values θ and r . To do so, we have imposed RGB colors to 5 strategic points in the disk and we have interpolated (bilinearly) the RGB values at the rest. In Figure 5.5 we show a table containing the RGB colors for such points on the left and their location inside the disk in the right. Notice that the color itself codifies the orientation, whereas the tone codifies the elevation. The brighter the tone is, the higher the elevation angle is. In the extreme case, a completely vertical fiber will be assigned the color white.

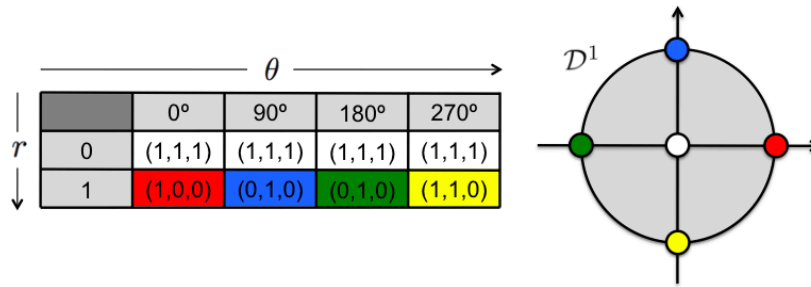


Figure 5.5: Coloring criteria. On the left a table that assigns (R,G,B) colors to 5 keypoints on the disk that are given in polar coordinates. Notice that for $r = 0$ all points coincide with the center of the disk. On the right, the location of these points inside the disk.

This provides a continuous colormap all over \mathcal{D}^1 . However, since it is difficult for the human eye to distinguish a continuous gradient of color, we discretize the disk in regions corresponding to a uniform partition of the orientation and the elevation angles. The θ -direction is divided into N_θ sectors (indexed by $i = 1, \dots, N_\theta$) and the r -direction is divided into N_r layers (indexed by $j = 1, \dots, N_r$). We have chosen $N_\theta = 8$ and $N_r = 3$, which leads to 8×3 regions. In this case, the first layer comprises fibers with an elevation angle between 0° and 30° . The following two layers comprise fibers with an elevation angle between 30° and 60° , and between 60° and 90° respectively. Figure 5.6 (a) shows the colormap in our case. Notice that a uniform partition of the elevation angle leads to a non-uniform partition of partition of \mathcal{D}^1 along r -direction. This is due to the relation $r = \cos(\varphi)$ (see Fig. 5.6 (b)).

For any $\mathbf{x} \in \mathcal{LV}$, a color in this colormap is assigned to its associated myocardial fiber $V(\mathbf{x})$ computing the correspondent index as follows:

$$\begin{aligned}
 i(\mathbf{x}) &= \text{round} \left(\text{mod} \left(\frac{N_\theta \theta(\hat{\xi})}{2\pi}, N_\theta \right) + 1 \right) \\
 j(\mathbf{x}) &= N_r - \text{floor} \left(\frac{2N_r \arccos(r(\hat{\xi}))}{\pi} \right) + 1
 \end{aligned} \tag{5.20}$$

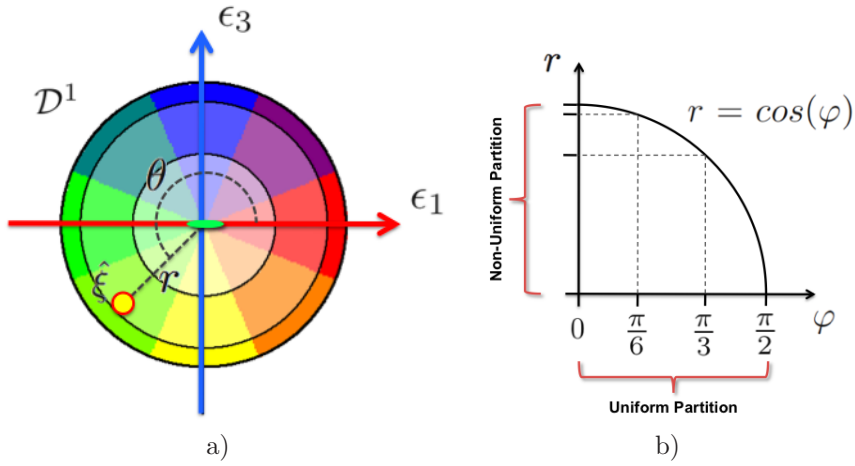


Figure 5.6: a) Discrete colormap using 8×3 regions. b) Relation between the uniform partition of the elevation angle and the non-uniform partition of the r -direction.

5.4 Experiments

DTI volumes used in this thesis were acquired and processed by Drs. Patrick A. Helm and Raimond L. Winslow at the Center for Cardiovascular Bioinformatics and Modeling and Dr. Elliot McVeigh at the National Institute of Health; and downloaded from the Center for Cardiovascular Biomechanics and Modelling¹. They belong to 8 normal canine hearts. For the acquisition process, each heart was placed in an acrylic container filled with Fomblin (Ausimon, Thorofare, NJ), and a 3D fast spin-echo (3D-FSE) sequence was used to acquire diffusion images. MR parameters varied slightly depending on heart size. The field of view ranged from 8 to 10 *cm* yielding image in-plane resolutions of 312.2×312.2 to $390 \times 390 \mu\text{m}^2$. The volume was imaged with 110 to 120 slices at 800- to 1000- μm thickness. Diffusion gradients were applied in a minimum of sixteen noncollinear directions with a maximum diffusion weighting of 1500 s/mm^2 .

¹<http://www.ccbm.jhu.edu/index.php>

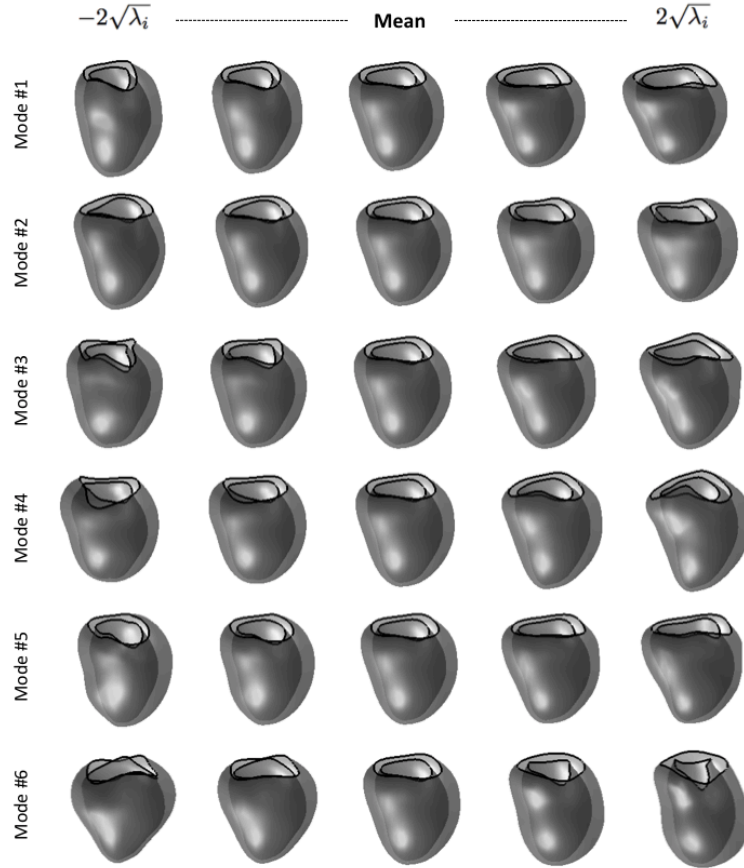


Figure 5.7: By rows, the 6 principal modes of variation obtained moving parameter b_n up to ± 2 standard deviations from the mean, shown in the central column.

5.4.1 Anatomic Atlas

We have addressed the creation of an anatomic atlas jointly modelling the gross anatomy and the fiber architecture of the LV using the 8 normal canine hearts.

The gross anatomy has been obtained parameterizing the geometric volume of each canine heart as described in Section 4.3.2. For each heart, the control points of the parametrization map have been concatenated (eq. 5.2) and their mean and covariance matrix have been obtained (eqs. 5.3 and 5.4 resp.). In order to properly describe the variability observed in the 8 canine hearts, the 6 first modes of variation (which explain a 99.25% of the total shape variability) have been taken into account. Figure 5.7 shows the 6 modes of variation, $\{\phi_n\}_{n=1}^6$, for the gross anatomy. Each mode (shown in rows) is computed by setting to zero all coefficients in equation 5.7 but the one associated to the mode ϕ_n , b_n . This coefficient is uniformly sampled in

the range $\pm 2\sqrt{\lambda_n}$ (for $\sqrt{\lambda_n}$ the standard deviation associated to ϕ_n). In this manner the first column corresponds to -2 standard deviations and the last to 2 standard deviations from the average anatomy, shown in the central column.

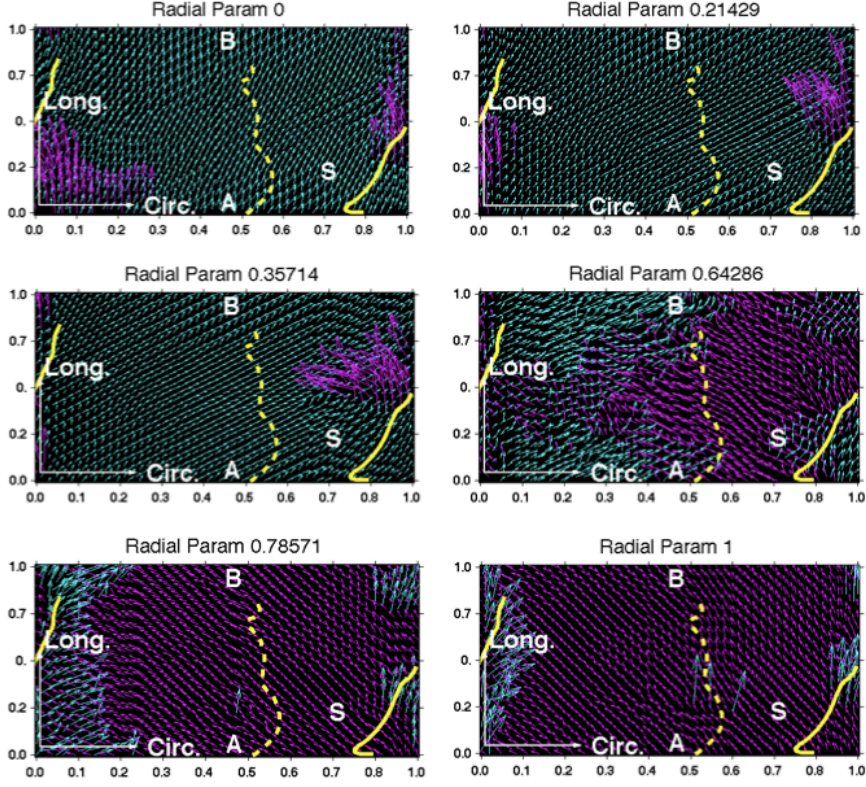


Figure 5.8: Average fiber distribution in Ω^3 for 6 slices of constant radial parameter $w = \{0, 0.21, 0.35, 0.64, 0.78, 1\}$, for $w = 0$ the endocardium and $w = 1$ the epicardium. The yellow lines represent the junction between right and left ventricles at anterior (continuous line) and posterior (dashed line) walls. Apical area is labelled 'A', basal 'B' and septal 'S'.

For modelling the fiber architecture, the same parametrization obtained for the geometric volumes, could be used for their respective first eigenvector component volumes (they share the same coordinates). Using the parametric map, the components of the vectors representing fiber directions were moved to Ω^3 (Sec. 4.1.1), normalized (eq. 5.9) and reoriented (eq. 5.10). To each point in Ω^3 , statistical analysis, using the Frechet mean (see Sec. 5.2.1) was applied to the 8 vectors (lying on S^{2+}). In order to compensate for the low number of DTI studies, in the case of fibers, we increased the number of samples by considering vectors in a 4-connected neighborhood defined in the circumferential-longitudinal plane (of Ω^3). This strategy allowed to increase up to 5 times the number of samples for computing the statistics, while

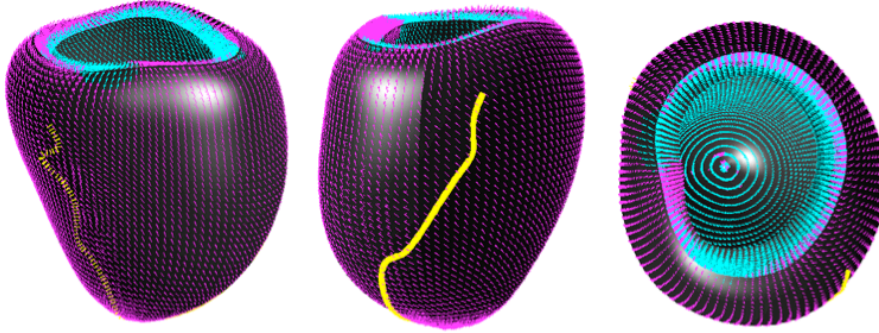


Figure 5.9: Average fiber architecture over the average gross anatomy of the \mathcal{LV} . The colors (cyan and magenta) are in concordance with those in Fig. 5.8.

avoiding to mix fiber orientations between different radial layers (where gradients of fiber variations are higher). The average model of the myocardial fibers is shown in Figure 5.8 where their orientation is visualized in Ω^3 considering different slices for fixed radial parameters, $w = \{0, 0.21, 0.35, 0.64, 0.78, 1\}$ ($w = 0$ the endocardium and $w = 1$ the epicardium). Images are given in the circumferential and longitudinal directions of Ω^3 . The yellow lines represent the junction between right and left ventricles at anterior (continuous line) and posterior (dashed line) walls. Apical area is labelled 'A', basal 'B' and septal 'S'. We can observe that endocardial and epicardial cuts present an approximate uniform fiber orientation with opposite sign with respect to the circumferential direction (each orientation is colored by cyan and magenta). We observe that as the radial parameter evolves from 0 to 1 (endocardium to epicardium), the orientation of fibers suffer from an abrupt change in orientation. Notice that this change starts at septal area and gradually propagates to rest of the tissue.

The joined model of the gross anatomy and the fiber architecture is obtained by mapping the fiber average model to the average geometry. This is achieved by applying the Differential of the average parametrization to the mean fibers computed in Ω^3 . Figure 5.9 shows the average fibers over the average gross anatomy. The colors (cyan and magenta) are in concordance with those in Fig. 5.8 and the yellow curves stand for the RV-LV junctions at anterior wall (continuous) and inferior wall (discontinuous).

In order to visualize the disposition of myocardial fibers inside the LV, we have performed a tractography process over the joined average model (using the MATLAB `streamline` function). Figure 5.10 shows several views of the final result where we can appreciate 3 sets of fibers colored red, green and blue. Blue fibers have been generated using seeds uniformly placed in the epicardium ($w = 1$), whereas green and red fibers have been obtained using seed uniformly distributed in the midwall ($w = 0.5$) and in the endocardium ($w = 0$) respectively. In Figure 5.11 it can be appreciated that these fibers visually correlate to the structure of the HMVB.

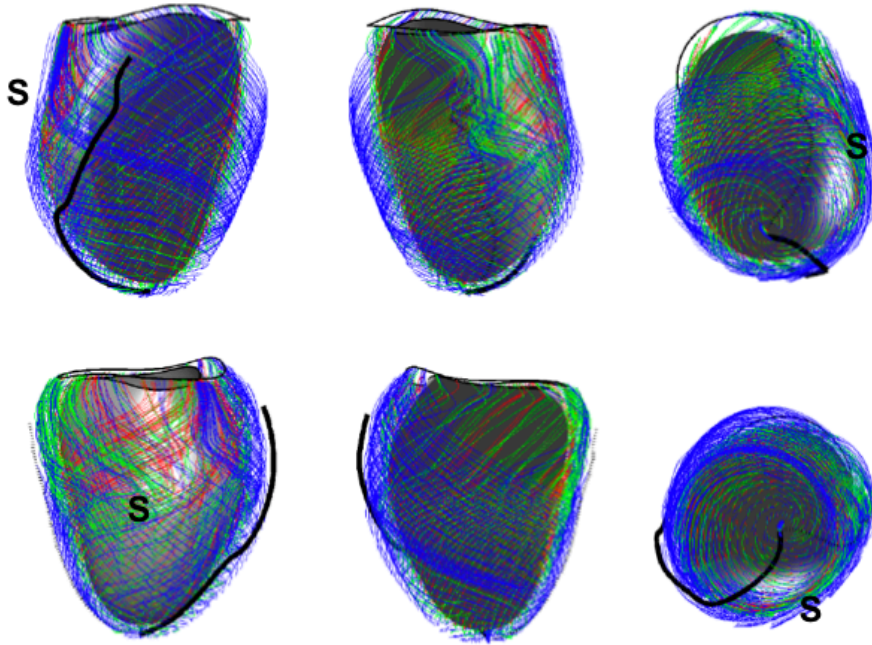


Figure 5.10: Tractography performed onto the average fiber architecture mapped to the mean LV gross anatomy. Blue fibers have been generated using seeds placed in the epicardium ($w = 1$), whereas green and red fibers have been obtained using seed placed in the midwall ($w = 0.5$) and in the endocardium ($w = 0$) respectively. S indicates the septal wall and the bold black line, the junction between RV and LV at anterior wall.

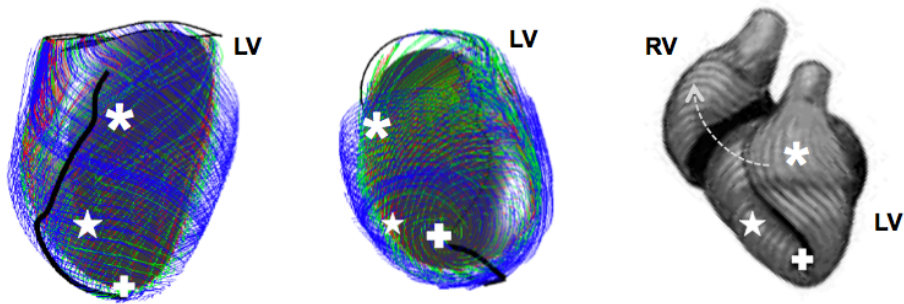


Figure 5.11: Correspondences observed between the fibers obtained performing tractography on our average model (first two images) and those in a schematic visualization of the HMVB, where the RV have been uncoupled from the LV (last image). Equivalent anatomical areas are marked with th same symbol in all images.

5.4.2 Evidences Supporting the HMVB

As discussed in Subsection 2.3.2 the HVMB has been rejected by some on the basis of histological- [9, 10], optical- [95] and DTI-based [173] evidences of a smooth change in ventricular fibre orientation across the myocardium. There are, however, other evidences pointing that the HVMB might follow a favored path as suggested by several authors from histological [89] and optical [126] studies. Figure 5.12 (a-d) (proposed in [69]) synthesizes fibre angle change, obtained from DTI, with the dissection diagrams of [89] (Fig. 5.12 (e,f)) and optical section reconstructions of [126] (Fig. 5.12 (g)). Divergences above 6° are shown in black for two basal levels (a,b), mid-heart (c) and 4 chambers (d). Major transitions are highlighted in red. Both, DTI sections (Fig. 5.12 (a-d)) and the optical reconstruction (Fig. 5.12 (g)) split the ventricles into zones that suggest the HVMB dissection planes. DTI-derived cross-sections show V-shaped features correlating to the pinnation features (Fig. 5.12 (e,f)) described in [89]. If a dissection plane is made joining these features this reproduces a key feature of the HVMB dissection path. This evidence does not identify the HVMB as a unique unit but it does show that the dissection of Torrent-Guasp follows a measurable difference within the myocardium.

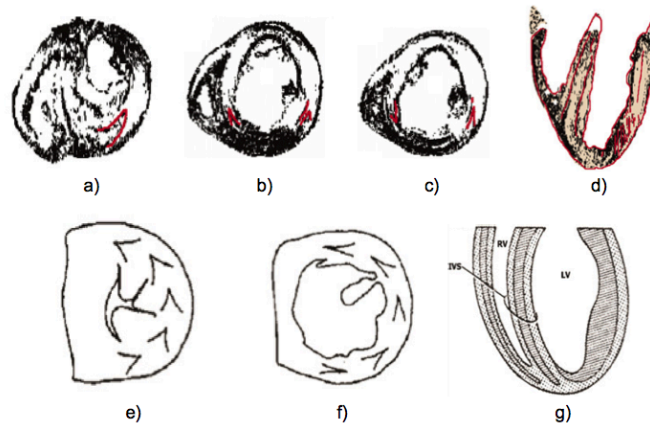


Figure 5.12: Synthesis of maps of fibre orientation obtained from DTI with ventricular architecture from histology (a-d). Canine histological pinnation patterns observed in [89] at systole (e) and diastole (f). Longitudinal reconstruction of murine optical mapped fibre angle obtained in [126] (g).

We have applied the coloring method described in Section 5.3 to the 8 parameterized canine hearts, as well as, to the mean model (computed in Section 5.4.1). Visual assessment of the results (shown in Fig. 5.13 for the 3 subjects and the mean model) confirm the above observations. In all cases they show two main populations (red, green) of fibers oppositely oriented and almost concentric. Their boundary clearly enhances the dissection path suggested above and supports HMVB unfolding process.

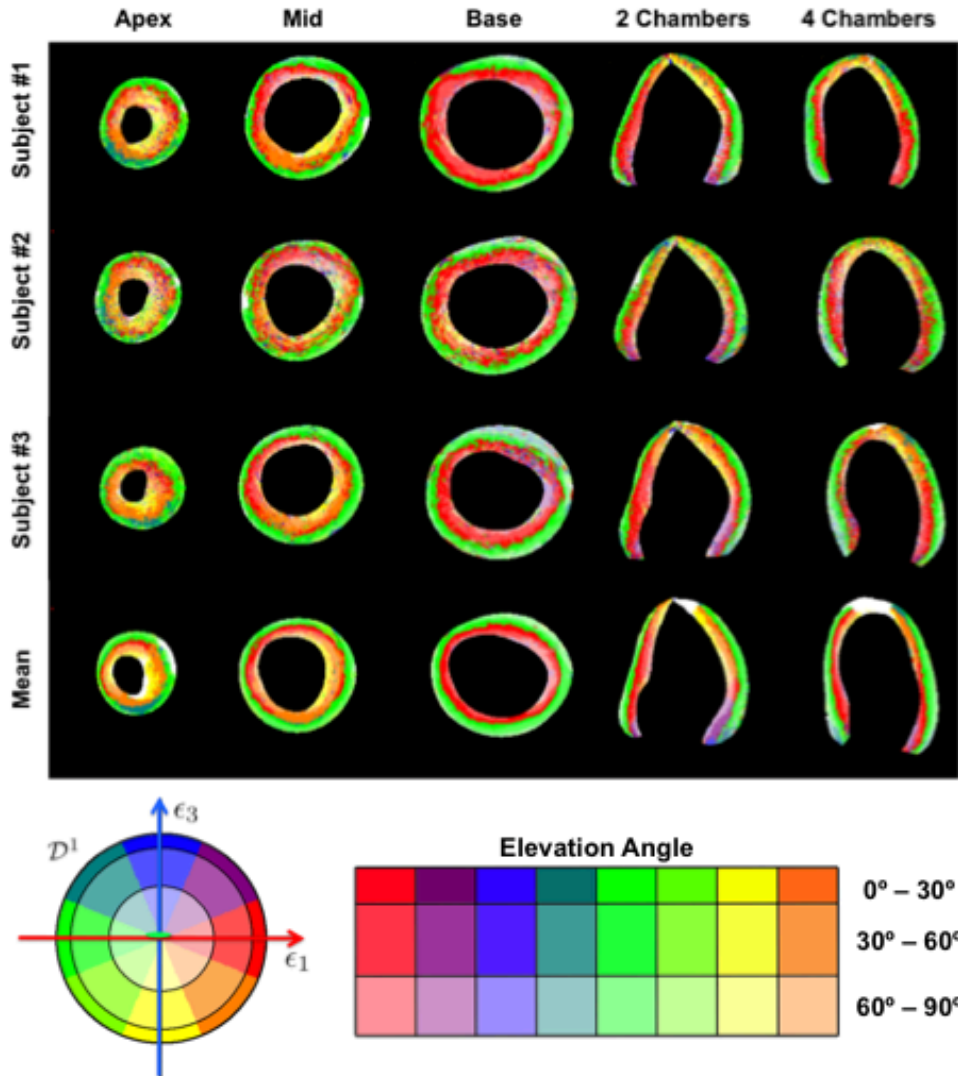


Figure 5.13: Coloring method applied to 3 canine hearts and to the mean model. Transition between red-most and green-most areas (which contain fibers running oppositely) clearly show the HMVB dissection path. Below on the left the legend codifying the orientation of the fiber according to the local references is depicted. On the right, the legend depicts the elevation angle according to the tone of the color.

5.5 Discussion

The NPD framework has been applied to build a joined atlas of the LV including both, the gross anatomy and its fiber architecture from 8 DTI normal canine hearts. From the B-Spline based parameterization maps, that have a vector space structure,

we have created a PDM describing the gross anatomy observed in the data set. Dimensionality reduction have been performed and the first 6 modes of variation taken into account (99.25% of total variation). Myocardial fibers have been statistically analyzed in Ω^3 where Riemmanian metrics were required. The NPD allowed to perform an oversampling according to the LV geometry in order to account for the low number of subjects. A straightforward visualization of the average fiber distribution evidenced the presence of two populations presenting opposite orientations (as in [81]). In addition, the tractography process suggests that our mean fiber model visually correlate to the HMVB structure.

The formulation of NPD framework have allowed to easily map the average model of fiber architecture to the average geometry. But this mapping can be extended to other geometries of any subject (even alive) previously parameterized. Thus, the NPD framework might contribute to the creation of patient-sensitive LV electromechanical models.

Since the NPD framework endows the LV with anatomically meaningful local coordinates, we have designed an enhanced visualization method of the fiber architecture. The method consists on designing a colormap that assigns an (R,G,B) tuple to each fiber according to its position relative to the local references. Thus, the colormap inherits the anatomic interpretation from these references, providing an intuitive visualization of the fiber structure. In fact, this coloring method allows to observe that the myocardial fibers run oppositely in two concentric rings. The discontinuity between both rings is interpreted as that the HMVB dissection process follows an anatomic feature inside the LV. This evidence supports that HMVB might be systematically unfolded.

Chapter 6

Function Modelling

The characterization of LV function requires, both, the definition of indicators characterizing the myocardial function (for any patient in a reproducible manner) and the creation of a statistical model (normality patterns) able to discriminate healthy from diseased areas. In this Chapter we obtain normality patterns for global and local function scores. Regarding global ones, due to their increasing clinical relevance [79] we consider ventricular rotation at base, mid and apex, in addition to ventricular torsion (or twist). Regarding local scores we consider motion vector fields obtained by means of HPF, as well as, several strains. We also fuse local scores to obtain multidimensional descriptors of local function. In order to determine the optimal set of indicators able to localize Regional Wall Motion Abnormalities (RWMA), we thoroughly explore the feature space given by all local descriptors.

6.1 Function Descriptors

6.1.1 Global Descriptors

Rotation

The rotation at a given LV point at time t is defined as the angle between its position at end-diastole ($\mathbf{x}^0 \in \mathcal{LV}^0$) and its current position at time t ($\mathbf{x}^t \in \mathcal{LV}^t$) with respect to the axis of rotation (the main axis of the LV). Since in the case of SA views this axis can not be identified, we approximate it as the center of the blood pool at time t , which is computed as the centroid of the endocardial points. It will be noted as O^t . Components of \mathbf{x}^t are obtained by applying HPF-based tracking to its position at end-diastole:

$$\mathbf{x}^t = \begin{cases} \mathbf{x}^0 & t = 0 \\ \mathbf{x}^t = \mathbf{x}^{t-1} + V^{t-1}(\mathbf{x}^{t-1}), & t > 0 \end{cases} \quad (6.1)$$

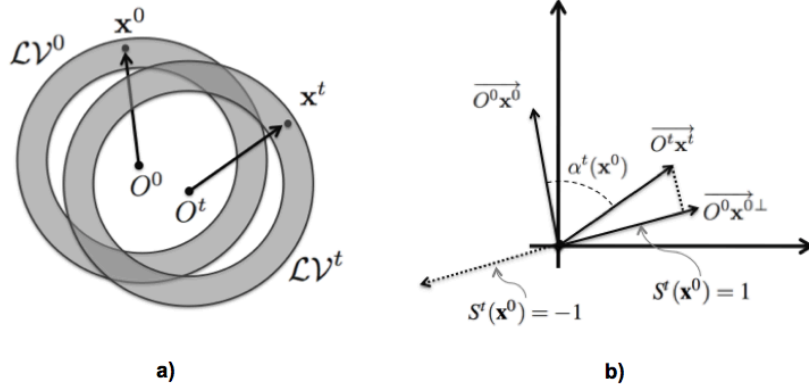


Figure 6.1: Rotation computation. a) A point \mathbf{x}^0 at end-diastole (\mathcal{LV}^0) and its spatial position at time t , \mathbf{x}^t , generate two vectors considering the centroids O^0 and O^t . b) The angle of these vectors multiplied by the sign function ($S^t(\mathbf{x}^0)$), is the rotation experienced by \mathbf{x}^0 at time t .

The angle between 2 points, \mathbf{x}^0 , \mathbf{x}^t is defined by the scalar product of the vectors $\overrightarrow{O^0\mathbf{x}^0}$ and $\overrightarrow{O^t\mathbf{x}^t}$:

$$\alpha^t(\mathbf{x}^0) = \frac{180}{\pi} \arccos \left(\frac{\langle \overrightarrow{O^0\mathbf{x}^0}, \overrightarrow{O^t\mathbf{x}^t} \rangle}{\| \overrightarrow{O^0\mathbf{x}^0} \| \| \overrightarrow{O^t\mathbf{x}^t} \|} \right) \quad (6.2)$$

Since the arccos function does not provide any sign, equation 6.2 is multiplied by the following function that provides an orientation for the rotation:

$$S^t(\mathbf{x}^0) = \text{sign} \left(\langle \overrightarrow{O^0\mathbf{x}^0_{\perp}}, \overrightarrow{O^t\mathbf{x}^t} \rangle \right)$$

Then, the rotation experienced by a point \mathbf{x}^0 at time t is given by

$$r^t(\mathbf{x}^0) = S^t(\mathbf{x}^0) \alpha^t(\mathbf{x}^0) \quad (6.3)$$

The scheme in Figure 6.1 sketches the computation of the angle of rotation.

Finally, the rotation of the whole LV at time t is defined as the average angle of rotation for a uniformly sampling of \mathcal{LV}^0 :

$$R^t = \frac{1}{N} \sum_{n=1}^N r^t(\mathbf{x}_n^0) \quad \mathbf{x}_n^0 \in \mathcal{LV}^0 \quad (6.4)$$

Torsion

Ventricular torsion is defined as the difference between rotation angles measured at 2 different SA levels. In clinical practice such levels are often defined for the most apical level in which blood pool is still visible and a basal one just above the papillary muscles. We will denote torsion as T^t , for t indicating time as usual.

6.1.2 Local Descriptors

Following [165], in order to assess myocardial local function, we consider two different kinds of local indicators (or attributes): *0th*-order (motion) and *1st*-order (strains). Since their comparison and fusion takes place in the NPD, all attributes are considered at the points $\mathbf{x} = \Psi^t(u, w)$, $(u, w) \in \Omega^2$.

0th-order Indicators (Motion)

Motion is given by the (two) components, (V_x^t, V_y^t) , of the vector fields V^t expressed in image coordinates. Our *0th*-order attributes are given by the circumferential (V_u^t) and radial (V_w^t) components of the motion vectors V^t . This is, V^t expressed in terms of the local references $\{e_u, e_w\}$ given by equation (4.3).

1st-order Indicators (Strains)

They are given by the spatial variations (1st partial derivatives) of the displacement maps and are computed by means of the strain tensor:

$$E(V) = \frac{1}{2} (\nabla V + \nabla V^T + \nabla V^T \nabla V) \quad (6.5)$$

where

$$\nabla V = \begin{pmatrix} \partial_x V_x & \partial_y V_x \\ \partial_x V_y & \partial_y V_y \end{pmatrix} \quad (6.6)$$

and T denotes the transpose of a vector or matrix. The strain at a point \mathbf{x} along a direction v (with $\|v\| = 1$) is given by:

$$S_v(\mathbf{x}) = v^T E(V(\mathbf{x}))v \quad (6.7)$$

Strains describe the amount of contraction the muscle undergoes. In cardiac function analysis, the usual strains are extremal (minimal, S_m , and maximal, S_M) strains and directional strains. The latter are commonly computed along radial (S_R) and circumferential (S_C) directions. In addition, we also consider the strain along the direction

of displacement (S_D). Extremal strains are given by the highest (S_M) and the lowest (S_m) eigenvalues of the strain tensor evaluated in the NPD, $E(V(\mathbf{x}))$. Directional strains are given by:

$$\begin{aligned} S_C(\mathbf{x}) &= (e_u(\mathbf{x}))^T E(V(\mathbf{x})) e_u(\mathbf{x}) \\ S_R(\mathbf{x}) &= (e_w(\mathbf{x}))^T E(V(\mathbf{x})) e_w(\mathbf{x}) \\ S_D(\mathbf{x}) &= \frac{V(\mathbf{x})^T}{\|V(\mathbf{x})\|} E(V(\mathbf{x})) \frac{V(\mathbf{x})}{\|V(\mathbf{x})\|} \end{aligned} \quad (6.8)$$

for e_u, e_w the local references (eq. (4.3)).

6.1.3 Multivariate Regional Function Descriptors

Usually *0th* and *1st*-order attributes are considered separately. However, on one hand strains reflect muscle contraction at an image plane. On the other hand, since tissue motion follow from adjacent contracting fibers (dragging effect), motion might reflect the dynamic behavior of areas even outside the image plane. We, thus, consider that by taking into account both attributes, better descriptors reflecting (in spite of being 2D) the 3D functionality of the LV should be obtained. Merging all the attributes described so far, we obtain a 9-dimensional feature space describing more faithfully the local function of the LV.

$$\Gamma^t(\mathbf{x}) = [V_u^t(\mathbf{x}), V_w^t(\mathbf{x}), S_C^t(\mathbf{x}), S_R^t(\mathbf{x}), S_D^t(\mathbf{x}), S_M^t(\mathbf{x}), S_m^t(\mathbf{x})] \quad (6.9)$$

We will use the above multidimensional descriptor to assess the regional behavior of LV function.

Regions in the LV are defined by giving a uniform grid on Ω^2 . A sampling given by

$$u_I = \{(I-1)/N_S\}_{I=1}^{N_S} \quad w_J = \{(J-1)/N_L\}_{J=1}^{N_L}$$

divides Ω^2 in $N_S \times N_L$ regions ω_{IJ} :

$$\omega_{IJ} = \{(u, w) \in \Omega^2 / u_I \leq u \leq u_{I+1}, w_J \leq w \leq w_{J+1}\} \quad I = 1 \div N_S, \quad J = 1 \div N_L \quad (6.10)$$

Regions along the circumferential direction (u) are called sectors whereas along the radial direction (w) layers. The functional score at each ω_{IJ} for a given systolic time t is given by the average:

$$\Gamma_{IJ}^t := \frac{1}{N_u N_w} \sum_{i=1}^{N_u} \sum_{j=1}^{N_w} \Gamma^t(\Psi^t(u_i, w_j)) \quad (u_i, w_j) \in \omega_{IJ}$$

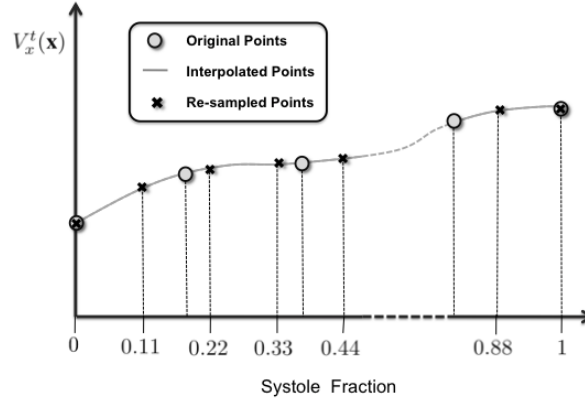


Figure 6.2: Temporal normalization the component of the motion field V_x .

for (u_i, w_j) a uniform sampling over ω_{IJ} .

6.2 Time and Space Normalization

In order to obtain quantities comparable across different studies, spatio-temporal variability across acquisitions should be compensated. On one hand, TMR studies may have different spatial resolution. On the other hand, due to heart beat variability, the number of frames per cardiac cycle may differ from one study to another.

Space Normalization

Since TMR studies may have different spatial resolution (depending on the acquisition conditions), the displacement vector fields in pixels are non-comparable. This artifact is removed by considering motion fields in mm. Millimeter resolution is achieved by resizing images so that 1 pixel corresponds to 1 mm^2 . The spatial resolution may be found in the DICOM header associated to images.

Time Normalization

Temporal resolution is compensated by interpolating the motion components V_x^t and V_y^t in order to get a uniform sampling along the systolic cycle for all subjects. Let us consider the discrete sets $\{V_x^t(\mathbf{x})\}_{t=0}^{T_{ES_n}}$ and $\{V_y^t(\mathbf{x})\}_{t=0}^{T_{ES_n}}$. The components at time $t = 0$ correspond to 0% of systolic cycle, whereas components at time $t = T_{ES_n}$ correspond to 100% of systole. We re-sample values (by using cubic interpolation) at N_T uniformly sampled fractions of the systolic cycle given by $t = \{kT_{ES_n}/N_T\}_{k=0}^{N_T}$.

Figure 6.2 shows the re-sampling process of the x component V_x^t at a given point

x. The x -axis represents the fraction of systolic cycle. The components obtained from analysis of TMR sequences, $\{V_x^t(\mathbf{x})\}_{t=0}^{T_{ES_n}^t}$, are plotted in circles. The values at the uniform sampling of the systolic cycle are plotted in crosses over the interpolated curve in solid line.

6.3 LV Functional Assessment

6.3.1 Normality Patterns

Normality patterns of global (time-evolving) scalar scores are computed by considering the rank for each systolic phase. For a given systolic phase, the rank is given by the average \pm the standard deviation computed from N healthy subjects. For rotation is obtained as follows

$$\mu_R^t = \frac{1}{N} \sum_{n=1}^N R_n^t \quad \sigma_R^t = \sqrt{\frac{1}{N} \sum_{n=1}^N (R_n^t - \mu_R^t)^2} \quad t = 0 \div 100(\%) \quad (6.11)$$

whereas for torsion is computed as

$$\mu_T^t = \frac{1}{N} \sum_{n=1}^N T_n^t \quad \sigma_T^t = \sqrt{\frac{1}{N} \sum_{n=1}^N (T_n^t - \mu_T^t)^2} \quad t = 0 \div 100(\%) \quad (6.12)$$

6.3.2 Regional Function Assessment

Regional normality models follow from the statistical analysis of the descriptors $\{\Gamma_{IJ}^t\}_{t=1}^{N_T}$ obtained for healthy volunteers. We assume gaussianity and describe the regional normal function of the LV with $N_L \times N_S \times N_T$ gaussian models (one for each spatiotemporal region). Principal component analysis serves to obtain the orthogonal basis that best explains the correlations among functional parameters. The eigenvectors of the covariance matrix of the observations give the modes of variation and the eigenvalues the expected normal ranges.

Let μ_{IJ}^t , Σ_{IJ}^t be, respectively, the mean and covariance matrix of Γ_{IJ}^t for the N healthy cases. Given an incoming subject, the Mahalanobis distance:

$$dM_{IJ}^t = \sqrt{(\Gamma_{IJ}^t - \mu_{IJ}^t)^T (\Sigma_{IJ}^t)^{-1} (\Gamma_{IJ}^t - \mu_{IJ}^t)}$$

quantifies the deviation of the subject regional descriptor Γ_{IJ}^t from the average healthy model. The average of dM_{IJ}^t for all times:

Table 6.1: Visualization of Regional Function Assessment.

Function Value	Label	Color
$D_{IJ} < Th$	'Normal'	$R = 0; G = \frac{e^{-D_{IJ}/2} - e^{-1}}{1 - e^{-1}}; B = 0$
$D_{IJ} > Th$	'Abnormal'	$R = \frac{e^{-1} - e^{-D_{IJ}/2}}{e^{-1}}; G = 0; B = 0$

$$D_{IJ} = \frac{1}{N_T} \sum_{t=1}^{N_T} dM_{IJ}^t \quad (6.13)$$

gives a compact description of the region (ω_{IJ}) integrity. Regions are considered 'Abnormal' if D_{IJ} is over a given threshold Th and 'Normal' otherwise. The threshold value was set using ROC analysis as detailed in Section 6.4.2.

In order to provide an intuitive visual assessment of the different regions, each of them will be assigned a color according to its classification: green is used for 'Normal' regions and red for 'Abnormal' ones. In order to obtain a more descriptive assessment, the red (R) and green (G) channels are colored according to Table 6.1. In this manner, dark colors indicate (for, both, 'Normal' and 'Abnormal') values close to the boundary discriminating pathological behaviors from normal ones. Meanwhile, bright tones correspond to extreme behaviors: severe deviation from normality for the red color and high agreement to normal function for the green one.

6.3.3 Parametric Images

For an intuitive visualization of data over the LV, we use Bull's Eye Plots (BEPs). BEPs are polar plots that represent an idealized LV. The most extended BEP is the standardized 17-segment division suggested by the AHA [36]. AHA BEP plots 4 SA levels (basal, mid, apical and the apical cap) in the same graphic formed by 4 concentric rings. Many authors, however, have developed their own BEPs [23, 42, 139, 25, 189]. In our case we use a separate BEP for each of the 3 SA levels, basal, mid and apex (leaving aside the apical cap). For each BEP, the outer rim denotes the epicardium and the inner rim denotes the endocardium. The BEPs are enhanced with an arc representing the septal portion (displayed on the left) and for a better comparison to AHA segments, these are included in the outer rim (labels are: A standing for *Anterior*, AL for *Antero-Lateral*, IL for *Infero-Lateral*, I for *Inferior*, IS for *Infero-Septal* and AS for *Antero-Septal*). In the case of showing continuous data over the LV, our BEP is flat inside, whereas in the case of showing data obtained in regions, the BEP is divided into sectors and layers. Figure 6.3 shows our BEP (either continuous and discrete) in relation to their location in the LV and to the standard AHA BEP.

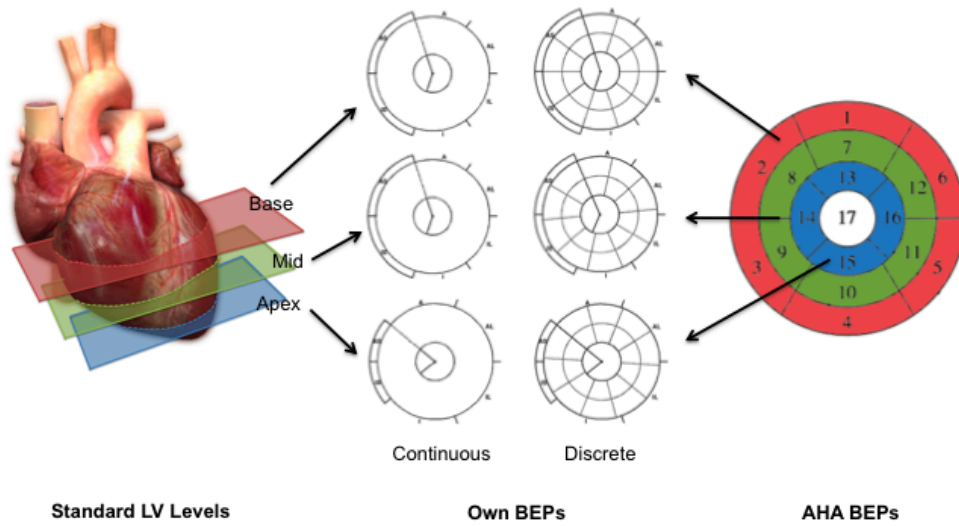


Figure 6.3: Relation between our BEPs (shown in the center for, both, continuous and discrete cases) and the standard AHA BEP (shown in the right).

6.4 Experiments

Our data set consists of healthy volunteers and patients with several degrees of hypokinesia:

- *Healthy subjects.* Composed of a total number of 21 volunteers, 15 males and 6 females aged between 23 and 55 (30.7 ± 7.5).
- *Non-healthy subjects.* Composed of a total number of 7 patients (6 infarcted and 1 hypertrophic), 4 males and 3 females aged between 47 and 71 (60 ± 8).

Image acquisition details are those given in Section 3.4.2.

6.4.1 Normality Patterns

Global Scores

Normality patterns of rotation and torsion have been computed using equations 6.11 and 6.12 for the healthy population. The normality patterns for rotation and torsion are plotted in Fig. 6.4. The horizontal axis shows the percentage of the systolic cycle and the vertical one the rotation and torsion in degrees. In the case of the torsion we show (in bright gray lines) its variability range given by the standard deviation of the 21 patterns considered. The average plots for rotation show that all three

Table 6.2: Mean values and their standard deviation for basal (B), mid (M) and apical (A) levels. Torsion (T) is also showed. Values are given for 6 stages of the systolic cycle.

	17%	33%	50%	67%	83%	100%
B	0.7 ± 0.2	0.6 ± 0.5	-0.7 ± 0.8	-2.3 ± 1.0	-3.3 ± 1.0	-3.2 ± 1
M	1.3 ± 0.3	2.5 ± 0.4	2.2 ± 0.7	1.5 ± 0.9	1.4 ± 0.9	2.7 ± 1.6
A	1.5 ± 0.3	2.8 ± 0.7	3.3 ± 1	3.6 ± 1.3	4.6 ± 1.5	7.4 ± 2
T	0.7 ± 0.4	2.2 ± 0.7	4.1 ± 1	6 ± 1.4	7.8 ± 1.7	10.7 ± 1.8

levels start rotating counterclockwise (seen from apex to base) and at 23% and 38% of the cycle, base and mid change to clockwise rotation respectively. At these points they reached a rotation of 0.85° and 2.63° . Later, at 92% and 78% (-3.48° , 1.37°) base and mid, turn again to counterclockwise rotation until reaching the end of the systolic cycle (-3.2° , 2.7°). On the other hand, apex experiments a non-decreasing rotation (counterclockwise) during all the systolic cycle. In its central interval, from 45% to 64% approximately, rotation remains almost constant as it varies from 3.3° to 3.5° . This fact means that, in this period of time, radial shortening predominates over rotation. It is worth to mention that, despite the nonlinear rotational behavior that all levels undergo, the resultant torsion values vary almost linearly with time. In Table 6.2 we show the numeric range at some representative systolic stages. Statistical ranges are given by the mean plus minus the standard deviation of the subjects analyzed.

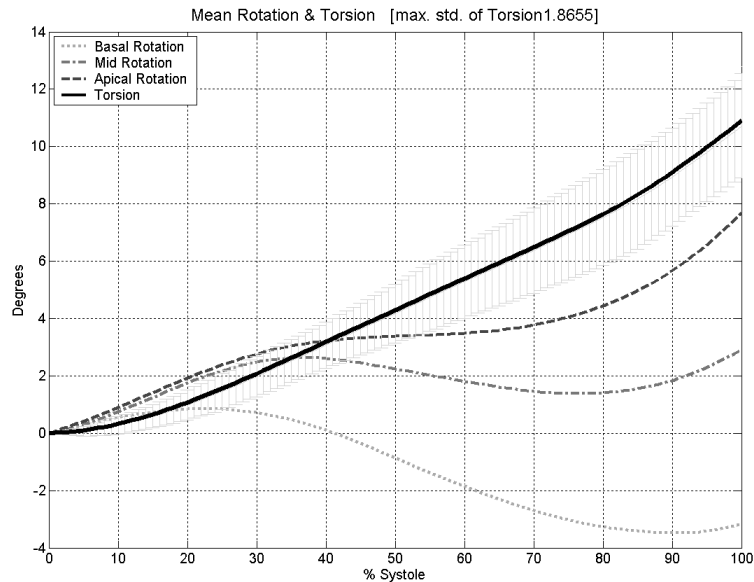


Figure 6.4: Normality Patterns for basal, mid and apical rotation and torsion.

Table 6.3: Parameter configurations used in our experiments

\mathcal{C}	V_u	V_w	S_C	S_R	S_D	S_M	S_m	Dim
1	•	•	–	–	–	–	–	2
2	–	–	•	•	–	–	–	2
3	–	–	–	–	–	•	•	2
4	•	•	–	–	•	–	–	4
5	•	•	•	•	–	–	–	4
6	•	•	–	–	–	•	•	4
7	•	•	•	•	•	–	–	5
8	•	•	–	–	•	•	•	5
9	•	•	•	•	•	•	•	7

Local Scores

Normality patterns of *0th*- and *1st*-order attributes have been computed for the healthy population at basal, mid and apical levels and setting $N_T = 9$.

Figures 6.8, 6.9 and 6.10, show in our continuous BEP the normality patterns (just the mean) of motion for base, mid and apex respectively. In each BEP, the arrows indicate the direction of displacement at a particular stage of the systolic cycle. The underlying colormap indicates the magnitude of the displacement measured in millimeters and the range is specified in the colorbar beside each chart. In contrast to the global patterns, local ones allow a detailed visualization of tissue behavior along the systolic cycle. In Figure 6.8, we can appreciate that, at basal level, *A* and *Al* segments start a moderate contraction while the rest of segments present a counterclockwise rotation. Rapidly, *IL* and *I* segments change the orientation of their rotation. From 44.4% on, all segments rotate clockwise with the *A* segment also suffering some contraction. Figure 6.9 shows that for the mid level all segments start rotating counterclockwise. 33.3% of the systolic cycle represents an inflexion point. All sectors contract and then they turn to clockwise rotation until the end of the systolic cycle. Concerning apical level, Figure 6.10 reveals that at the beginning of systole all sectors experience a counterclockwise rotation except *I*. At 11.1% of the systolic cycle, sectors *I* and *IL* start a strong contraction followed by *IS* at 33.3%. From this stage on, *I* and *IL* keep on contracting while *AL* and *A* rotate counterclockwise and *IS* and *AS* clockwise.

Average patterns of circumferential, radial and extremal strains are shown for the three levels from Figures 6.11 to 6.22. Colormap indicates the percentage of deformation (in %) and the darker bold level curves indicate the transition from positive to negative values (zero crossing).

6.4.2 Optimal Configuration for RWMA Assessment

The NPD framework has been applied to assess the regional systolic function in TMR sequences. For each sequence, $N_L \times N_S \times N_T = 2 \times 10 \times 9$ spatio-temporal regions

have been considered. The 7-dimensional feature space defined in equation (6.9) is explored in order to determine which subsets of parameters are best suited for regional assessment of LV function. Among the 127 possible configurations, we have analyzed 9 representative subsets ($\mathcal{C}_i, i = 1, \dots, 9$) given in table 6.3. The bullet indicates that a particular attribute is present in the configuration.

For each configuration we have assessed:

- *Model Consistency.* We consider that for healthy cases all regions should be labelled as '*Normal*'. Consistency is assessed by Leave-One-Out (LOO) errors for the volunteers data set.
- *Pathology Discrimination.* The clinical potential is given by the ability for detecting anomalous regional behaviors. Discrimination is assessed by comparing the automatic classification to manual labelling.

Ground Truth Maps

For each sequence we define its ground truth as a discrete BEP with each of its $N_L \times N_S$ regions labelled as '*Normal*' or '*Abnormal*' (BEPs labelled *Expert*#1 and *Expert*#2 in fig. 6.7). Physicians were asked to visually identify those regions moving abnormally. The experts were given two TMR sequences: the original one and another with the $N_L \times N_S$ time-evolving regions printed over \mathcal{LV}^t . A region was labelled '*Abnormal*' if it presented any anomalous behavior along the systolic cycle. Two different experts have been considered in order to compute inter-observer variability.

Quality Scores

The performance of each configuration was evaluated in terms of sensitivity and specificity given by:

$$spec = \frac{T_N}{N}, \quad sens = \frac{T_P}{P} \quad (6.14)$$

for T_P true positives (number of regions correctly classified as '*Abnormal*') and T_N true negatives (number of regions correctly classified as '*Normal*'). The total number of '*Abnormal*' (positive) and '*Normal*' (negative) regions are P and N . We are particularly interested in minimizing sensitivity.

Consistency is given by Leave-One-Out (LOO) errors. For each configuration, the normality model is computed using all healthy cases except one, which is used as test. The process is repeated for each healthy subject and the false positive rate ($1 - sens$) is computed at each round. We define our measure of consistency (\mathcal{E}_C) as the average of LOO errors for the sequences of all healthy cases. The threshold Th is defined by the radius of the ellipsoid containing 95% of the normal samples. In this manner, the consistency error should keep around 5%. Any increase might be attributed to errors in the computation of the statistical model parameters. It follows that \mathcal{E}_C indicates the maximum number of dimensions that can be reliably modelled with a

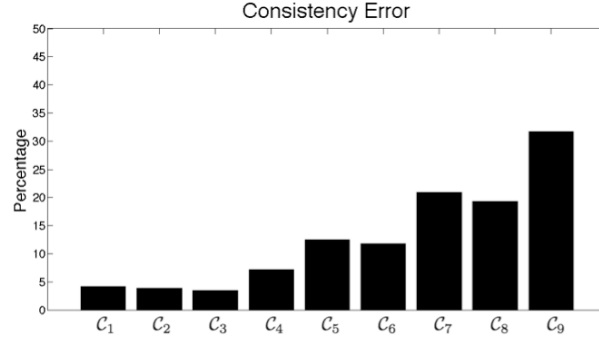


Figure 6.5: Leave-one-Out Errors for the 9 parameter configurations.

given number of healthy samples. The threshold value is $Th = 2.4$ for 2 dimensions (C_1 to C_3), $Th = 2.8$ for 3 dimensions (C_4), $Th = 3.1$ for 4 dimensions (C_5 and C_6), $Th = 3.35$ for 5 dimensions (C_7 and C_8) and $Th = 4.1$ for 7 dimensions (C_9).

Concerning discriminant capability, we will check the ability of the system to perform as a human expert. Since manual labelling of sequences is prone to vary across experts, the system will perform as one of them if classification errors compare to inter-observer variability [102]. Inter-observer variability (sensitivity and specificity) is computed by taking one of the experts labelling as ground truth and the other one as configuration output. Receiver operating characteristics (ROC) curves are used to define the optimal cutoff threshold Th . We define the cutoff value as the radius that achieves the same sensitivity as inter-observer sensitivity, which is 0.7732 in our case. Since we have one ROC curve for each expert, the cutoff Th is given by the average of the cutoff values for both experts. This optimal Th is used to assess each configuration. We have considered the following agreement measures between each configuration and expert: area under ROC curve (AUC), Spearman rank correlation (Corr) [85], specificity, sensitivity and confidence intervals (CI) for mean differences. Agreement scores have been computed using stratified by sequence analysis. Results for each sequence were aggregated in order to obtain confidence intervals and standard errors (given by mean \pm standard deviation) using sequences as experimental unit. In this manner, agreement measures incorporate inter sequence variability.

Model Consistency

Figure 6.5 shows the graphic of bars for model consistency for the 9 configurations. By the choice of the threshold (including 95% of the healthy population) errors should keep around 5%. Configurations (C_1 to C_4) under 4 dimensions are the only spaces fulfilling such condition. Four dimensional configurations (C_5 , C_6) raise to 10% and higher dimensional spaces reach errors over 20%. For equal dimension, we observe a worse performance in configurations including directional strains (C_2 , C_5 and C_7).

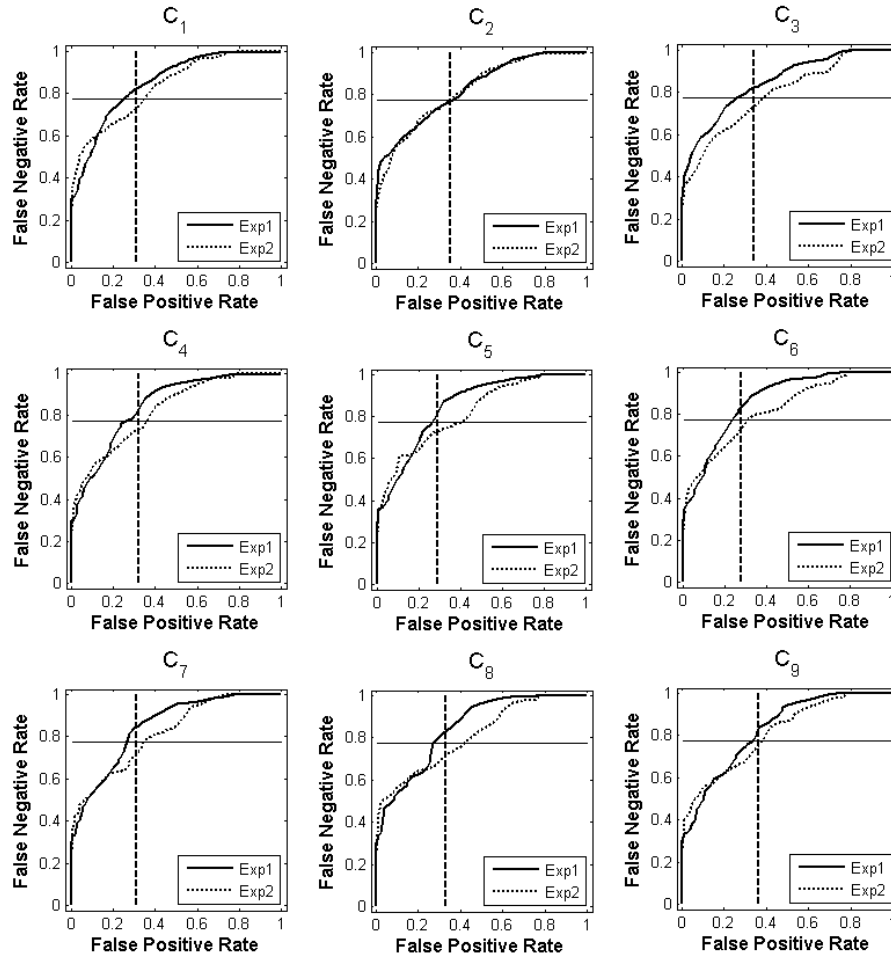


Figure 6.6: ROC plots for the 9 configurations showing ROC curves for the two experts and the optimal cutoff (horizontal line).

Pathology Discrimination

Figure 6.6 shows ROC plots for the 9 configurations. Each plot shows the ROC curves for the two experts (labelled 'Exp1', 'Exp2'), the cutoff line of 0.7732 sensitivity (horizontal solid line) and the average false positive rate achieved with this criterion (vertical dashed line). Plots for C_2 and C_9 present the most linear profile in the middle part of the ROC curve. Except for configuration C_3 , which is biased towards Exp1, all configurations agree with Exp2 for high sensitivity (left part of ROC plots) and with Exp1 for medium-high specificity (right part of ROC plots). Concerning cutoff lines, C_5 and C_6 are the best performers in terms of false positive rates (given by vertical dashed lines). The average of the values given by the intersection of the

Table 6.4: Statistics summary.

	AUC	SensRnk	SpecRnk	SensCI	SpecCI	Corr
\mathcal{C}_1	0.86	71.6 ± 29.9	80.7 ± 21.1	(-22.4, 10.9)	(-11.2, 12.9)	0.29
\mathcal{C}_2	0.85	73.0 ± 27.1	79.8 ± 20.2	(-19.9, 11.4)	(-11.7, 11.7)	0.26
\mathcal{C}_3	0.84	74.2 ± 28.9	76.7 ± 21.4	(-19.4, 13.2)	(-15.3, 9.0)	0.25
\mathcal{C}_4	0.86	71.2 ± 29.5	80.1 ± 23.2	(-22.6, 10.4)	(-12.6, 13.1)	0.30
\mathcal{C}_5	0.86	75.8 ± 24.3	79.0 ± 27.5	(-16.2, 13.2)	(-15.2, 13.6)	0.27
\mathcal{C}_6	0.86	77.6 ± 23.6	76.5 ± 26.1	(-14.2, 14.7)	(-17.2, 10.5)	0.29
\mathcal{C}_7	0.85	77.1 ± 25.8	75.1 ± 30.2	(-15.4, 15.0)	(-20.2, 10.7)	0.26
\mathcal{C}_8	0.85	74.9 ± 25.5	73.5 ± 30.1	(-17.5, 12.7)	(-21.7, 9.1)	0.22
\mathcal{C}_9	0.85	73.8 ± 27.2	75.1 ± 26.5	(-19.2, 12.2)	(-18.8, 9.3)	0.23
IO	-	77.3 ± 29.4	79.8 ± 23.1	-	-	0.39

cutoff horizontal line with each expert ROC curve gives our optimal cutoff thresholds, which are $\{1.70, 1.35, 1.40, 2.00, 2.35, 2.35, 2.65, 2.70, 3.45\}$ for $\mathcal{C}_1 - \mathcal{C}_9$.

Table 6.4 reports the statistical scores assessing $\mathcal{C}_1 - \mathcal{C}_9$, as well as, the comparison to inter-observer (IO) variability. We give the average area under ROC curves (AUC), sensitivity (SensRnk) and specificity (SpecRnk) ranges (mean ± standard deviation, computed for the two experts), confidence interval (SensCI, SpecCI) for mean differences and Spearman rank correlation (Corr). The top performers for each score are in boldface. Configurations \mathcal{C}_5 and \mathcal{C}_6 are the ones achieving a best compromise between sensitivity and specificity.

Figure 6.7 shows BEPs for the two experts manual labelling and the color map for \mathcal{C}_6 . As the inter-observer ranges (SensRnk, SpecRnk) of Table 6.4 suggest, there is a substantial variability between the two experts labels. The larger disagreement is in the hypertrophic case (Pat.#4) followed by Pat.#5. For the latter, our method performs closer to Expert2, which is identifying injured segments, while Expert1 considers a normal motion. In general, \mathcal{C}_6 achieves a good compromise between both experts, specially for affected segments (sensitivity). The only exception is the basal level of Pat.#7, which is labelled green when both experts consider that it presents an abnormal behavior. However, we note that the classification output is in the transition area (dark colors) between normal and affected. We also observe that apical levels achieve the lowest agreement, with a higher rate of false positive detections (specificity).

6.5 Discussion

6.5.1 Normality Patterns

Although rotation and torsion may seem oversimplified function scores, they are gaining popularity in clinical practice. This is due to the fact that these scores are strongly related to the ventricular ejection and filling [79]. Results reported in Table 6.2 show an increase in error ranges along systole. We attribute the apparent increase in ranges for torsion to an increase in its values, since, in fact, the relative range decreases from 57% at begin systole to 16% at end-systole. Still, a standard deviation below 2 selects

torsion as a reliable parameter to be taken into account in clinical routine for myocardial function assessment. In fact, our normality patterns of rotation are visually consistent to those obtained by manually selecting points in [114].

6.5.2 RWMA Assessment

Model Consistency

Regardless of the dimension, the classifier boundary of the normal group was defined by the ellipsoid containing 95% of the normal samples. Therefore the consistency error should keep around 5%. Any increase might be attributed to errors on the computation of the statistical model parameters. The reliability of any statistical analysis drops with either low or dependant number of samples unable to properly explain the variability of the feature space.

In our case, consistency decreases as the dimensionality increases (over 20% for spaces over 4 dimensions). We attribute such phenomenon to a low number of volunteers (21) used to compute the statistical model in comparison to the space dimension. Thus, parameter configurations should reach the best compromise between number of scores (determined by the number of healthy samples available) and capability for pathology detection. The lower performance of spaces including directional strains is attributed to computational and accumulation errors (they rely on the accuracy of directions estimation).

Pathology Discrimination

Table 6.4 shows that configurations under 5 dimensions including motion are favored. This agrees to the fact that visual identification of RWMA strongly relies on motion. In fact, human experts fail to properly detect areas of abnormal strain, as the hypertrophic Pat.#4 illustrates. It follows that configurations combining strain and motion might improve image based diagnosis. The configuration achieving the best compromise among the agreement scores considered is \mathcal{C}_6 .

Table 6.5 reports for each level (base, mid and apex) the ranges for accuracy ($(TP+TN)/(P+N)$), specificity and sensitivity obtained by \mathcal{C}_6 for their comparison to agreement to visual assessment achieved by the models of normal wall motion reported in [185]. Average percentages for the ICA-based method (ICA) proposed in [185] and wall thickening (WT) computed using the software developed in [202] are given in Table 6.6. For the apical level, visual identification of anatomical landmarks (especially \mathbf{x}_{ant} and \mathbf{x}_{inf} defining the septal segment) required for NPD definition is sensitive to subjectivity, which drops the model accuracy to 64%. However, specificity compares to WT and sensitivity is a 20% higher than ICA and WT. Although mid level accuracy is a bit lower than ICA and WT, it is the level showing the best compromise between specificity and sensitivity. Sensitivity is higher than ICA and WT, while specificity is between them. Finally, basal level outperforms ICA and WT, achieving the highest specificity (82%).

Table 6.5: RWMA validation for C_6

	AccRnk (%)	SensRnk (%)	SpecRnk (%)
base	70.0 \pm 19.5	73.7 \pm 32.7	81.6 \pm 24.5
mid	65.8 \pm 18.8	74.3 \pm 21.1	73.3 \pm 26.6
apex	63.7 \pm 17.0	80.6 \pm 22.7	69.9 \pm 31.0

Table 6.6: RWMA validation for ICA-method and WT reported in [185]

	ICA			WT		
	Acc	Sens	Spec	Acc	Sens	Spec
base	63.70	60.83	66.00	70.00	65.83	73.33
mid	67.41	65.12	69.50	68.52	60.47	75.89
apex	66.67	59.42	71.17	62.22	60.87	63.06

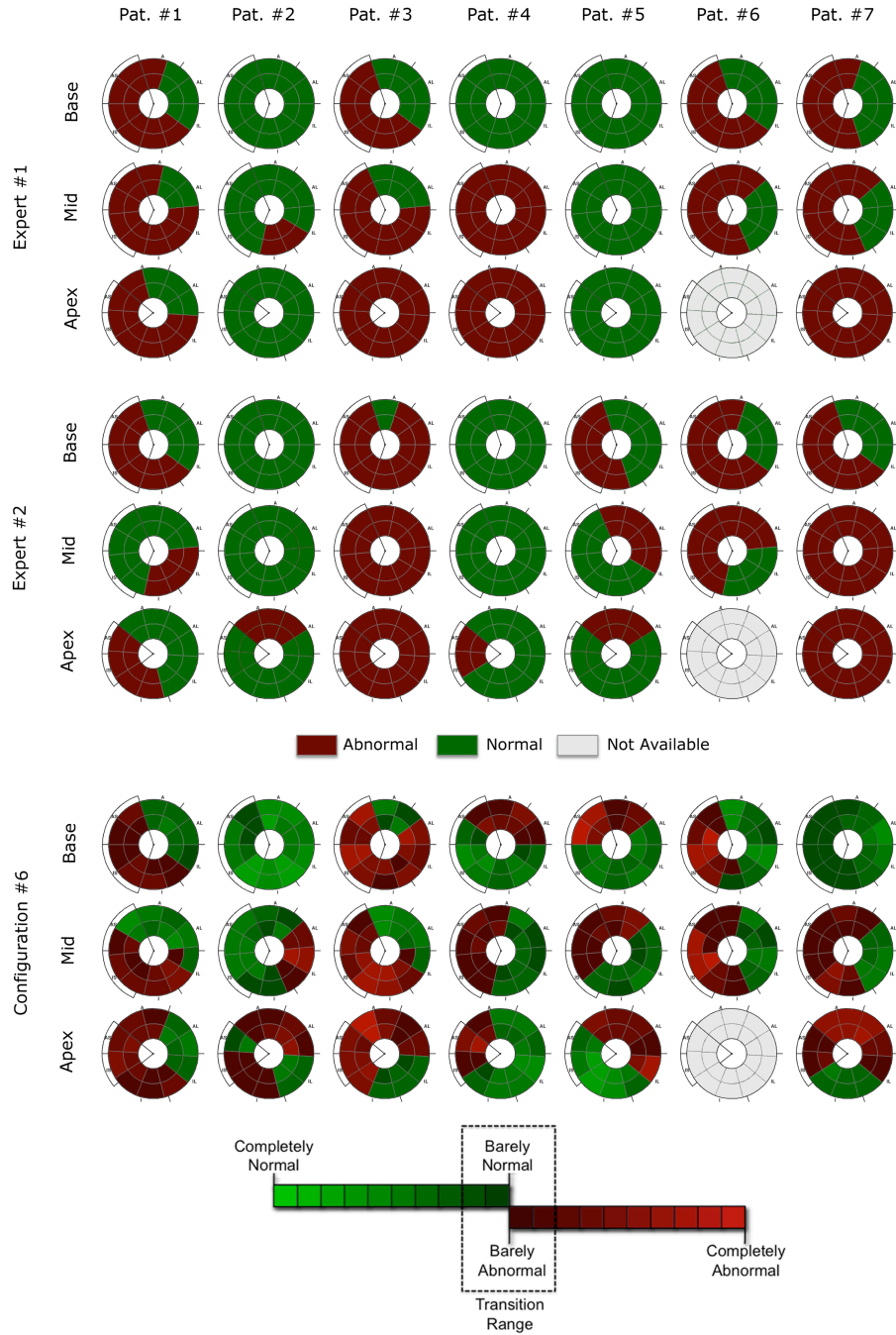


Figure 6.7: BEPs for ground truth provided by the clinical experts and classification given by $C_6 = [V_u, V_w, S_M, S_m]$.

Motion at Base

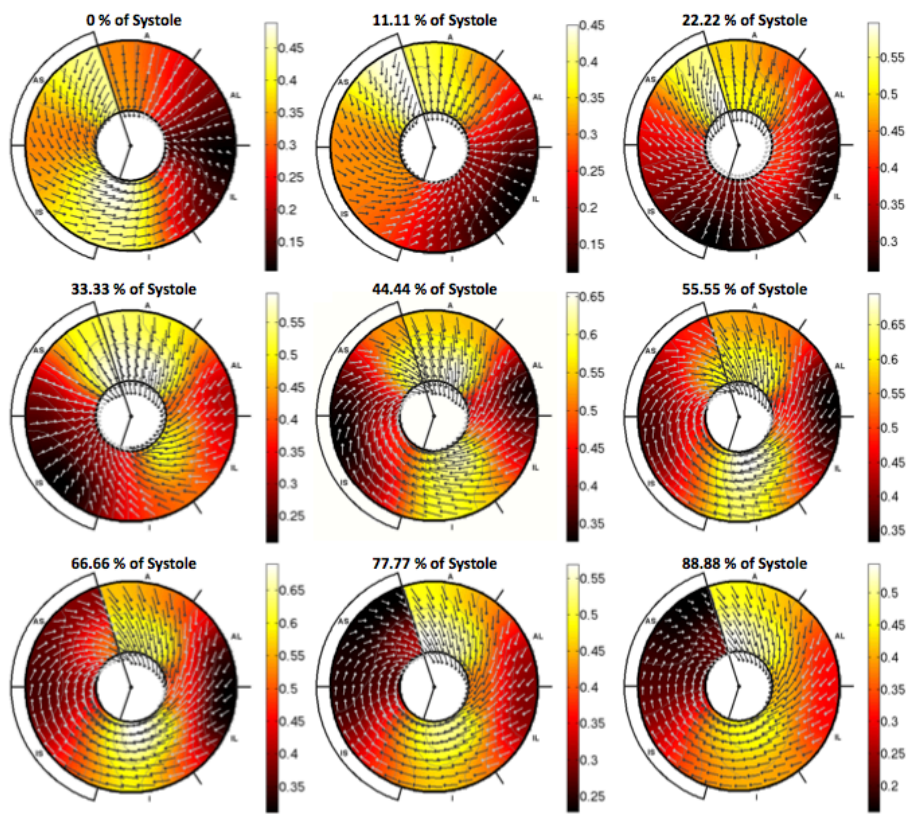


Figure 6.8: Normality patterns of motion measured in $mm.$ at base in 9 phases of the systolic cycle.

Motion at Mid

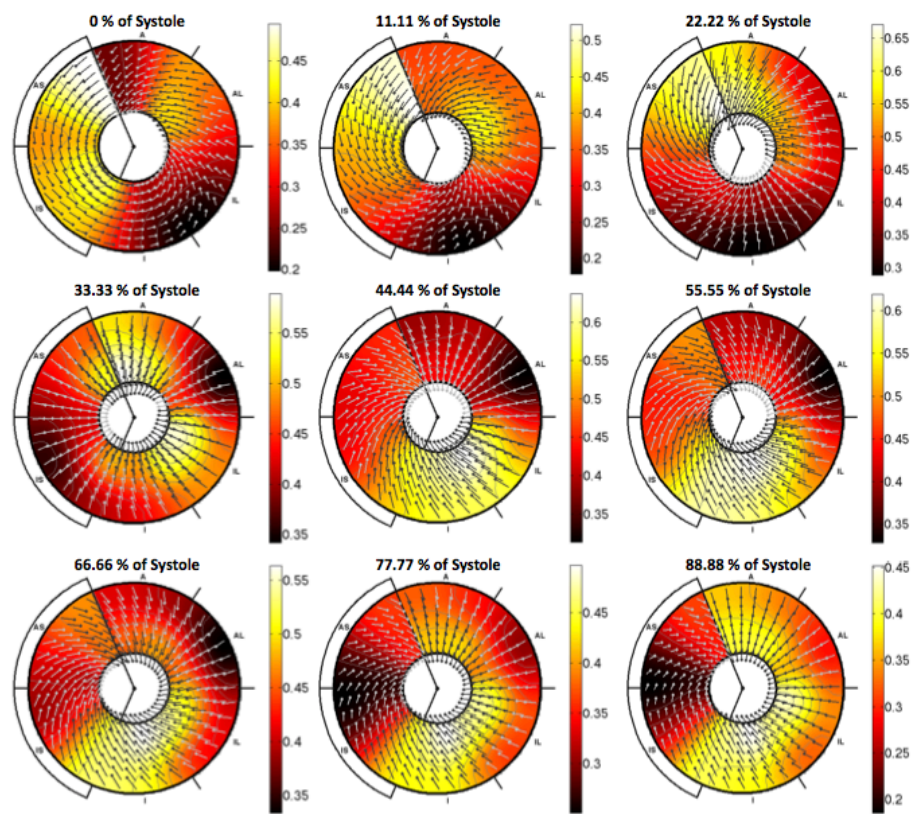


Figure 6.9: Normality patterns of motion measured in $mm.$ at mid in 9 phases of the systolic cycle.

Motion at Apex

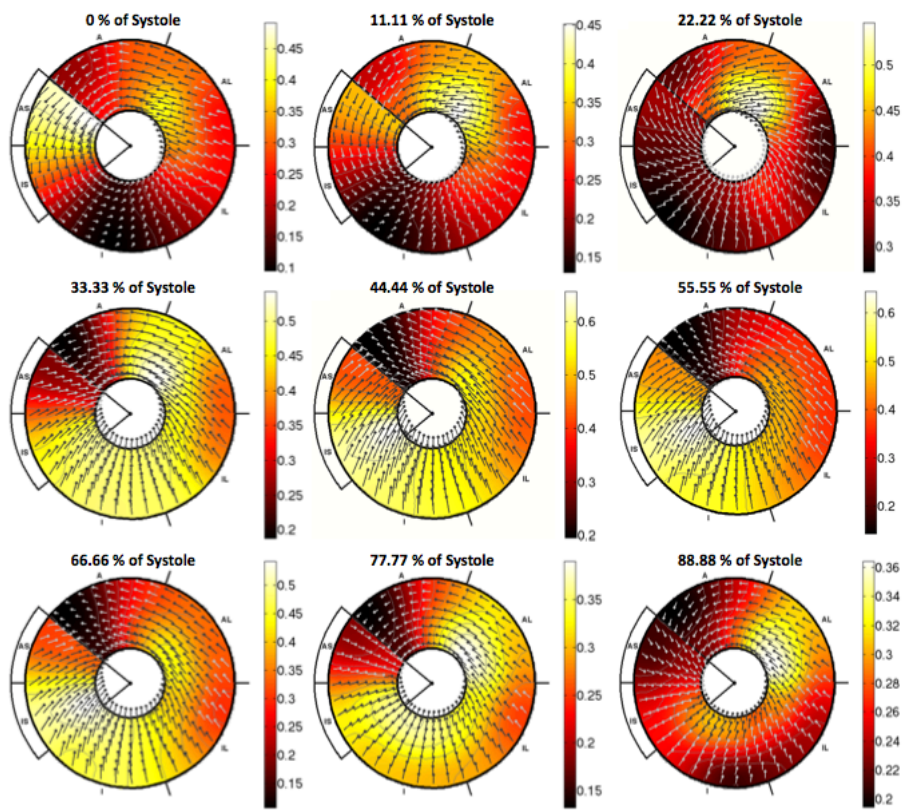


Figure 6.10: Normality patterns of motion measured in $mm.$ at apex in 9 phases of the systolic cycle.

Circumferential Strain at Base

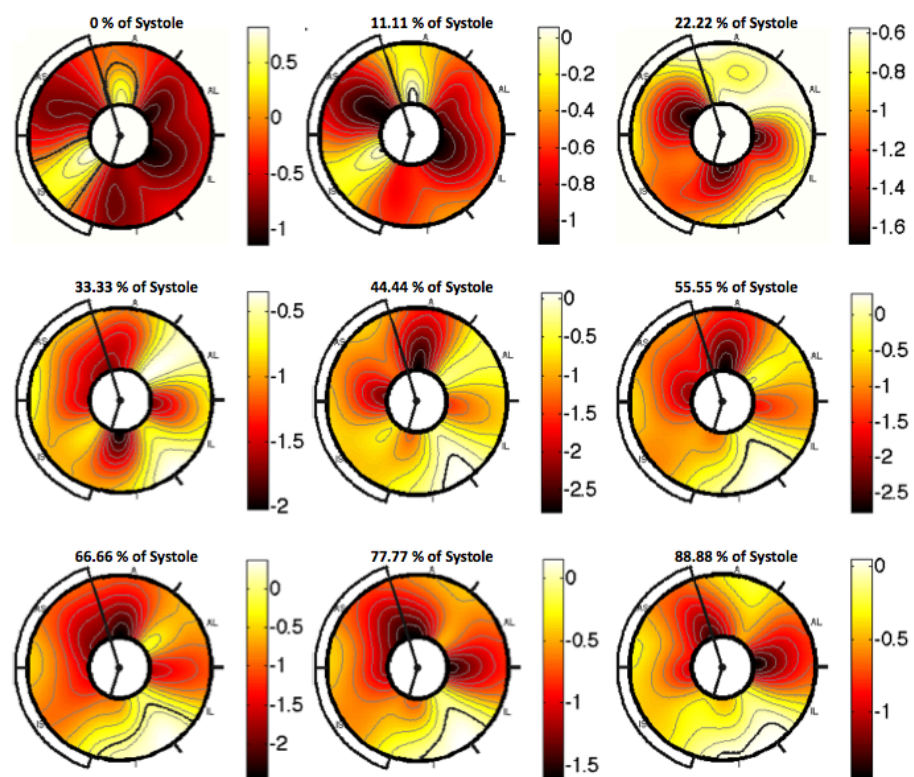


Figure 6.11: Normality patterns of circumferential strain measured in % at base in 9 phases of the systolic cycle.

Circumferential Strain at Mid

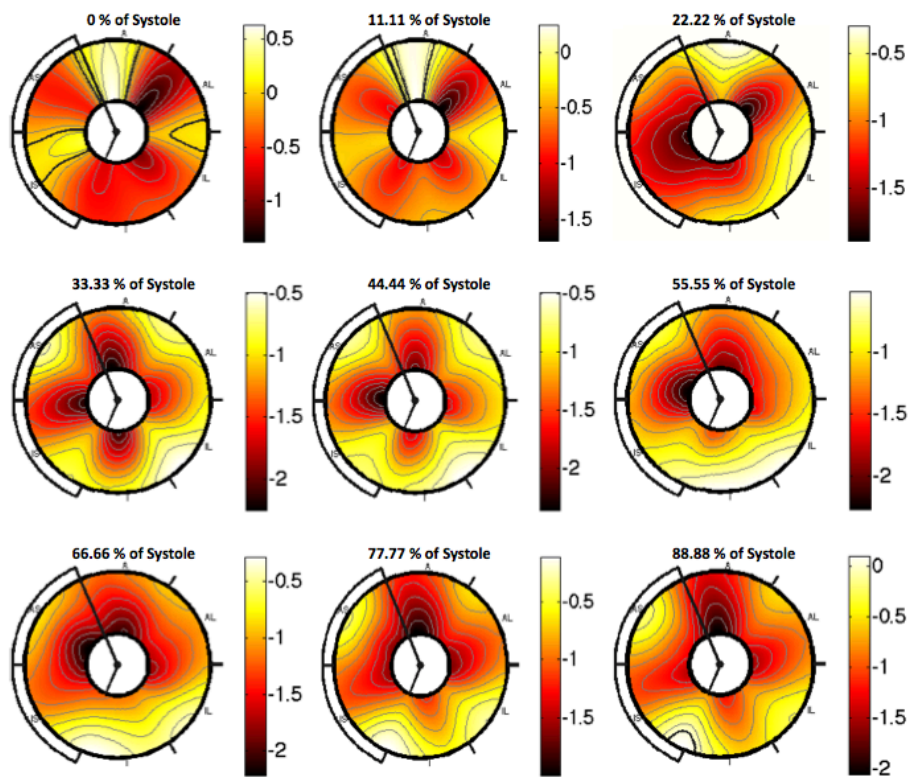


Figure 6.12: Normality patterns of circumferential strain measured in % at mid in 9 phases of the systolic cycle.

Circumferential Strain at Apex

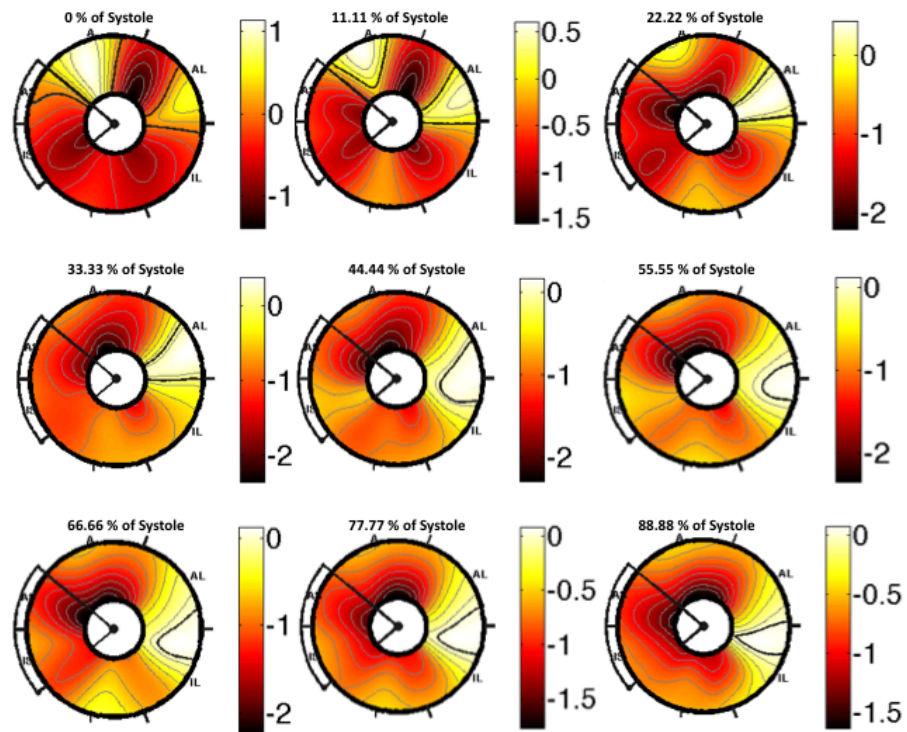


Figure 6.13: Normality patterns of circumferential strain measured in % at apex in 9 phases of the systolic cycle.

Radial Strain at Base

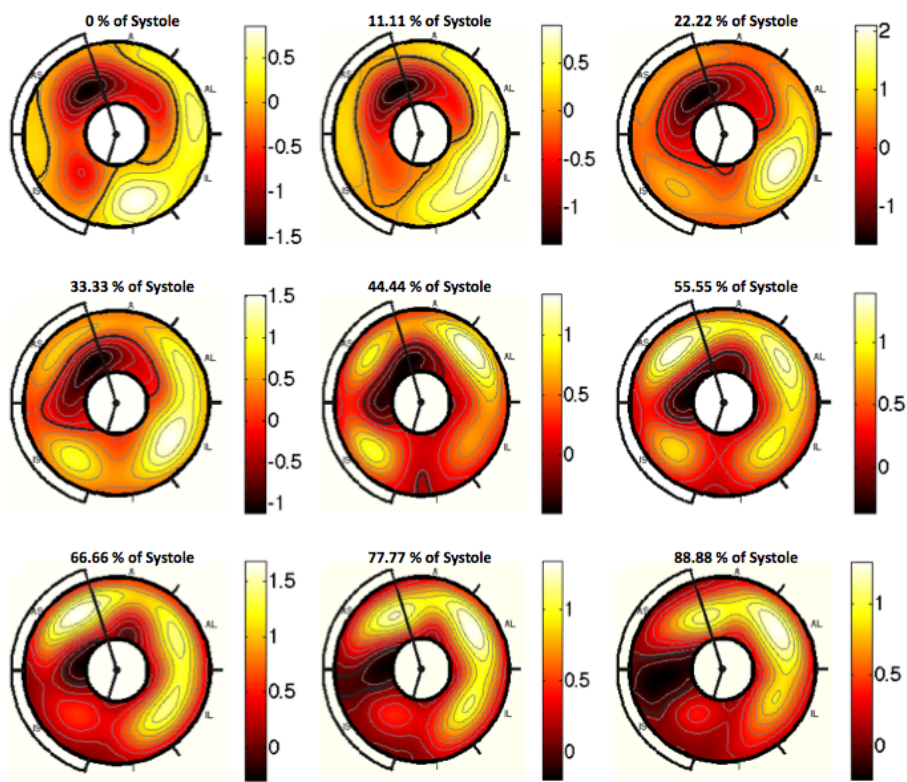


Figure 6.14: Normality patterns of radial strain measured in % at base in 9 phases of the systolic cycle.

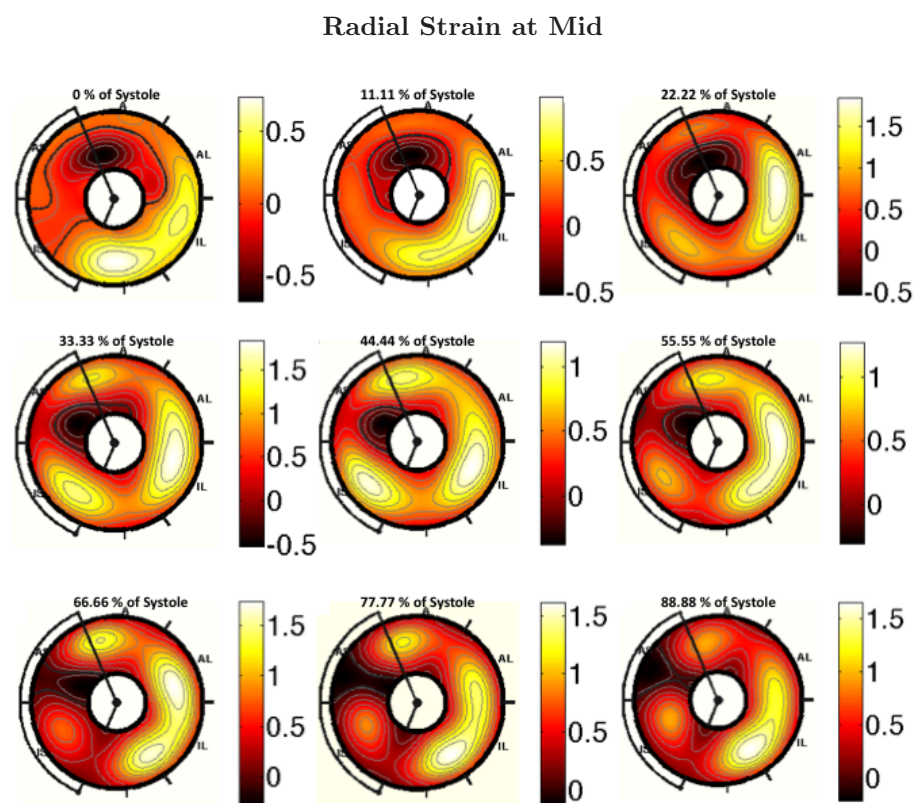


Figure 6.15: Normality patterns of radial strain measured in % at mid in 9 phases of the systolic cycle.

Radial Strain at Apex

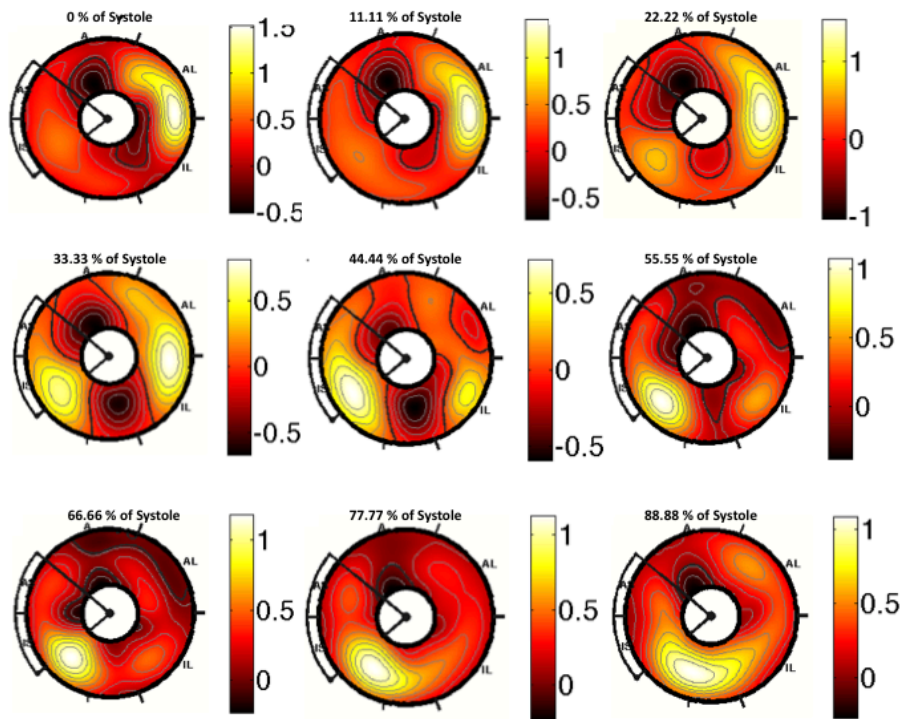


Figure 6.16: Normality patterns of radial strain measured in % at apex in 9 phases of the systolic cycle.

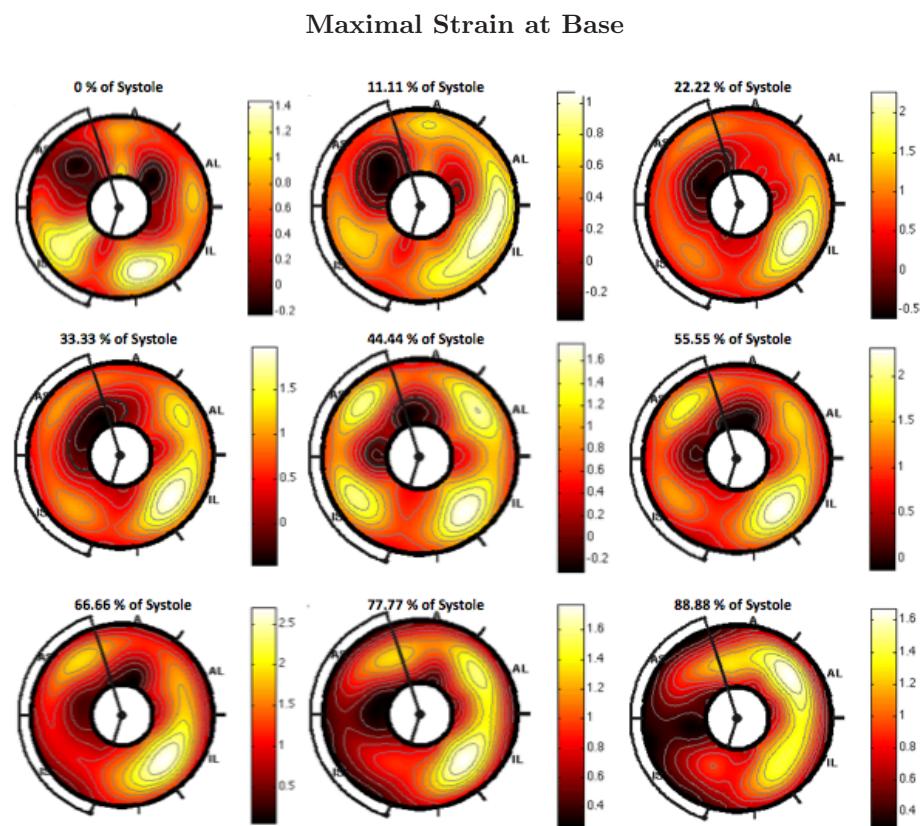


Figure 6.17: Normality patterns of maximal strain measured in % at base in 9 phases of the systolic cycle.

Maximal Strain at Mid

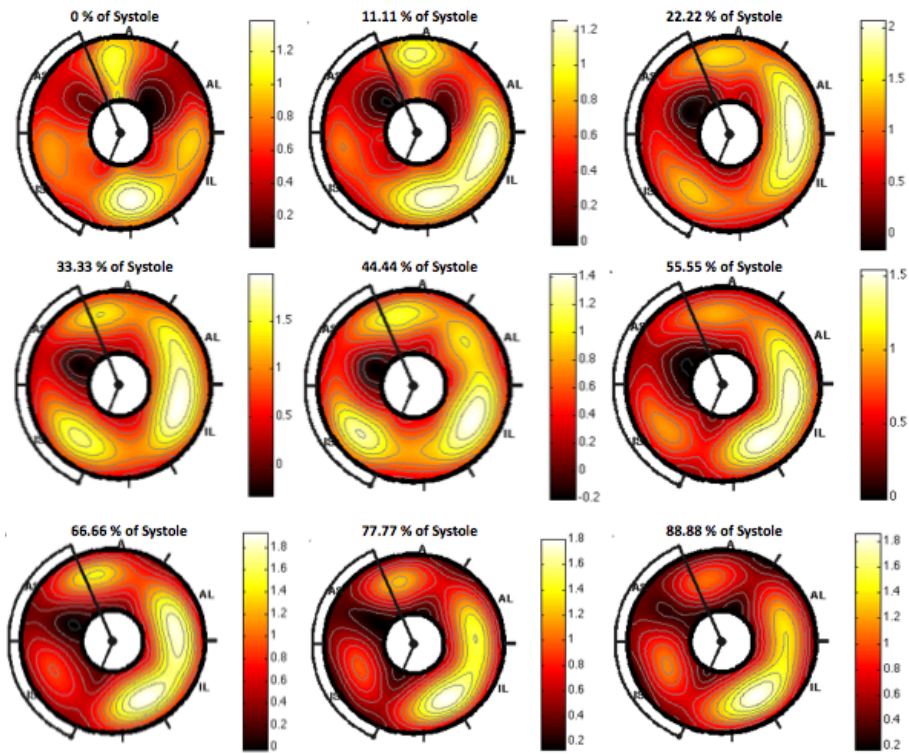


Figure 6.18: Normality patterns of maximal strain measured in % at mid in 9 phases of the systolic cycle.

Maximal Strain at Apex

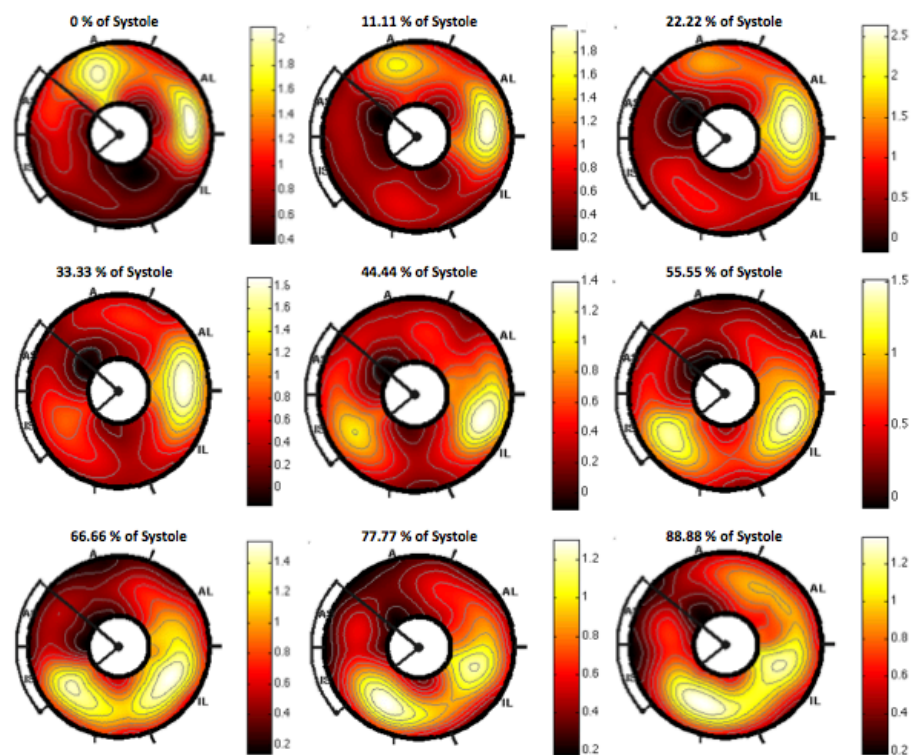


Figure 6.19: Normality patterns of maximal strain measured in % at apex in 9 phases of the systolic cycle.

Minimal Strain at Base

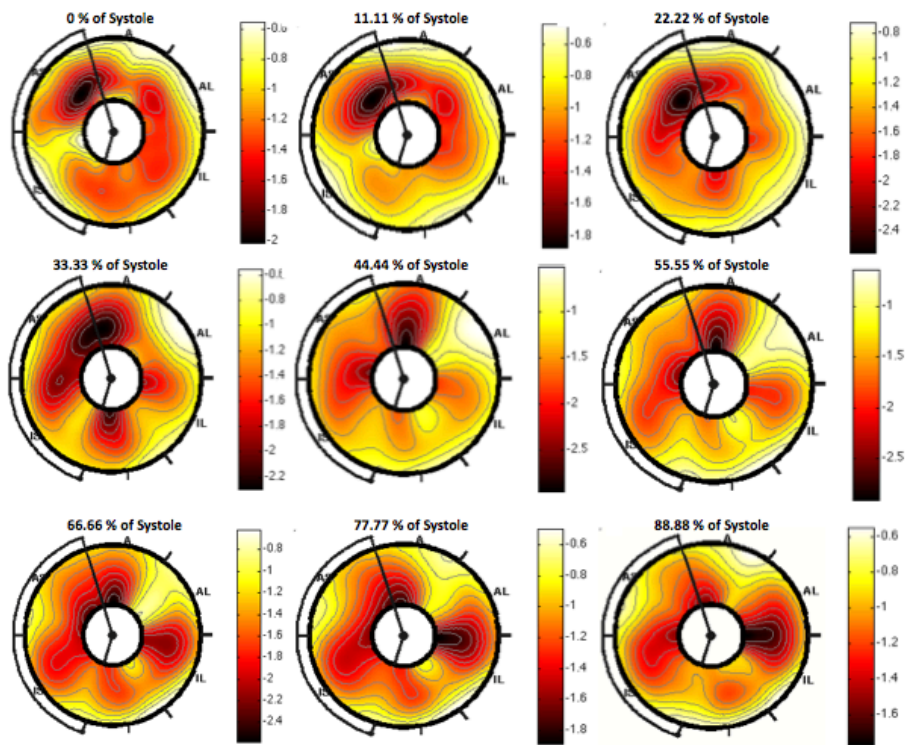


Figure 6.20: Normality patterns of minimal strain measured in % at base in 9 phases of the systolic cycle.

Minimal Strain at Mid

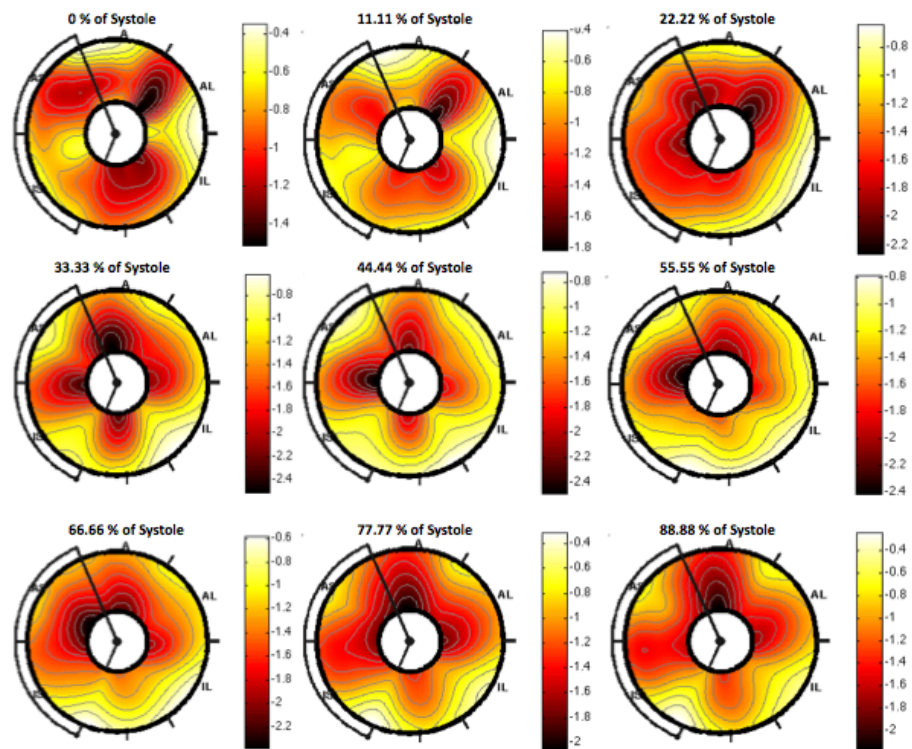


Figure 6.21: Normality patterns of minimal strain measured in % at mid in 9 phases of the systolic cycle.

Minimal Strain at Apex

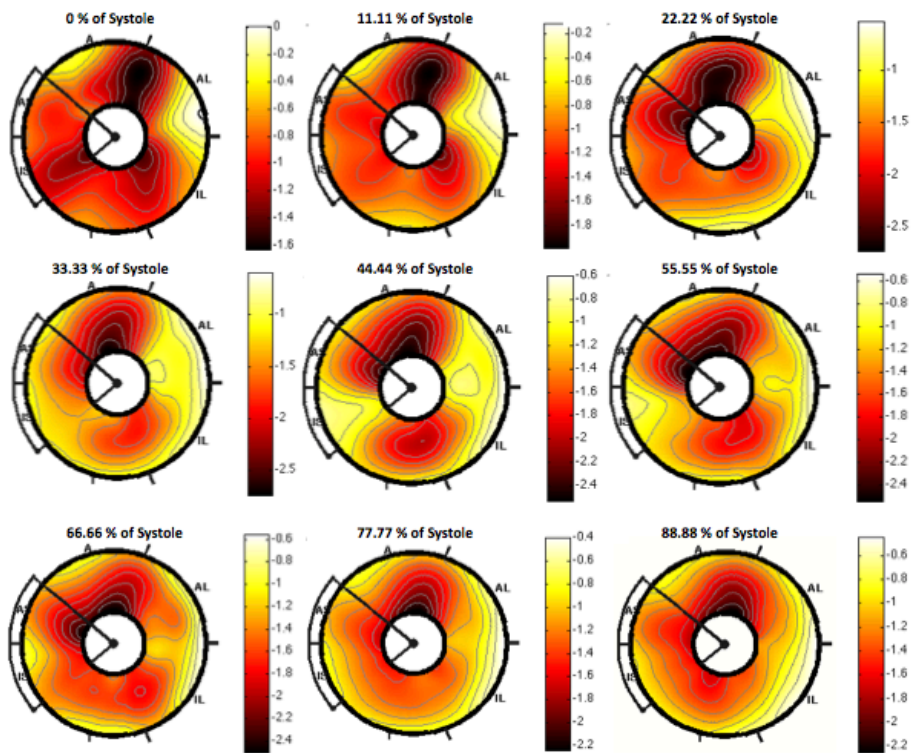


Figure 6.22: Normality patterns of minimal strain measured in % at apex in 9 phases of the systolic cycle.

Chapter 7

Conclusions and Future Lines of Research

Conclusions

Statistical models are a valuable clinical tool for defining objective criterions quantifying the degree of (anomalous) deviation of the LV anatomy and function from the expected patterns. The computation of statistical models requires extracting data from medical images, defining a comparison domain for data extracted from different acquisitions and designing suitable statistical protocols. In this thesis we have presented two computational tools that actively contribute to the creation of statistical models. More precisely, the Harmonic Phase Flow methods contributes to the data extraction step and the Normalized Parametric Domain framework contributes to the comparison framework step. These tools have been applied to computing statistical models of, both, the anatomy and the function of the LV.

1. Harmonic Phase Flow: We have designed a novel variational approach for tracking motion in TMR sequences. Two families of Gabor filters have been designed in order to obtain a complex representation of TMR images with two main properties. The phase of the Gabor responses provide information of the tag deformation. Thus, optical flow for Gabor phases matches consecutive frames. The amplitude of the Gabor responses provide a measure of the reliability of the tag pattern. Thus, low values detect areas with a corrupted tag pattern.

Our variational method present a simple formulation that gathers in a single equation a matching and a regularization term weighted by Gabor amplitude. In this manner, smoothness constrains are imposed just at areas were motion might not be reliably estimated. The final result is a dense smooth vector field, called Harmonic Phase Flow, that characterizes tissue motion without overestimating it at affected areas.

Accuracy of HPF has been tested in synthetic and experimental data. Experiments in both data sets report that HPF achieves subpixel accuracy, which validates the method for motion tracking in TMR sequences.

2. Normalized Parametric Domain: We have seen that for those anatomical structures (in our case the LV) admitting a single parametrization chart, it is possible to define the NPD framework. Such framework bases on the parametrization (using B-Splines) of the LV volume in the sense of differentiable manifolds. Since the parametric map is defined taking into account anatomical landmarks identifiable for any subject, it ensures implicit registration of any LV to a unitary template (parametric domain). Some of the main advantages that the NPD framework presents over existing explicit registration approaches and existing coordinate systems, are the following:

- Since the anatomies of all subjects are registered to a common domain, Ω^n , the NPD framework overcomes the problem (in registration approaches) of choosing a reference anatomy.
- The NPD framework allows to intuitively localize any anatomical point since each of them is labelled with a parameter common to any subject.
- By definition, coordinate curves faithfully describe the geometry of the anatomical structure (run parallel to its boundaries). Thus, segments adapted to such geometry are defined by means of a rectangular grid in Ω^n .
- Quantitative (scalar and vectorial) scores obtained over the anatomical structure can be mapped onto this template were pointwise comparison of data belonging to different subjects (and times) can be reliably done.
- The formulation of the parametrization maps by means of B-Splines, allows the continuous modelling of the anatomical structure by a discrete set of control points presenting a vector space structure. This enables the modelling of the geometry of the anatomical structure as in point distribution models which, by its linear formulation, are easy to implement.
- Local operations, such as interpolation or smoothing according to the geometry of the anatomical structure, can be done along the rectangular axis of Ω^n . For instance in the 2D case, coordinate directions over the manifold correspond to vertical (rows) and horizontal (columns) directions. This considerably simplifies the mathematical formulation and the computational cost.
- Vectorial quantities expressed in the local reference system given by (4.3) have a clinical interpretation in terms of the anatomical structure (local references).

3. Anatomy Modelling: Current approaches for building statistical models of the LV consider separately the gross geometry and the fiber architecture. We have used the NPD framework for the creation of a statistical atlas gathering both of them. On one hand, the gross anatomy has been modelled by means of PCA applied to the

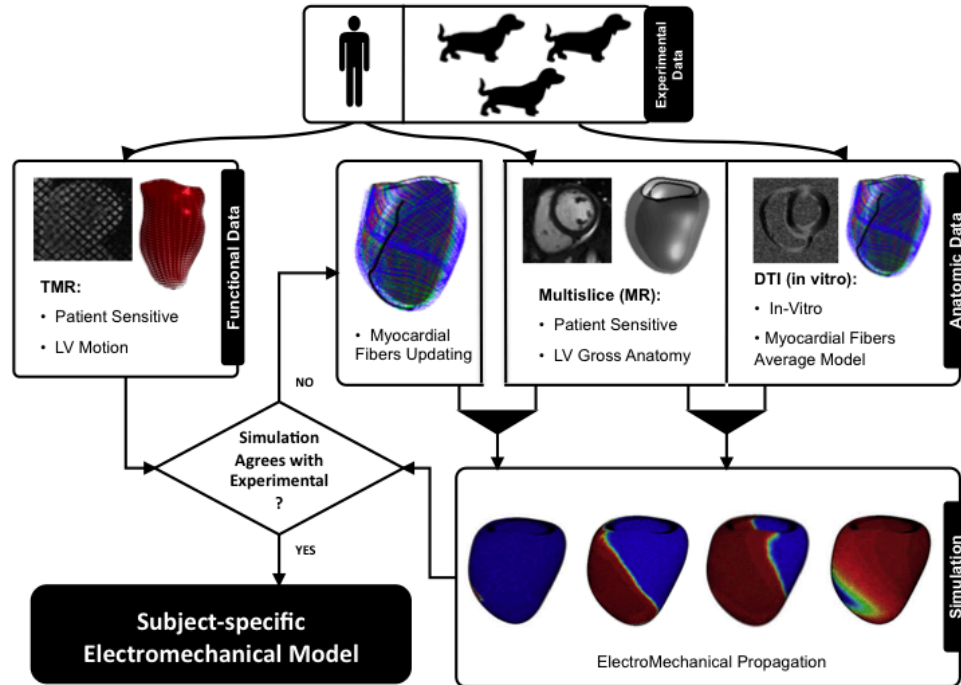


Figure 7.1: Scheme of the proposed iterative method for the creation of patient-tailored electromechanical models.

control points of the BSpline-based parameterizations. On the other hand, the fiber architecture has been modelled in Ω^3 using Riemmanian metrics. Since the myocardial fibers are modelled in an abstract template common to any parameterized subject, the average fiber architecture can be mapped to any subject. In particular, to the mean gross anatomy of the LV.

We have also designed a coloring method based on anatomical information that allowed to observe that the myocardial fibers run oppositely in two concentric rings. The discontinuity between both rings is interpreted as the HMVB dissection path. Moreover, results of trectography performed on the our mean model visually correlate to the HMVB architecture.

4. Function Modelling: We have used the HPF in order to obtain global (rotation and torsion) and local (motion and strains) function indicators. Normality patterns of global scores agree with those obtained by means of manual intervention. Local scores have been separately modelled in the NPD. Besides, we have addressed, for the first time, determining which set of local indicators form the optimal configuration for RWMA detection. Our experiments conclude that an optimal (within inter-observer variability) RWMA detection should consider motion and extremal strains.

Future Lines of Research

The main future lines of research are the following:

- 1. Estimation of LV 3D Motion:** A more precise modelling of LV function requires the estimation of 3D motion from sets of complementary (SA and LA) TMR slices. In such case, we will be able to use the 3D NPD framework in order to extend current results of 2D function modelling.
- 2. Tracking in Generic Sequences:** Although HPF was initially designed for tracking motion in TMR sequences, preliminary experiments show that Gabor phase also remains constant in generic sequences. Thus, HPF could be extended to video sequences.
- 3. Subject Specific Electromechanical Models of the LV:** The creation of subject-specific electromechanical models is a tool that would directly benefit the planning of specific interventions and therapies. These models require the knowledge of the myocardial fiber distribution for the subject under consideration. A main limitation is that DTI studies can only be acquired in-vitro, which hinders the creation of such models. We are planning to develop an iterative method for obtaining patient-tailored fibers distribution. Such method involves the computation of an initial average model of fibers distribution and a means of mapping it to a given LV geometry. These two points are naturally handled by the HPF framework. In addition it requires the interaction between simulations and experimental data given by the application of electromechanical propagation models and the estimation of LV 3D motion. Figure 7.1 sketches the pipeline of the whole method.

It is worth to mention that the average fiber distribution mapped onto the average gross anatomy presented in Chapter 5, is currently being used by a research group at Barcelona Supercomputing Center¹ in order to develop appropriate electromechanical propagation models.

¹www.bsc.es

Publications and Funded Projects

Journals

International Journals

- J. Garcia-Barnés, D. Gil, L. Badiella, A. Hernández, F. Carreras, S. Pujades and E. Martí. A Normalized Framework for the Design of Feature Spaces Assessing the Left Ventricular Function. *IEEE Trans. Med. Imag.* Minor revisions.
- J. Garcia-Barnés, D. Gil, S. Pujadas, F. Carreras. A Variational Framework for Assessment of the Left Ventricle Motion. *Mathematical Modelling on Natural Phenomena*, 3:76-100, 2008.

National Journals

- J. Garcia-Barnés, D. Gil, S. Pujadas, F. Carreras. Valoración de la Función del Ventrículo Izquierdo Mediante Modelos Regionales Hiperparamétricos. *Revista Española de Cardiología (Sup.)*, 61:79, 2008.

Congress Contributions

International Congress Contributions

- D. Gil, J. Garcia-Barnés, R. Arís, G. Houzeaux, M. Vázquez. A Riemannian approach to cardiac fiber architecture modelling. In *1st International Conference on Mathematical and Computational Biomedical Engineering*, 269, 2009.
- J. Garcia-Barnés, D. Gil, F. Carreras, S. Pujadas. Regional Motion Patterns for the Left Ventricle Function Assessment. In *19th International Conference on Pattern Recognition (ICPR)*, 2008.

- J. Garcia-Barnés, D. Gil, A. Bajo, M. Ledesma-Carbayo. Influence of the Temporal Resolution on the Quantification of Displacement Fields in Cardiac MR Tagged Images. In *IEEE Proc. 35th Computers in Cardiology*, 35:785-788, 2008.
- D. Gil, J. Garcia-Barnés, M. Vázquez, R. Arís, G. Houzeaux. Patient-Sensitive Anatomic and Functional 3D Model of the Left Ventricle Function. In *5th European Congress on Computational Methods in Applied Sciences and Engineering (ECCOMAS)*, 2008.
- J. Garcia-Barnés, M. Vázquez, R. Arís, G. Houzeaux, J.M. Cela. Anatomical and Functional High Performance Computational Electrophysiology Model of the Left Ventricle. In *Grand Challenges in Computational Biology*, 2008.
- J. Garcia-Barnés, D. Gil, S. Pujadas, F. Carreras. A Normalized Parametric Domain for the Analysis of the Left Ventricle. In *Proceedings of the Third International Conference on Computer Vision Theory and Applications, INSTIC Press*, 267-274, 2008.
- J. Barajas, J. Garcia-Barnés, K.L. Caballero, F. Carreras, S. Pujadas. Correction of Misalignment Artifacts Among 2-D Cardiac MR Images in 3-D Space. In *Proc. of Computer Vision for Intravascular and Intracardiac Imaging Workshop from MICCAI*, 114-121, 2006.
- J. Garcia-Barnés, D. Gil, J. Barajas, F. Carreras, S. Pujadas. Characterization of Ventricular Torsion in Healthy Subjects Using Gabor Filters and a Variational Framework. In *IEEE Proc. of Computers in Cardiology*, 33:877-880, 2006.
- J. Garcia-Barnés, J. Barajas, F. Carreras, S. Pujadas. A Physics-Based Validation Technique to Compare Global versus Local Tagged MRI Analysis. In *IEEE Proc. of 32nd Computers in Cardiology*, 32:29-32, 2005.
- D. Rotger, J. Garcia-Barnés, M. Rosales, O. Pujol, J. Mauri. Active Vessel: A New Multimedia Workstation for Intravascular Ultrasound and Angiography Fusion. In *IEEE Proc. of the 30th Computers in Cardiology*, 30:65-68, 2003.
- J. Garcia-Barnés, D. Rotger, F. Carreras, R. Leta. Contrast Echocardiography Segmentation and Tracking by Trained Deformable Models. In *IEEE Proc. of the 30th Computers in Cardiology*, 30:173-176, 2003.

National Congress Contributions

- J. Garcia-Barnés, D. Gil. MIOCARDIA. Computational Framework for Modelling and Assessing the LV Functionality. In *Current Challenges in Computer Vision. Proceedings of the CVCRD 2008*, 3:37-39, 2008.
- C. Santa-Marta, J. Garcia-Barnés, A. Bajo, J.J. Vaquero, M. Ledesma-Carbayo. Influence of the Temporal Resolution on the Quantification of Displacement Fields in Cardiac MR Tagged Images. In *XXVI Congreso Anual de la Sociedad Espanola de Ingeniería Biomédica (CASEIB)*, 2008.

- D. Gil, J. Garcia-Barnés, F. Carreras, M. Ballester, M. Vázquez, R. Arís, G. Houzeaux. Un Model 3D del Ventricle Esquerre Integrant Anatomia i Funcionalitat. In *XX Congrés de la Societat Catalana de Cardiologia (CSCC)*, 2008.
- J. Garcia-Barnés, D. Gil, F. Carreras, S. Pujadas, G. Pons-Lladó, R. Leta, X. Alomar. Patrons de Normalitat Regional per la Valoració de la Funció del Ventricle Esquerre. In *XX Congrés de la Societat Catalana de Cardiologia (CSCC)*, 2008.
- J. Garcia-Barnés, F. Carreras, S. Pujadas, M. Ballester. A Normalized Parametric Domain for the Analysis of the Left Ventricle Function. In *Computer Vision. Advances in Research and Development. Proceedings of the Second CVC Internal Workshop*, 2:71-76, 2007.
- J. Garcia-Barnés, D. Gil, F. Carreras, S. Pujadas, R. Leta, X. Alomar, P. Radeva. Modelització 4-dimensional de la funció sistòlica del ventricle esquerre per cardio-RM etiquetada (tagging miocàrdic). In *XIX Congrés de la Societat Catalana de Cardiologia (CSCC)*, 133-134, 2007.
- K.L. Caballero, J. Barajas, J. Garcia-Barnés, F. Carreras, S. Pujadas. Aligning 2-D Cardiac MR Images in 3-D Space using Normalized Mutual Information. In *Proceedings of the First CVC Internal Workshop*, 1-6, 2006.
- J. Garcia-Barnés, D. Gil, F. Carreras, S. Pujadas. Harmonic Phase Flow for Tissue Motion Estimation in Tagged MR Sequences. In *Proceedings of the First CVC Internal Workshop*, 18-23, 2006.
- J. Garcia-Barnés, J. Barajas, F. Carreras, S. Pujadas, R. Leta, X. Alomar, P. Radeva. Estudi del Moviment de Torsió Ventricular per Cardio-Ressonància Magnètica. In *XVIII Congrés de la Societat Catalana de Cardiologia (CSCC)*, 2006.
- J. Barajas, J. Garcia-Barnés, F. Carreras, S. Pujadas. Angle Images Using Gabor Filter Banks in Cardiac Tagged MRI. In *VIII Congrés Català Intel·ligència Artificial (CCIA)*, 2005.
- J. Garcia-Barnés, P. Radeva. Combining Spectral and Active Shape Methods to track Tagged MRI. In *Recent Advances in Artificial Intelligence Research and Development*, 113:37-44, 2004.

Technical Reports

- J. Garcia-Barnés, P. Radeva. Generalized Active Shape Models Applied to Cardiac Function Analysis. CVC Tech. Report 78, 2004.
- J. Garcia-Barnés, P. Radeva. Propagació de Fronts per a la Segmentació en Imatges IVUS. CVC Tech. Report 65, 2002.

Funded Projects

The contents of this PhD. thesis have recently received funding from the Spanish government for a period of three years: MICINN (Ministerio de Ciencia e Innovación) TIN2009-13618.

Bibliography

- [1] *Heart failure: pathogenesis and treatment.*, chapter partial orientation of the ventricular muscle band and approach to partial ventriculotomy in heart failure, pages 685–693. London: Martin Dunitz, 2002.
- [2] *American Heart Association. Heart Disease and Stroke Statistics 2005 Update.* Dallas, Texas: American Heart Association, 2005.
- [3] J. Abi-Nahed, M.P. Jolly, and G.Z. Yang. Robust active shape models: A robust, generic and simple automatic segmentation tool. In *Medical Image Computing and Computer-Assisted Intervention MICCAI 2006*, volume 4191, pages 1–8, 2006.
- [4] P.S. Jouk ad A. Mourad, V. Milisi, G. Michalowicz, A. Raoult, D. Cailleri, and Y. Usson. Analysis of the fiber architecture of the heart by quantitative polarized light microscopy. accuracy, limitations and contribution to the study of the fiber architecture of the ventricles during fetal and neonatal life. *Eur J Cardiothorac Surg*, 31(5):915–921, 2007.
- [5] O. Akinboboye, G. Germano, O. Idris, and et al. Left ventricular mass measured by myocardial perfusion gated spect. *Clin Nucl Med*, 28:392397, 2003.
- [6] W.F. Ames. *Numerical Methods for Partial Differential Equations.* New York Academic, 1993.
- [7] A.A. Amini and J.S. Duncan. Bending and stretching models for lv wall motion analysis from curves and surfaces. *Imag. Vis. Comput.*, 10(6):418–430, 1992.
- [8] B.H. Amundsen, T. Helle-Valle, T. Edvardsen, and et at. Noninvasive myocardial strain measurement by speckle tracking echocardiography: Validation against sonomicrometry and tagged magnetic resonance imaging. *Journal of the American College of Cardiology*, 47(4):789 – 793, 2006.
- [9] R.H. Anderson, S.Y. Ho, K. Redmann, D. Sanchez-Quintana, and P.P. Lunkenheimer PP. The anatomical arrangement of the myocardial cells making up the ventricular mass. *Eur J Cardiothorac Surg*, 28:517–525, 2005.

- [10] R.H. Anderson, S.Y. Ho, D. Sanchez-Quintana, K. Redmann, and P.P. Lunkenheimer. Heuristic problems in defining the three-dimensional arrangement of the ventricular myocytes. *The Anatomical Record Part A: Discoveries in Molecular, Cellular, and Evolutionary Biology*, 288(6):579–586, 2006.
- [11] K.S. Arun and T.S. Huang and S.D. Blostein. Least-squares fitting of two 3-d point sets. *IEEE Transactions on Pattern Analysis and Machine Intelligence*, 9(5):698–700, 1987.
- [12] V. Arsigny, P. Fillard, X. Pennec, and et al. Log-euclidean metrics for fast and simple calculus on diffusion tensors. *Mag. Res. Med.*, 56(2):411–421, 2006.
- [13] T. Arts, K.D. Costa, J.W. Covell, and A.D. McCulloch. Relating myocardial laminar architecture to shear strain and muscle fiber orientation. *Am J Physiol Heart Circ Physiol.*, 280:2222–2229, 2001.
- [14] T. Arts, W.C. Hunter, A.S. Douglas, A.M.M. Muijtjens, J.W. Corsel, and R.S. Reneman. macroscopic three-dimensional motion patterns of the left ventricle. *Adv. Exp. Med. Biol.*, 346:383–392, 1993.
- [15] L. Axel, S. Chung, and T. Chen. Tagged mri analysis using gabor filters. In *IEEE International Symposium on Biomedical Imaging: From Nano to Macro*, pages 684–687, 2007.
- [16] L. Axel and L. Dougherty. Mr imaging of motion with spatial modulation of magnetization. *Radiology*, 171:841–845, 1989.
- [17] M. Ballester-Rodes, A. Flotats, F. Torrent-Guasp, and et al. Base-to-apex ventricular activation: Fourier studies in 29 normal individuals. *Eur J Nucl Med Mol Imaging*, 2005.
- [18] J. Barajas, J. Garcia-Barnes, F. Carreras, S. Pujadas, and P. Radeva. Angle images using gabor filters in cardiac tagged mri. In *Artificial Intelligence Research and Development*, volume 131, pages 107–114, 2005.
- [19] U. Barcaro, D. Moroni, and O. Salvetti. *Pattern Recognition and Image Analysis*, volume 18, chapter Automatic computation of left ventricle ejection fraction from dynamic ultrasound images, pages 351–358. Springer, 2008.
- [20] A.H. Barr. Superquadrics and angle-preserving deformations. *IEEE Comput. Graph. Applicat.*, 1(1):1123, 1981.
- [21] J.L. Barron, D.J. Fleet, and S.S. Beauchemin. Performance of optical flow techniques. *Int. Journal. Comp. Vis.*, 12(1):43–77, 1993.
- [22] M.F. Beg, M. Miller, A. Trounev, and L. Younes. *Medical Image Computing and Computer-Assisted Intervention - MICCAI 2003*, volume 2879 of *Lecture Notes in Computer Science*, chapter The Euler-Lagrange Equation for Interpolating Sequence of Landmark Datasets, pages 918–925. 2003.

- [23] F. Behloul, B.P.F. Lelieveldt, A. Boudraa, M.F. Janier, D. Revel, and J.H.C. Reiber. Neuro-fuzzy systems for computer-aided myocardial viability assessment. *Medical Imaging, IEEE Transactions on*, 2001.
- [24] S. Benayoun and N. Ayache. Dense and nonrigid motion estimation in sequences of medical images using differential constraints. *Int. J. Comput. Vis.*, 26(1):25–40, 1998.
- [25] F. Bernis, C. Leger, and V. Eder. Regional analysis of the left ventricle of the heart. *Computerized Medical Imaging and Graphics*, 30(3):153–161, 2006.
- [26] P.J. Besl and N.D. McKay. A method for registration of 3-d shapes. *IEEE Transactions on Pattern Analysis and Machine Intelligence*, 14(2):239–256, 1992.
- [27] K.K. Bhatia, J.V. Hajnal, B.K. Puri, A.D. Edwards, and D. D. Rueckert. Consistent groupwise non-rigid registration for atlas construction. In *Biomedical Imaging: Nano to Macro, 2004. IEEE International Symposium on*, pages 908–911, 2004.
- [28] S. Biedenstein, M. Schafers, L. Stegger, T. Kuwert, and O. Schober. Three-dimensional contour detection of left ventricular myocardium using elastic surfaces. *European Journal of Nuclear Medicine and Molecular Imaging*, pages 201–207, 1999.
- [29] A. Bjorck. *Numerical Methods for Least Squares Problems*. SIAM, 1996.
- [30] J. Bosch, F. Nijland, S. Mitchell, B. Lelieveldt, O. Kamp, J. Reiber, and M. Sonka. Computer-aided diagnosis via model-based shape analysis automated classification of wall motion abnormalities in echocardiograms. *Academic Radiology*, 12(3):358–367, 2005.
- [31] G. Brogefors. Hierarchical chamfer matching: A parametric edge matching algorithm. *IEEE Transactions on pattern analysis and machine*, 10(6), 1988.
- [32] G.D. Buckberg, M.L. Weisfeldt, M. Ballester, and et al. Left ventricular form and function: Scientific priorities and strategic planning for development of new views of disease. *Circulation*, 110(14):333–336, 2004.
- [33] Y. Cao, M.I. Miller, R.L. Winslow, and L. Younes. Large deformation diffeomorphic metric mapping of vector fields. *Medical Imaging, IEEE Transactions on*, 24(9):1216–1230, 2005.
- [34] E. Castillo, J. A. Lima, and D. A. Bluemke. Regional myocardial function: advances in mr imaging and analysis. *Radiographics*, 23:127–140, 2005.
- [35] J.C. Cauvin, J.Y. Boire, M. Zanca, J. M. Bonny, J. Maublant, and A. Veyre. 3d modeling in myocardial 201tl spect. *Comput. Med. Imag. Graph.*, 17(4):345350, 1993.

- [36] M.D. Cerqueira, W.J. Weissman, and et al. Standardized myocardial segmentation and nomenclature for tomographic imaging of the heart: a statement for healthcare professionals from the cardiac imaging committee of the council on clinical cardiology of the american heart association. *Circulation*, 105:539–42, 2002.
- [37] R. Chandrashekara, R. H. Mohiaddin, and D. Rueckert. Analysis of 3-d myocardial motion in tagged mr images using nonrigid image registration. *IEEE Trans. Med. Im.*, 23(10):1245–1250, 2004.
- [38] J. Chen, S.K. Song, W. Liu, M. McLean, J.S. Allen, J. Tan, S.A. Wickline, and X. Yu. Remodeling of cardiac fiber structure after infarction in rats quantified with diffusion tensor mri. *Am J Physiol Heart Circ Physiol*, 285:946–954, 2003.
- [39] P.S. Chen, Y.M. Cha, B.B. Peters, and L.S. Chen. Effects of myocardial fiber orientation on the electrical induction of ventricular fibrillation. *Am. J. Physiol.*, 264:17601773, 1993.
- [40] A. Cheng, F. Langer, F. Rodriguez, J.C. Criscione, G.T. Daughters, D.C. Miller, and N.B. Ingels. Transmural sheet strains in the lateral wall of the ovine left ventricle. *Am J Physiol Heart Circ Physiol*, 289:1234–1241, 2005.
- [41] P. Clarysse, C. Basset, L. Khouas, P. Croisille, D. Friboulet, C. Odet, and I. E. Magnin. Two-dimensional spatial and temporal displacement and deformation field fitting from cardiac magnetic resonance tagging. *Medical Image Analysis*, 4(3):253–268, 2000.
- [42] P. Clarysse, M. Han, P. Croisille, and I.E. Magnin. Exporatory analysis of the spatio-temporal deformation of the myocardium during systole from tagged mri. *IEEE Trans. BioMed. Eng.*, 49(11):1328–1339, 2002.
- [43] L.D. Cohen. On active contour models and balloons. *Comput. Vis. Graph. Imag. Processing: Imag. Underst.*, 53(2):211–218, 1991.
- [44] T. Cootes, C. Taylor, D. Cooper, , and J. Graham. Active shape models - their training and application. *Computer Vision and Image Understanding*, 61:38–59, 1995.
- [45] T.F. Cootes, G.J. Edwards, and C.J. Taylor. Active appearance models. In H. Burkhardt and B. Neumann, editors, *European Conference on Computer Vision*, volume 2, pages 484–498, 1998.
- [46] T.F. Cootes, A. Hill, C.J. Taylor, and J. Haslam. *Information Processing in Medical Imaging*, volume 687 of *Lecture Notes in Computer Science*, chapter The use of active shape models for locating structures in medical images, pages 33–47. Springer Berlin / Heidelberg, 1993.
- [47] T.F. Cootes and C.J. Taylor. Statistical models of appearance for medical image analysis and computer vision. In *Proceedings SPIE Medical Imaging 2001, San Diego, CA*.

- [48] K.D. Costa, K. May-Newman, D. Farr, W.G. Odell, A.D. McCulloch, and J.H. Omens. Three-dimensional residual strain in midanterior canine left ventricle. *Am J Physiol Heart Circ Physiol*, 42:1968–1976, 1997.
- [49] B.C. Davis, P.T. Fletcher, E. Bullitt, and S. Joshi. Population shape regression from random design data. In *Computer Vision, 2007. ICCV 2007. IEEE 11th International Conference on*, pages 1–7, 2007.
- [50] C. de Boor. *A Practical Guide to Splines*. Springer-Verlag, 1978.
- [51] J. Declerck, J. Feldmar, and N. Ayache. Definition of a four-dimensional continuous planispheric transformation for the tracking and the analysis of left-ventricle motion. *Med Image Anal.*, 2(2):197–213, 1998.
- [52] J. Declerck, J. Feldmar, F. Betting, and M.L. Goris. Automatic registration and alignment on a template of cardiac stress and rest reoriented spect images. *Medical Imaging, IEEE Transactions on*, 16(6):727–737, 1997.
- [53] X. Deng and T.S. Denney. Three-dimensional myocardial strain reconstruction from tagged mri using a cylindrical b-spline model. *IEEE Trans Med Imaging*, 23(7):861–867, 2004.
- [54] X. Deng and T.S. Denney. Combined tag tracking and strain reconstruction from tagged cardiac mr images without user-defined myocardial contours. *J Magn Reson Imaging*, 21(1):12–22, 2005.
- [55] T. Denney and J. Prince. Optimal brightness functions for optical flow estimation of deformable motion. *IEEE Trans. Imag. Proc.*, 3:178–191, 1994.
- [56] L. Dougherty, J. Asmuth, A. Blom, L. Axel, and R. Kumar. Validation of an optical flow method for tag displacement estimation. *IEEE Trans. Med. Im.*, 18:359–263, 1999.
- [57] M.C. Dulce, G.H. Mostbeck, K.K. Friese, G.R. Caputo, and C.B. Higgings. Quantification of the left ventricular volumes and function with cine mr imaging: Comparison of geometric models with threedimensional data. *Radiology*, 188(2):371376, 1993.
- [58] J.S. Duncan and N. Ayache. Medical image analysis: progress over two decades and the challenges ahead. *Pattern Analysis and Machine Intelligence, IEEE Transactions on*, 22(1):85–106, 2000.
- [59] L.C. Evans. *Partial Differential Equations*. Berkeley Math. Lect. Notes, 1993.
- [60] T.L. Faber, R.W. McColl, R.M. Opperman, J.R. Corbett, and R.M. Peshock. Spatial and temporal registration of cardiac spect and mr images: methods and evaluation. *Radiology*, 179:857–861, 1991.
- [61] H.W. Fei, X.F. Wang, M.X. Xie, and et al. Real-time three-dimensional echocardiography for quantifying left ventricular mass. *Chin Med Sci J*, 19:230 232, 2004.

- [62] M.A. Fernandez-Teran and J.M. Hurle. Myocardial fibre architecture of the human heart ventricles. *Anat Rec*, 204:137–147, 1982.
- [63] P.T. Fletcher and S.C. Joshi. Riemannian geometry for the statistical analysis of diffusion tensor data. *Signal Processing*, 2007.
- [64] C.C Fox and G.M. Hutchins. The architecture of the human ventricular myocardium. *Hopkins Med J*, 130:289–299, 1972.
- [65] A.F. Frangi, W.J. Niessen, and M.A. Viergever. Three-dimensional modeling for functional analysis of cardiac images: A review. *IEEE TRANSACTIONS ON MEDICAL IMAGING*, 20(1):2–25, 2001.
- [66] A.F. Frangi, D. Rueckert, J.A. Schnabel, and W.J. Niessen. Automatic construction of multiple-object three-dimensional statistical shape models: application to cardiac modeling. *Medical Imaging, IEEE Transactions on*, 21(9):1151–1166, 2002.
- [67] M. Ballester G. Pons-Llado, X. Borrás, and et al. Myocardial cell damage in human hypertension. *J Am Coll Cardiol*, 2000.
- [68] L. Geerts, P. Bovendeerd, K. Nicolay, and T Arts. Characterization of the normal cardiac myofiber field in goat measured with mr-diffusion tensor imaging. *Am. J. Physiol.*, 283:H139–H145, 2002.
- [69] S.H. Gilbert, A.P. Benson, P. Li, and "et al.". Regional localization of the left ventricular sheet structure: integration with current models of cardiac fiber, sheet and band structure. *Eur. J. Card-thor. Surg.*, 32:231–249, 2007.
- [70] J.M. Gorce, D. Friboulet, and I.E. Magnin. Estimation of three-dimensional cardiac velocity fields: Assessment of a differential method and application to three-dimensional ct data. *Med. Image Anal.*, 1(3):245–261, 1996.
- [71] A.A. Goshtasby. *2-D and 3-D Image Registration*. John Wiley & Sons, Inc., 2005.
- [72] J.C. Gower. *Generalized procrustes analysis*. Psychometrika, 1975.
- [73] R.P. Grant. Notes on the muscular architecture of the left ventricle. *Circulation*, 2:301–308, 1965.
- [74] R.A. Greenbaum, S.Y. Ho, D.G. Gibson, A.E. Becker, and R.H. Anderson. Left ventricular fibre architecture in man. *Br Heart J*, 45:248–263, 1981.
- [75] G. Grenander and M.I. Miller. *Computational anatomy: An emerging discipline*, volume 56. Quarterly of Applied Mathematics, 1998.
- [76] T. Gustavsson, R. Pascher, and K. Caidahl. Model based dynamic 3d reconstruction and display of the left ventricle from 2d cross-sectional echocardiograms. *Comput. Med. Imag. Graph.*, 17(4):273–278, 1993.

- [77] M. Guttman, J. Prince, and E. McVeigh. Tag and contour detection in tagged mr images of the left ventricle. *IEEE Trans. Med. Im.*, 13:74–88, 1989.
- [78] K.B. Harrington, F. Rodriguez, A. Cheng, F. Langer, H. Ashikaga, G.T. Daughters, J.C. Criscione, N.B. Ingels, and D.C. Miller DC. Direct measurement of transmural laminar architecture in the anterolateral wall of the ovine left ventricle - new implications for wall thickening mechanics. *Am J Physiol Heart Circ Physiol*, 288:324–330, 2005.
- [79] T. Helle-Valle, J. Crosby, T. Edvardsen, and et al. New noninvasive method for assessment of left ventricular rotation speckle tracking echocardiography. *Circulation*, 112:3149–3156, 2005.
- [80] P.A. Helm. *A novel technique for quantifying variability of cardiac anatomy: Application to the dyssynchronous failing heart*. PhD thesis, Johns Hopkins Univ., Baltimore, 2005.
- [81] P.A. Helm, M.F. Beg, M.I. Miller, and et al. Measuring and mapping cardiac fiber and laminar architecture using diffusion tensor mr imaging. *Annals of the New-york Accademy of Science*, 1047:296–307, 2005.
- [82] P.A. Helm, H.J. Tseng, L. Younes, and E.R. McVeigh R.L. Winslow. Ex vivo 3d diffusion tensor imaging and quantification of cardiac laminar structure. *Magn Reson Med*, 54:850–859, 2005.
- [83] P.A. Helm, L. Younes, M.F. Beg, D.B. Ennis, C. Leclercq, O.P. Faris, E. McVeigh, D. Kass, M.I. Miller, and R.L. Winslow. Evidence of structural remodeling in the dyssynchronous failing heart. *Circ Res*, 98:125–132, 2006.
- [84] L.D. Hillis, B.G. Firth, and M.D. Winnifordm. Analysis of factors affecting the variability of fick versus indicator dilution measurements of cardiac output. *The American journal of cardiology*, 56(12):764–768, 1986.
- [85] M. Hollander and D. Wolfe. *Nonparametric Statistical Methods*. John Wiley and Sons, Inc., 1999.
- [86] B.K.P. Horn and B.G. Schunck. Determining optical flow. *Artificial Intelligence*, 17:185–204, 1981.
- [87] W. Hort. Mikrometrische untersuchungen an verschieden weiten meerschweinchenherzen. *Verhandl Deut Ges Krieslaufforsch*, 23:343–346, 1957.
- [88] W. Hort. Untersuchungen uber die muskelfaserdehnung und das gefullter des myokards in der rechten herzkammerwand des meerschweinchens. *Virchows Archiv*, 329, 1957.
- [89] W. Hort. Makroskopische und mikrometrische untersuchungen am myokard verschieden stark gefullter linker kammern. *Virchows Archiv*, 333, 1960.
- [90] W. Hort. Quantitative morphology and structural dynamics of the myocardium. *Methods Achiev Exp Pathol*, 5:3–21, 1971.

- [91] W.C. Huang and D.B. Goldgof. Adaptive-size meshes for rigid and nonrigid shape analysis and synthesis. *Pattern Analysis and Machine Intelligence, IEEE Transactions on*, 15(6):611–616, 1993.
- [92] A. Hyvarinen, J. Karhunen, and E. Oja. *Independent Component Analysis*. Wiley, 2001.
- [93] L.D. Jacobs, I.S. Salgo, and S. Goonewardena. Rapid online quantification of left ventricular volume from real-time three-dimensional echocardiographic data. *European Heart Journal*, 27:460468, 2006.
- [94] I.T. Jolliffe. *Principal Component Analysis*. Springer, 2002.
- [95] P.S. Jouk, Y. Usson, G. Michalowicz, and L. Grossi. Three-dimensional cartography of the pattern of the myofibres in the second trimester fetal human heart. *Anatomy and Embryology*, 202:103–118, 2000.
- [96] C. Kambhamettu and D.B. Goldgof. Curvature-based approach to point correspondence recovery in conformal nonrigid motion. *Comput. Vis. Graph. Imag. Processing*, 60(1):26–43, 1994.
- [97] M. Kass, A. Witkin, and D. Terzopoulos. Snakes: Active contour models. *Int. J. Comput. Vis.*, 1(4):321–331, 1988.
- [98] M. Kocica, A. Corno, F. Carreras-Costa, M. Ballester-Rodes, M. Moghbel, C. Cueva, V. Lackovic, V. Kanjuh, and F. Torrent-Guasp. The helical ventricular band: global, three-dimensional, functional architecture of the ventricular myocardium. *European Journal of Cardio-thoracic Surgery*, 29:21–40, 2006.
- [99] L. Krehl. Beitrage zur kenntnis der fullung und entleerung des herzens. *Abh Math-Phys Kl Saechs Akad Wiss*, 17:341–362, 1891.
- [100] S. Kumar and D. Goldgof. Automatic tracking of spamm grid and the estimation of deformation parameters from cardiac mr images. *IEEE Trans. Med. Imag.*, 13:122–132, 1994.
- [101] M. Kuwahara and S. Eiho. 3-d heart image reconstructed from mri data. *Comput. Med. Imag. Graph.*, 15(4):241–246, 1991.
- [102] J.R. Landis and G.G. Koch. The measurement of observer agreement for categorical data. *Biometrics*, 33:159–174, 1977.
- [103] Jose Leal, Ramon Luengo-Fernandez, Alastair Gray, Sophie Petersen, and Mike Rayner. Economic burden of cardiovascular diseases in the enlarged European Union. *Eur Heart J*, 27(13):1610–1619, 2006.
- [104] M.J. Ledesma-Carbayo, A. Bajo, C. Santa Marta, E. Perez-David, M.A. Garcia-Fernandez, M. Desco, and A. Santos. Fully automatic cardiac motion estimation from tagged mri using non-rigid registration techniques. In *IEEE Proceeding Computers in Cardiology*, volume 33, pages 305–308, 2006.

- [105] M.J. Ledesma-Carbayo, J.A. Derbyshire, S. Sampath, A. Santos, M. Desco, and E.R. McVeigh. Unsupervised estimation of myocardial displacement from tagged mr sequences using nonrigid registration. *Magnetic Resonance in Medicine*, 59(1):181–189, 2008.
- [106] W. Lee, Z. Qian, C. Tosti, T. Brown, D. Metaxas, and E. Konofagou. Preliminary validation of angle-independent myocardial elastography using mr tagging in a clinical setting. *Ultrasound in Medicine & Biology*, 34(12):1980–1997, 2008.
- [107] I.J. LeGrice, P.J. Hunter, and B.H. Smaill. Laminar structure of the heart: a mathematical model. 1997.
- [108] I.J. LeGrice, B.H. Smaill, L.Z. Chai, S.G. Edgar, J.B. Gavin, and P.J. Hunter. Laminar structure of the heart: ventricular myocyte arrangement and connective tissue architecture in the dog. *Am J Physiol*, 269:571–82, 1995.
- [109] I.J. LeGrice, Y. Takayama, and J.W. Covell. Transverse shear along myocardial cleavage planes provides a mechanism for normal systolic wall thickening. *Circ.*, 77:182193, 1995.
- [110] C. Lenglet, M. Rousson, R. Deriche, and O. Faugeras. Statistics on the manifold of multivariate normal distributions: Theory and application to diffusion tensor mri processing. *Journal of Mathematical Imaging and Vision*, 25(3):423–444, 2006.
- [111] K.Y.E. Leung and J.G. Bosch. Localized shape variations for classifying wall motion in echocardiograms. In *Medical Image Computing and Computer-Assisted Intervention - MICCAI 2004*, volume 4791 of *Lecture Notes in Computer Science*, pages 52–59, 2007.
- [112] K.Y.E. Leung, M. van Stralen, M.M. Voormolen, N. de Jong, A.F.W. van der Steen, J. H. Reiber, and J.G. Bosch. Improving 3DActive AppearanceModel Segmentation of the Left Ventricle with Jacobian Tuning. In *SPIE Medical Imaging*, volume 6914, page 69143B, 2008.
- [113] M. Lev and C.S. Simkins. Architecture of the human ventricular myocardium. technique for study using a modification of the mall-macallum method. *Lab Invest*, 5:396–409, 1956.
- [114] C.H. Lorenz, J.S. Pastorek, and J.M. Bundy. Delineation of normal human left ventricular twist throughout systole by tagged cine magnetic resonance imaging. *J Cardiovasc Magn Reson*, 2(2):97–108, 2000.
- [115] C.H. Lorenz, E.S. Walker, V.L. Morgan, S.S. Klein, and T.P. Graham. Normal human right and left ventricular mass, systolic function, and gender differences by cine magnetic resonance imaging. *J Cardiovasc Magn Reson*, 1(1):7–21, 1999.
- [116] R. Lower. *Tractatus de corde*, 1669.

- [117] G. Luo and P.A. Heng. Lv shape and motion: B-spline-based deformable model and sequential motion decomposition. *9(3):430–446*, 2005.
- [118] F. Maes, A. Collignon, D. Vandermeulen, G. Marchal, and P. Suetens. Multimodality image registration by maximization of mutual information. *Medical Imaging, IEEE Transactions on*, 16(2):187–198, 1997.
- [119] T. Makela, P. Clarysse, O. Sipila, N. Pauna, C.P. Quoc, T. Katila, and I.E. Magnin. A review of cardiac image registration methods. *Medical Imaging, IEEE Transactions on*, 21(9):1011–1021, 2002.
- [120] F.P. Mall. On the muscular architecture of the ventricles of the human heart. *Am J Anat*, 11:211–266, 1911.
- [121] S. Mansor, N.P. Hughes, and J.A. Noble. Wall motion classification of stress echocardiography based on combined rest-and-stress data. In *Medical Image Computing and Computer-Assisted Intervention - MICCAI 2004*, volume 5242 of *Lecture Notes in Computer Science*, pages 139–146, 2008.
- [122] B.J. Maron, T.J. Anan, and W.C. Roberts. Quantitative analysis of the distribution of cardiac muscle cell disorganization in the left ventricular wall of patients with hypertrophic cardiomyopathy. *Circulation*, 63:882–894, 1981.
- [123] A. Matheny and D.M. Goldgof. The use of three- and four-dimensional surface harmonics for rigid and nonrigid shape recovery and representation. *IEEE Trans. Pattern Anal. Machine Intell.*, 17:967–981, 1995.
- [124] T. Maxime, N. Paragios, and M.P. Jolly. From uncertainties to statistical model building and segmentation of the left ventricle. In *Computer Vision, 2007. ICCV 2007. IEEE 11th International Conference on*, pages 12–26, 2007.
- [125] T. McInerney and D.i Terzopoulos. Deformable models in medical image analysis: a survey. *Tim McInerney, a, and Demetri Terzopoulos*, 1(2):91–108, 1996.
- [126] M. McLean and J. Prothero. Myofiber orientation in the weanling mouse heart. *Am J Anat*, 192:425–441, 1991.
- [127] D. Metaxas and D. Terzopoulos. Shape and nonrigid motion estimation through physics-based synthesis. *IEEE Trans. Pattern Anal. Machine Intell.*, 15:580–591, 1993.
- [128] D.N. Metaxas. *Physics-based Deformable Models: Applications to Computer Vision, Graphics, and Medical Imaging*. Springer, 1997.
- [129] F.G. Meyer, R.T. Constable, A.J. Sinusas, and J.S. Duncan. Tracking myocardial deformation using phase contrast mr velocity fields: A stochastic approach. *IEEE Trans. Med. Imag.*, 15:453–465, 1996.
- [130] J. Milles, A. van Susteren, T. Arts, P. Clarysse, P. Croisille, and I.E. Magnin. Automatic 2d segmentation of the left ventricle in tagged cardiac mri using motion information. In *Biomedical Imaging: Nano to Macro, 2004. IEEE International Symposium on*, pages 153–156, 2004.

- [131] S.K. Mishra, D.B. Goldgof, T.S. Huang, and C. Kambhamettu. Curvature-based nonrigid motion analysis from 3d point correspondences. *Int. J. Image Syst. Tech.*, 4:214–225, 1992.
- [132] M. Moakher. A differential geometry approach to the geometric mean of symmetric positive-defined matrices. *SIAM-J. Mat. Ana. App.*, 26(3):735–747, 2005.
- [133] C.C. Moore, C.H. Lugo-Olivieri, E.R. McVeigh, and E.A. Zerhouni. Three-dimensional systolic strain patterns in the normal human left ventricle - characterization with tagged mr imaging. *Radiology*, 214:453–466, 2000.
- [134] V. Mor-Avi, L. Sugeng, L. Weinert, and et al. Fast measurement of left ventricular mass with real-time three-dimensional echocardiography: comparison with magnetic resonance imaging. *Circulation*, 110:1814–1818, 2004.
- [135] S. Morita, T. Nagase, and K. Nomizu. *Geometry of Differential Forms*, volume 201 of *Iwanami Series in Modern Mathematics*. American Mathematical Society Bookstore, 2001.
- [136] A. Mourad, L. Biard, D. Caillerie, P.S. Jouk, A. Raoult, and Y. Usson. Geometrical modelling of the fibre organization in the human left ventricle. In *Functional imaging and modelling of the heart FIMH 2001*, volume 2230 of *LNCS*, pages 32–38, 2001.
- [137] Computational Cardiac Anatomy Using MRI. M.f. beg and p.a. helm and e. mcveigh and m.i. miller and r.l. winslow. *Magn Reson Med*, 52(5):1167–1174, 2004.
- [138] J. Nash. The imbedding problem for riemannian manifolds. *Annals of Math*, 63(2):20–63, 1956.
- [139] N.M.I. Noble, D.L.G. Hill, M. Breeuwer, and R. Razavi. The automatic identification of hibernating myocardium. In *Medical Image Computing and Computer-Assisted Intervention - MICCAI 2004*, volume 3217 of *Lecture Notes in Computer Science*, pages 890–898, 2004.
- [140] M.K. O'Connor. Evaluation of Motion-Correction Techniques in Cardiac SPECT. *J Nucl Med*, 41(7), 2000.
- [141] W.G. O'Dell, C.C Moore, W.C. Hunter, E.A. Zerhouni, and E.R. McVeigh. Three-dimensional myocardial deformations: calculation with displacement field fitting to tagged mr images. *Radiology*, 195(3):829–835, 1995.
- [142] S. Ordas and A.F. Frangi. Automatic quantitative analysis of myocardial wall motion and thickening from long- and short-axis cine mri studies. In *Proceedings of the 2005 IEEE Engineering in Medicine and Biology 27th Annual Conference*, pages 7028–7031, 2005.
- [143] F. Orderud, G. Kiss, S. Langeland, E.W. Remme, and et al. Real-time left ventricular speckletracking in 3d echocardiography with deformable subdivision surfaces. In *MICCAI 2008 Workshop on Analysis of Functional Medical Images*, page 4148, 2008.

- [144] F. Orderud and S.I. Rabben. Real-time 3d segmentation of the left ventricle using deformable subdivision surfaces. In *CVPR'08 IEEE Conference on*.
- [145] N.F. Osman, W.S. Kerwin, E.R. McVeigh, and J.L. Prince. Cardiac motion tracking using cine harmonic phase (harp) magnetic resonance imaging. *Magnetic Resonance in Medicine*, 42:1048–1060, 1999.
- [146] N.F. Osman, E.R. McVeigh, and J.L. Prince. Imaging heart motion using harmonic phase mri. *IEEE Trans. Med. Im.*, 19:186–202, 2000.
- [147] G. Aubert M. Barlaud P. Charbonnier, L. Blanc-Feraud. Deterministic edge-preserving regularization in computed imaging. *IEEE Transactions on Image Processing*, 6(2):298–311, 1997.
- [148] N. Paragios, M.P. Jolly, M. Taron, and R. Ramaraj. *Scale Space and PDE Methods in Computer Vision*, volume 3459 of *Lecture Notes in Computer Science*, chapter Active Shape Models and Segmentation of the Left Ventricle in Echocardiography, pages 131–142. Springer Berlin / Heidelberg, 2005.
- [149] J. Park, D.N. Metaxas, A.A. Young, and L. Axel. Deformable models with parameter functions for cardiac motion analysis from tagged mri data. *IEEE Trans. Med. Imag.*, 15:278–289, 1996.
- [150] A.S. Pednekar, R. Muthupillai, B. Cheong, and S.D. Flamm. Automatic computation of left ventricular ejection fraction from spatiotemporal information in cine-ssfp cardiac mr images. *Journal of Magnetic Resonance Imaging*, 28(1):39–50, 2008.
- [151] X. Pennec. Intrinsic statistics on riemannian manifolds - basic tools for geometric measurements. *Journal of Mathematical Imaging and Vision*, 25:127–154, 2006.
- [152] C. Petitjean, N. Rougon, and F. Preteux. Building and using a statistical 3d motion atlas for analyzing myocardial contraction in mri. In *In Proceedings SPIE Conference on Image Processing - SPIE International Symposium Medical Imaging, San Diego, CA*, volume 5370, pages 14–19, 2004.
- [153] J-M. Peyrat, M. Sermesant, X. Pennec, and "et al.". A computational framework for the statistical analysis of cardiac diffusion tensors: application to a small database of canine hearts. *IEEE Trans. Med. Imag.*, 26(10):1500–1514, 2007.
- [154] J.L. Prince and E.R. McVeigh. Motion estimation from tagged mr image sequences. *IEEE Transactions on Medical Imaging*, 11:238–249, 1992.
- [155] M.A. Quinones, W.H. Gaasch, and J.K. Alexander. Influence of acute changes in preload, afterload contractile state and heart rate on ejection and isovolumetric indices of myocardial contractility in man. *Circ.*, 53:293–302, 1976.
- [156] S. Rahimtoola. Coronary bypass surgery for chronic angina. *Circulation*, 65:225–241, 1982.

- [157] A. Rao, R. Chandrashekar, G.I. Sanchez-Ortiz, M. Lorenzo-Valdes, R. Mohiaddin, and D. Rueckert. Construction of a cardiac motion atlas from mr using nonrigid registration. In *In Functional Imaging and Modeling of the Heart, FIMH03*, volume 2674, 2003.
- [158] A. Rao, R. Chandrashekar, G.I. Sanchez-Ortiz, R. Mohiaddin, P. Aljabar, J.V. Hanjnal, B.K. Puri, and D. Rueckert. Spatial transformation of motion and deformation fields using non-rigid registration. *IEEE Transactions on Medical Imaging*, 23(9):1065–1076, 2004.
- [159] A. Rao, G.I. Sanchez-Ortiz, R. Chandrashekar, M. Lorenzo-Valdes, R. Mohiaddin, and D. Rueckert. Comparison of cardiac motion across subjects using nonrigid registration. In *Fifth Int. Conf. on Medical Image Computing and Computer-Assisted Intervention (MICCAI)*, volume 2488 of *Lecture Notes in Computer Science*, pages 722–729, 2002.
- [160] E.W. Remme, A.A. Young, K.F. Augenstein, B. Cowan, and P.J. Hunter. Extraction and quantification of left ventricular deformation modes. *Biomedical Engineering, IEEE Transactions on*, 51(11):1923–1931, 2004.
- [161] J.S. Robb and R.C. Robb. The normal heart anatomy and physiology of the structural units. *Am Heart J*, 23:455467, 1942.
- [162] D.E. Roberts, L.T. Hersh, and A.M. Scher. Influence of cardiac fiber orientation on wavefront voltage, conduction velocity, and tissue resistivity in the dog. *Circ. Res.*, 44:701–712, 1979.
- [163] W.C. Roberts, R.J. Siegel, and B.M. McManus. Ideopathic dilated cardiomyopathy: Analysis of 152 necropsy patients. *Am. J. Cardiol.*, 60:1340–1355, 1987.
- [164] N. Rougon, F. Prêteux C. Petitjean, and et al. A non-rigid registration approach for quantifying myocardial contraction in tagged mri using generalized information measures. *Med. Imag. Ana.*, 9:353–375, 2005.
- [165] N. Rougon, C. Petitjean, F. Preteux, P. Cluzel, and P. Grenier. A non-rigid registration approach for quantifying myocardial contraction in tagged mri using generalized information measures. *Med. Imag. An.*, 9(4):353–375, 2005.
- [166] D. Rueckert and P. Burger. Geometrically deformable templates for shape-based segmentation and tracking in cardiac mr images. In *Energy Minimization Methods in Computer Vision and Pattern Recognition*, volume 1223 of *Lecture Notes in Computer Science*, pages 83–98, 1997.
- [167] D. Rueckert, L.I. Sonoda, C. Hayes, D.L.G. Hilland M.O. Leach, and D.J. Hawkes. Nonrigid registration using free-form deformations: application to breast mr images. *Medical Imaging, IEEE Transactions on*, 18(8):712–721, 1999.
- [168] R.F. Rushmer, D.K. Crystal, and C. Wagner. The functional anatomy of ventricular contraction. *Circ Res*, 1:162–170, 1953.

- [169] M.M. Samyn. A review of the complementary information available with cardiac magnetic, resonance imaging and multislice computed tomography during the study of congenital heart disease. *Int J Card Imaging*, 20:569–578, 2004.
- [170] D. Sanchez-Quintana, V. Garcia-Martinez, and J.M. Hurle. Myocardial fibre architecture in the human heart. *Anat Rec*, 217:263–273, 1990.
- [171] Y. Sato, M. Moriyama, M. Hanayama, H. Naito, and S. Tamura. Acquiring 3d models of nonrigid moving objects from time and viewpoint varying image sequences: A step toward left ventricle recovery. *IEEE Trans. Pattern Anal. Machine Intell.*, 19:253–259, 1997.
- [172] A. Savi, M.C. Gilardi, G. Rizzo, M. Pepi, C. Landoni, C. Rossetti, G. Lucignani, A. Bartorelli, and F. Fazio. Spatial registration of echocardiographic and positron emission tomographic heart studies. *European Journal of Nuclear Medicine and Molecular Imaging*, pages 243–247, 2005.
- [173] P. Schmid, T. Jaermann, P. Boesiger, P.F. Niederer, P.P. Lunkenheimer, C.W. Cryer, and R.H. Anderson. Ventricular myocardial architecture as visualised in postmortem swine hearts using magnetic resonance diffusion tensor imaging. *Eur J Cardiothorac Surg*, 27:468–472, 2005.
- [174] D.F. Scollan, A. Holmes, R.L. Wilson, and "et al.". Histological validation of myocardial microstructure obtained from diffusion tensor imaging. *Am. J. Phys.- Heart and Circ. Phys.*, 275:2308–2318, 1998.
- [175] M. Sermesant, H. Delingette, and N. Ayache. An electromechanical model of the heart for image analysis and simulation. *Medical Imaging, IEEE Transactions on*, 25(5):612–625, 2006.
- [176] M. Sermesant, K. Rhode, G.I. Sanchez-Ortiz, O. Camara, R. Andriantsimiavona, S. Hegde, D. Rueckert, P. Lambiase, C. Bucknall, E. Rosenthal, H. Delingette, D.L.G. Hill, N. Ayache, and R. Razavi. Simulation of cardiac pathologies using an electromechanical biventricular model and xmr interventional imaging. *Medical Image Analysis*, 9(5):467–480, 2005.
- [177] S.M. Song and R.M. Leahy. computation of 3d velocity fields from 3d cine ct images of a human heart. *IEEE Trans. Med. Imag.*, 10:295–306, 1991.
- [178] S.M. Song, R.M. Leahy, D.P. Boyd, B.H. Brundage, and S. Napel. determining cardiac velocity fields and intraventricular pressure distribution from a sequence of ultrafast ct cardiac images. *IEEE Trans. Med. Imag.*, 14:386–397, 1994.
- [179] S.M. Song, S. Napel, N.J. Pelc, and G.H. Glover. Phase unwarping of mr phase images using poisson equation. *IEEE Trans. Imag. Process.*, 4:667–676, 1995.
- [180] L.H. Staib and J.S. Duncan. Model-based deformable surface finding for medical images. *IEEE Trans. Med. Imag.*, 15:720–731, 1996.
- [181] G.D. Stetten. Active fourier contour applied to real time 3d ultrasound of the heart. *International Journal of Image and Graphics*, 1(4):647–658, 2001.

- [182] D.D. Streeter. Gross morphology and fibre geometry of the heart. *The cardiovascular system.*, pages 61–112, 1979.
- [183] D.D. Streeter and C. Ramon. Muscle pathway geometry in the heart wall. *J Biomech Eng.*, 105(4):367–373, 1983.
- [184] P. Suetens. *Fundamentals of Medical Imaging*. Cambridge University Press, 2002.
- [185] A. Suinesiaputra, A.F. Frangi, T.A. Kaandorp, H.J. Lamb, J.J. Bax, J.H. Reiber, and B.P. Lelieveldt. Automated detection of regional wall motion abnormalities based on a statistical model applied to multislice short-axis cardiac mr images. *IEEE Trans Med Imaging*, 28(4):595–607, 2009.
- [186] H. Sundar, D. Shen, G. Biros, and et al. Estimating myocardial fiber orientation by template warping. In *3rd IEEE Int. Symp. Biomed. Imag. (ISBI'06)*, pages 73–76, 2006.
- [187] B. Taccardi, R.L. Lux E. Macchi, and P.R. Ershler. Effect of myocardial fiber direction on epicardial potentials. *Circulation*, 90:3076–3090, 1994.
- [188] R. Tennant and C.J. Wiggers. The effect of coronary occlusion on myocardial contraction. *Am J Physiol*, 112:351–361, 1935.
- [189] M. Termeer, J.O. Bescos, M. Breeuwer, A. Vilanova, F. Gerritsen, and M.E. Groller. Covicad: Comprehensive visualization of coronary artery disease. *Visualization and Computer Graphics, IEEE Transactions on*, 6:1632–1639, 2007.
- [190] F. Tezuka. Muscle fiber orientation in normal and hypertrophied hearts. *Tohoku J. Exp. Med.*, 117:289–297, 1975.
- [191] C. Tobon-Gomez, A.F. Frangi S. Ordas, S. Aguade, and J. Castell. *Deformable Models Biomedical and Clinical Applications*, chapter Statistical deformable models for cardiac Segmentation and Functional Analysis In Gated-Spect Studies, pages 163–193. International Topics in Biomedical Engineering. Springer New York, 2007.
- [192] F. Torrent-Guasp. El ciclo cardiaco - consideraciones criticas sobre la interpretación clásica y nuevas ideas sobre el mismo. *Diana Artes Graficas*, pages 13–45, 1954.
- [193] F. Torrent-Guasp. La estructuració n macroscópica del miocardio ventricular. *Rev Esp Cardiol*, 133:265–287, 1980.
- [194] F. Torrent-Guasp. Estructura y función del corazón. *Rev Esp Cardiol*, 51:91–102, 1998.
- [195] F. Torrent-Guasp, M. Ballester, G.D. Buckberg, F. Carreras, A. Flotats, I. Carrio, A. Ferreira, L.E. Samuels, and J. Narula. Spatial orientation of the ventricular muscle band: Physiologic contribution and surgical implications. *J Thorac Cardiovasc Surg*, 122:389–392, 2001.

- [196] F. Torrent-Guasp, M. Ballester, G.D. Buckberg, and et al. Spatial orientation of the ventricular muscle band - physiologic contribution and surgical implications. *J Thorac Cardiovasc Surg*, 122:389–392, 2001.
- [197] F. Torrent-Guasp, G.D. Buckberg, C. Clemente, and et al. The structure and function of the helical heart and its buttress wrapping. the normal macroscopic structure of the heart. *Semin Thorac Cardiovasc Surg*, 13(4):301–319, 2001.
- [198] F. Torrent-Guasp, J.M. Caralps-Riera, and M. Ballester. Cuatro propuestas para la remodelación ventricular en el tratamiento quirúrgico de la miocardiopatía dilatada. *Rev Esp Cardiol*, 1997.
- [199] W.Y. Tseng, V.J. Wedeen, T.G. Reese, R.N. Smith, and E.F. Halpern. Diffusion tensor mri of myocardial fibers and sheets: correspondence with visible cut-face texture. *J Magn Reson Imaging*, 17:31–42, 2003.
- [200] Y. Usson, F. Parazza P.S. Jouk, and G. Michalowicz. Method for the study of the threedimensional orientation of myocardial cells by means of confocal scanning laser microscopy. *J Microsc*, 174:101–110, 1994.
- [201] H.C. van Assen, M.G. Danilouchkine, M.S. Dirksen, J.H.C. Reiber, and B.P.F. Lelieveldt. A 3-d active shape model driven by fuzzy inference: Application to cardiac ct and mr. *Information Technology in Biomedicine, IEEE Transactions on*, 12(5):595–605, 2008.
- [202] R.J van der Geest, V.G.M. Buller, E. Jansen, and et al. Comparison between manual and semiautomated analyssi of left ventricular volume parameters from short-axis mr images. *J. Comp. Assist. Tomo.*, 21 (5):756–765, 1997.
- [203] M.A. Vannan, P. Li, J. Wang, and et al. Isolated diastolic dysfunction is a velocity vector imaging. *J Am Coll Cardiol*, in press.
- [204] F.L. Villarreal, L.K. Waldman, and W.Y.W. Lew. Technique for measuring regional two-dimensional finite strains in canine left ventricle. *Circ. Res.*, 62(4):711–721, 1988.
- [205] C. Vuille and A.E. Weyman. *Left ventricle I: general considerations, assessment of chamber size and function*. Philadelphia, PA: Lea and Fabiger, 1994.
- [206] E. Waks, R.L. Prince, and A. Douglas. Cardiac motion simulator for tagged mri. In *Math. Meth . Biomed. Imag . Anal.*, pages 182–191, 1996.
- [207] S. Webb. *The Physics of Medical Imaging*. Bristol; Philadelphia - Hilger, 1988.
- [208] S.A. Wickline, E.D. Verdonk, A.K. Wong, and et al. Structural remodeling of human myocardial tissue after infarction. quantification with ultrasonic backscatter. *Circulation*, 85:259–268, 1992.
- [209] C. Xu and J.L. Prince. Snakes, shapes and gradient vector flow. *IEEE Trans. Imag. Proc.*, 7(3):359–369, 1998.

- [210] A.L. Yettram, C.A. Vinson, and D.G. Gibson. Computer modeling of the human left ventricle. *J. Biomech.*, 104(2):148–152, 1982.
- [211] A.A. Young and L. Axel. Three-dimensional motion and deformation of the heart wall: Estimation with spatial modulation of magnetization- a model based approach. *Radiology*, 185(1):241–247, 1992.
- [212] A.A. Young, B.A. French, Z. Yang, B.R. Cowan, W.D. Gilson, S.S. Berr, C.M. Kramer, and F.H. Epstein. Reperfused myocardial infarction in mice: 3d mapping of late gadolinium enhancement and strain. *J Cardiovasc Magn Reson.*, 8(5):685–692, 2006.
- [213] A.A. Young, P.J. Hunter, and B.H. Smaill. Epicardial surface estimation from coronary angiograms. *Comput. Vis. Graph. Imag. Processing*, 47(1):111–127, 1989.
- [214] A.A. Young, P.J. Hunter, and B.H. Smaill. Estimation of epicardial strain using the motions of coronary bifurcations in biplane cineangiography. *IEEE Trans. Biomed. Eng.*, 39:526–531, 1992.
- [215] A.A. Young, I.J. LeGrice, M.A. Young, and B.M. Smaill. Extended confocal microscopy of myocardial laminae and collagen network. *J Microscopy*, 192:139–150, 1998.
- [216] B. Zitova and J. Flusser. Image registration methods: A survey. *Im. Vis. Comp.*, 21:977–1000, 2003.